

# WAVEFRONT SENSING FOR ADAPTIVE OPTICS

A thesis submitted for the  
Degree of Doctor of Philosophy  
in the  
Faculty of Physics

Bangalore University

By

J.P.Lancelot Chellaraj Thangadurai



Photonics Division  
Indian Institute of Astrophysics  
Bangalore – 560 034  
INDIA

Bangalore University  
July 2007

## **DECLARATION**

I hereby declare that the matter contained in this thesis is the result of the investigations carried out by me at the Photonics Division of Indian Institute of Astrophysics, Bangalore – 560 034, under the guidance and supervision of Dr.Ajay Kumar Saxena, Dean, Faculty of Sciences, Indian Institute of Astrophysics, Bangalore.

This work has not been submitted for the award of any degree, diploma, associateship, fellowship, etc., of any university or other institute.

J.P.Lancelot Chellaraj Thanagadurai  
Principal Scientific Officer  
Photonics Division  
Indian Institute of Astrophysics  
Bangalore – 560 034.

Guide:

Dr.A.K.Saxena  
Dean (Engg.)  
Faculty of Sciences  
Indian Institute of Astrophysics  
Bangalore – 560 034.

## **CERTIFICATE**

This is to certify that the matter contained in this thesis is the result of the investigations carried out by Mr.J.P.Lancelot Chellaraj Thangadurai, at the Photonics Division of Indian Institute of Astrophysics, Bangalore – 560 034, under my guidance and supervision.

This work has not been submitted for the award of any degree, diploma, associateship, fellowship, etc., of any university or other institute.

Research Guide

Dr.A.K.Saxena  
Dean (Engg.)  
Faculty of Sciences  
Indian Institute of Astrophysics  
Bangalore – 560 034.

## **ABSTRACT**

A wavefront sensor in an adaptive optics system, measures the phase changes across the telescope pupil of the incident beam. The estimate of these errors is later used in a closed loop correction system to achieve close to diffraction limited optical quality. A new wavefront sensor based on polarization shearing interferometry technique using two crossed Babinet Compensators (BC) has been developed and studied. The necessary theory for shearing interferometry using BC has been developed. Simulations of the interferometric records were carried out for the study of various aberrations in an optical system and the effect of noise, ripple and atmospheric turbulence in the interferograms. The geometry of the optical set up for carrying out the laboratory experiments using Shack Hartmann and Polarization Shearing Interferometer wavefront sensors in the same set up have been described. The data reduction procedure for the estimation of wavefront errors from a single interferometric record using Fourier technique has been worked out. The actual results obtained from the laboratory experiments for both the sensors have been compared. The method provides a convenient alternative choice for wavefront sensing in an actual adaptive optics system for astronomical telescope. The suitability of this new wavefront sensor is highlighted.

*to my mother  
in loving memory*

## **ACKNOWLEDGEMENTS**

This thesis work was carried out as a research and development project at the Photonics Division of Indian Institute of Astrophysics. I would like to place on record my sincere thanks to Prof.Siraj Hasan, Director, Indian Institute of Astrophysics, the Board of Graduate Studies and other authorities for giving me permission to carry out this research work in the institute in addition to my regular responsibilities and constant encouragement.

First, I would like to thank Dr. Ajay Kumar Saxena for introducing me to this field of Optics, furnishing me with the problem, encouraging me throughout the period of this work and guiding me in every step. He has been my supervisor and scientific mentor and a great source of my strength. He made this work possible and I would like to thank him for giving me the confidence and the motivation to continue this research work.

I would like to thank the Chairman, Physics Department, Bangalore University for their support in carrying out this work. Also I would like to thank the Vice-Chancellor and the administrative staff of Ph.D. section of the Bangalore University, particularly Ms.Saraswathi for providing all the necessary administrative support during this period.

I would like to acknowledge and thank Prof.S.K.Saha, Mr.V.Chinnappan my colleagues, for many fruitful discussions and suggestions during the course of this work. I would also like to thank my colleague Dr.S.Chatterjee for patiently reading through this thesis and for his critical comments, which greatly improved its form. I owe my deep gratitude to Dr. Christina Birdie who meticulously read through the manuscript and offering her valuable suggestions.

My sincere thanks to all my colleagues at the Photonics Division, Mr.V.Gopinath, Mr.M.G.Mohan, Mr.Ismail Jabilullah, Mr.V.Robert for their assistance in the laboratory experiment and to Mr.Mohammad Ismail for his help in LabView programming. Thanks also to Mr.K.Subramanian for his CAD drawings that appear in this thesis and to Mr.Kanagaraj and Thyagarajan for binding this thesis. My thanks are due to Mr.Mallesiah and Ms.Padma for their administrative support from the Photonics Division.

I would like to thank my wife Chitra, my son Andrew and my daughter Bettina and my father Paul and to all my friends for their love, continued encouragement and bearing with me for not attending to their chores.

Finally, I would like to thank my Heavenly Father who has been leading me right from the beginning till now and for his future guidance.

The sun has one kind of splendor,  
the moon another and the stars another;  
and star differs from star in splendor.

1 Cor.15:41

# Contents

Declaration	ii
Certificate	iii
Abstract	iv
Acknowledgements	v
Contents	vii
List of Abbreviations	x
List of Figures	xi
List of Tables	xv
1. Introduction.....	1
2. Imaging through Atmospheric Turbulence.....	8
2.1 The statistics of the amplitude and phase perturbations.....	9
2.2 Temporal and anisoplanatic effects.....	12
2.3 Image formation.....	14
2.3.1 Long Exposure Imaging.....	16
2.3.2 Short Exposure Imaging.....	16
2.4 Zernike representation of atmospheric turbulence.....	17
2.4.1 Phase variance and image quality .....	23
3. Adaptive Optics System and its elements.....	24
3.1 Wavefront Sensing .....	25
3.1.1 Concept and methods of Wavefront sensing .....	26
3.1.2 Shack Hartmann Wavefront sensor .....	27
3.1.3 Curvature wavefront sensor .....	30

3.1.4 Pyramid wavefront sensor .....	31
3.1.5 Shearing Interferometry based Wavefront Sensor ..	33
3.2 Wavefront correcting system .....	35
3.2.1 Tip-tilt mirror .....	36
3.2.2 Deformable mirror .....	36
3.3 Wavefront controller .....	38
4. Polarization Shearing Interferometer based wavefront Sensor .....	39
4.1. Babinet Compensator (BC) .....	40
4.2 Polarization Shearing Interferometer using single BC for the evaluation of surface/wavefront errors .....	43
4.3 Polarization Shearing Interferometer using two crossed BC .....	46
4.3.1 A geometrical approach for fringes .....	48
4.3.2 A Fourier approach for fringes .....	50
4.4 Accuracy of the phase measurement using BC based PSI ...	53
5. Theoretical Simulations .....	54
5.1 Basis of theoretical simulation .....	55
5.2 Fringe profiles in ideal conditions .....	57
5.2.1 Effect of Shear in the interferogram .....	58
5.3 Effect of Third order aberrations in fringe profiles .....	59
5.3.1 Spherical aberration and defocus .....	59
5.3.2 Primary coma and defocus .....	60
5.3.3 Primary Astigmatism and defocus .....	61
5.3.4 Tilt in X and Tilt in Y .....	61
5.3.5 All primary aberrations .....	62
5.4 Interferogram simulations using Zernike polynomial .....	62
5.5 Effect of atmospheric turbulence, noise and ripples in the PSI record .....	64
5.5.1 Effect of noise .....	66
5.5.2 Ripples .....	68
6. Reconstruction of the wavefront from PSI Interferogram .....	71

6.1 Single interferogram analysis of Polarization Shearing	
Interferogram .....	72
6.1.1 Fourier Transform analysis of the PSI interferogram	.72
6.1.2 Phase unwrapping or Determination of wavefront	
Slope .....	75
6.2 Wavefront determination from wavefront slope data using	
Zernike polynomial .....	76
6.3. Sensitivity .....	80
7. Details of the Laboratory Experimental work and the results .....	82
7.1 Laboratory experiment with Shack Hartmann Wavefront	
Sensor .....	83
7.1.1 Optical design and Layout .....	83
7.1.2 Shack Hartmann Experiment .....	85
7.1.3 Data Analysis and Results .....	88
7.2 Laboratory Experiment with Polarization Shearing	
Interferometer .....	91
7.2.1 Polarization Shearing Interferometer Experiment...	92
7.2.2 Data Analysis and Results .....	94
7.3 Discussion .....	102
8. Conclusions .....	104
Bibliography .....	107

## **List of Abbreviations**

A	- Analyzer
P	- Polarizer
AO	- Adaptive Optics
AOA	- Adaptive Optics Associates
BC	- Babinet Compensator
CCD	- Charge Couple Device
CS	- Curvature Sensor
DM	- Deformable Mirror
FFT	- Fast Fourier Transform
LSI	- Lateral Shearing Interferometer
OTF	- Optical Transfer Function
PSF	- Point Spread Function
PSI	- Polarization Shearing Interferometer
PV	- Peak-to-Valley
PZT	- Piezoelectric Transducer
SH	- Shack-Hartmann
SNR	- Signal-to-Noise Ratio
SVD	- Single Value Decomposition
WS	- Wavefront Sensor
rms	- root mean square

## List of Figures

- 2.1 A schematic of the wave propagation through turbulent atmosphere
- 2.2 The Airy pattern of a telescope image
- 2.3 The effect of image quality due to turbulence. (a) No turbulence (b) Weak turbulence (c) Moderate turbulence and (d) Strong turbulence.
- 2.4 Graphical representation of few Zernike modes
- 3.1 Schematic of an Adaptive Optics System
- 3.2 Schematic of a Shack Hartmann sensor.
- 3.3 Principle of Curvature sensor
- 3.4 Principle of Pyramid Sensor
- 3.5 A schematic representation of the lateral shearing of the wavefront.
- 4.1 A Babinet compensator prisms showing the preferential direction of the optical axis in each prism.
- 4.2 Typical view of the fringes seen in collimated monochromatic light from a Babinet Compensator when placed between two crossed polarizers. Fringes are equally spaced and depend upon the wedge angle of the prisms.
- 4.3 A schematic of the optical setup for testing a concave mirror using a single Babinet Compensator.
- 4.4 Typical interferogram using single Babinet compensator for an aspheric surface. BC is placed inside focus of the convergent beam.
- 4.5 Two crossed Babinet Compensator arrangement
- 4.6 A schematic of the optical set up for testing a concave mirror using two crossed Babinet Compensator. Note that the two compensators are placed on either side of the focus  $F_2$ . Optic axes are shown parallel for

figure clarity for actual measurement. Lens L images the mirror surface on the detector.

5.1 Front Panel of the Lab VIEW for the theoretical simulation of PSI records.

5.2 Typical Polarization Shearing Interferogram in the presence of defocus only. (a).  $D_1 = D_2$ ; (b)  $D_1 \neq D_2$ ;

5.3 Typical PSI interferogram profiles for various shear values. Equal shear values  $s = t$ ; and equal defocus values  $D_1 = D_2$ ; have been assumed in this case. The normalized shear values are (a) =0.025; (b) = 0.5; (c) = 0.075.

5.4 Typical PSI interferometric fringe profiles for spherical aberration and defocus. Different values of spherical aberrations are chosen.(a)  $A = 1 \lambda$ ; (b)  $= 10 \lambda$ ; (c)  $= \lambda/10$

5.5 Typical PSI interferogram for coma and defocus combined.

5.6 Typical PSI interferogram for Primary Astigmatism and Defocus.

5.7 Typical PSI interferogram having primary aberrations.

5.8 Simulated PSI interferograms using the Zernike coefficients (a) only defocus term and all other coefficients is zero. (b) inclusive of all Zernike coefficients.

5.9 Simulated PSI interferograms corresponding to different  $r_o$  values. (a)  $r_o = 1$ , (b)  $r_o = 0.75$ , (c)  $r_o = 0.5$ , (d)  $r_o = 0.25$ , (e)  $r_o = 0.125$ , (f)  $r_o = 0.1$ , (g)  $r_o = 0.05$ , (h)  $D/r_o = 0.025$

5.10 (a) A Noise-free fringe pattern. (b) a one dimensional profile; (c) Fourier transform of (a); (d) A noisy fringe pattern; (e) one dimensional profile; (f) Fourier transform of (d).

5.11 The effect of noise on PSI interferograms. The effect of noise introduced in the interferometric equation as an added random term in the phase. (a)  $\delta < 0.05$  (b)  $\delta < 0.15$  (c)  $\delta < 0.25$  (d)  $\delta < 0.5$

5.12 Simulated PSI interferograms for ripples. The ripples are created as cosine function introduced into the phase factor of the interferometric

equation. (a)  $\delta < 0.03; \alpha = 30.$ , (b)  $\delta < 0.03; \alpha = 90.$ , (c)  $\delta < 0.05; \alpha = 45$  (d)  $\delta < 0.5; \alpha = 120.$ ,

6.1 (a) A typical one dimensional noisy interferogram profile and (b) Fourier Transform of the interferogram

7.1 Schematic diagram of the optical layout for SH wavefront sensor

7.2 Photograph of the Actual set up

7.3 CCD image of the Shack Hartmann spots of the reference beam.

7.4 The CCD images of the Shack Hartmann spots of the aberrated beam.

7.5 A small area around each spot has been marked for computing the centroid of the spots (a) reference spots (b) Spots due to aberrated beam.

7.6 The 2D representation of the wavefront error computed from the Shack Hartmann method.

7.7 Front Panel of the Lab VIEW for the reduction of Shack Hartmann record.

7.8 Schematic diagram of the optical layout for Polarization Shearing Interferometer wavefront sensor. The positions of the BC are shown in the inset.

7.9 A close up view of the mounting of the two crosses Babinet compensators in a cell

7.10 The Interferometric record of the Polarization Shearing Interferometer obtained in the laboratory after introducing the phase error plate at the pupil plane of the optical system

7.11 Flow chart of the methodology adopted

7.12 A radial profile of the Polarization Shearing Interferogram showing the presence of high frequency noise

7.13 The same radial profile of the interferogram after removing the high frequency noise using two dimensional Fourier

- 7.14 The radial profile across the interferogram after removing the carrier frequency from the field of view.
- 7.15 A radial profile showing the  $2\pi$  ambiguity
- 7.16 The radial profile after the  $2\pi$  ambiguity removed
- 7.17 The two dimensional phase derivative inclusive of the shear factor.
- 7.18 The 2 D wavefront error map (in  $\lambda$ ) of the phase plate as computed from the Zernike polynomials.
- 7.19 A comparative plot of the 20 Zernike coefficients computed by the SH and PSI method
- 7.20 Front Panel of the Lab VIEW for the reduction of PSI record.

## List of Tables

Table 2.1 Zernike orthonormal polynomials  $Z_j$  for  $j = 1$  to 37,  $n$  is the radial order of the polynomial and  $m$  the azimuthal frequency. Index  $j$  is the polynomial ordering number and even  $j$  correspond to symmetric modes ( $\cos m\theta$ ) and odd  $j$  correspond to antisymmetric modes ( $\sin m\theta$ ).

Table 2.2 The residual variance  $\Delta_j$  of Kolomogorov turbulence after after the first  $j$  modes are removed.

Table 6.1 Zernike Polynomial X Derivative  $\gamma_{jj'}^x$  matrix elements

Table 6.2 Zernike Polynomial Y derivative  $\gamma_{jj'}^y$  matrix elements

# Chapter 1

## Introduction

Since the invention of optical telescopes by Galileo in 1609, man has started venturing into the exploration of the universe. In the last 400 years, the technology of astronomical telescopes has evolved from a simple mechanical device to more complex computer controlled instrument. Throughout this development, the basic objective remains the same, to look far and beyond with the improved sharpness of the image and angular resolution as well as sensitivity of the telescope.

Rayleigh proposed the criterion; that the two point objects are just resolved if their angular separation is such that the central maximum from one point source lies on the first minimum of the other. The theoretical resolving of optical telescopes can be determined by the expression:

$$\alpha = 1.22 \frac{\lambda}{d} \text{ radians} \quad (1.1)$$

where  $\alpha$  is the angular separation (in radians)  $\lambda$  is the wavelength of the light being collected and  $d$  is the diameter of the Primary of the telescope. Thus the angular size to which an optical telescope can detect depends on the diameter of the telescope. Besides the large photon counting

power of the telescope, the quest for high angular resolution drives one to increase the aperture of the telescope. If an optical telescope achieves its theoretical limit it is said to be *diffraction limited*. A detailed account of diffraction limited imaging for telescopes is given by Swapan (2007). But in practice, independent of the telescope size, the angular resolution is equivalent to that of a telescope with a diameter of  $\approx 10$  cm, which corresponds to about 1 arc second for visible wavelength. This is because the atmosphere through which the light from the stars propagate, is turbulent and distort the wavefront. This significantly affects the image quality at the focal plane of the telescope. With the recent advancement in computer speed and improved control electronics and optical devices, it is possible to form a fast closed loop system. The distortion induced by the turbulent atmosphere on the incoming wavefront from the stars can thus be corrected which enables the telescope to reach diffraction limited image quality thereby improving the resolution (Roggemann et al, 1997) of the ground based telescopes. Such a real time correcting system is named as Adaptive Optics (AO). The Adaptive Optics concept was originally proposed by Babcock in 1953 (Babcock, 1953) but was never put into practice till 70's due to lack of high-speed computing. The invention of lasers and high-speed computers, have enabled to realize an AO based system today. A wide range of references for the basic concepts on adaptive optics for astronomy is given in the resource letter (Milonni P, 1999).

Designing of an adaptive optics system requires a better understanding of the characteristics of the atmospheric turbulence and its effects on the wavefront aberrations. The atmospheric turbulence is a random process and can be estimated statistically by means of variances and co-variances of local refractive index fluctuations. The planar wavefront, from a distant star, propagating through the turbulent atmosphere, gets distorted due to change in refractive indices of the

different layers. As a result, the amplitude and the phase of the incoming beam fluctuate during its passage and changes with time. A study of the statistical properties of the turbulence and their characteristics and their evolution with time is discussed in the second chapter. The temporal and anisoplanatic effects are briefly discussed. The random process of the atmospheric turbulence, affect the image forming capabilities of the telescope. The expressions for the effect of short exposure and long exposure imaging are derived. A brief account of the Zernike polynomials, describing atmospheric turbulence is given.

An adaptive optics system consists of many important components. There are sensing devices, computing systems and controlling units. These components operate in a closed feedback loop. It is necessary to understand the functions of each unit and its feedback characteristics. A detailed study of the important components has been reported in the third chapter. The wavefront sensor is the most important component of an AO system. It detects the aberrations in real time and uses a closed loop servo system to correct the same. Most commonly used wavefront sensors are discussed in chapter 3. Wavefront sensing using shearing interferometry is discussed in detail. The advantages of using shearing interferometry as a wavefront sensor are illustrated. A new Polarization Shearing Interferometer based wavefront sensor has been developed as part of this dissertation.

A wavefront sensor, which measures the phase changes across the incoming wavefront, is an important component of AO system. This dissertation aims at developing a novel wavefront sensing technique based on shearing interferometry for astronomical applications. A simulation study has been performed by Jeffrey et al. (2002) on the performance of Shack Hartmann (SH) and Shearing Interferometer (SI) wavefront sensors on the propagation of laser beams through the

extended turbulence. It is shown that the performance of the shearing interferometer is superior to that of the Shack Hartmann sensor in the presence of low Fried parameter and for Rytov numbers greater than 0.2. Therefore, a new method has been developed to produce lateral shearing of the wavefront using Babinet Compensator (BC) and exploit it for wavefront sensing in adaptive optics system.

A Babinet Compensator is an effective optical device used for the measurement of phase differences. The typical shearing interferometers that are in use, shear the wavefront in either X or Y directions only. Hence, there is a requirement to record the shearing interferograms in two orthogonal directions. The unique property of the method described in the fourth chapter requires only a single interferogram to retrieve complete information of the phase. By this method, the shearing can be done in two orthogonal directions simultaneously. The fundamental laboratory optical set up for using the single BC and two crossed BC is explained in chapter 4. A geometrical approach and the Fourier approach on the use of two crossed BC interferometric fringes are also described.

Based on the theory developed in chapter four, theoretical simulations have been carried out for the case of two crossed BC. The interferometric records were simulated for primary aberrations and presented in chapter five. Rigorous simulations have been carried out for various aberrations independently and as a combination. The effect of defocus and its importance in this interferometric method is highlighted. The effects of various shear values have also been presented. The simulations have been carried out using Zernike polynomials also, since Zernike polynomials are best suited to represent atmospheric turbulence over a circular aperture and it is sufficient to retain Zernike polynomials up to sixth order. The shearing interferogram produces wavefront slope and hence the derivatives of the Zernike polynomials have been used to

demonstrate various aberrations. An attempt has been made to simulate atmospheric turbulence in terms of various values of  $r_0$ , the Fried's parameter, and its effect on the interferometric pattern has been studied. The effect of random noise and the ripples due to the fabrication defects have also been simulated and presented. Thus, the sensitivity of this interferometric method in the presence of turbulence, noise, ripples and the system errors can be well understood.

The next focus is to estimate the wavefront errors from the interferometric records generated by the new Polarization Shearing Interferometric (PSI) method. The interferograms generated by the PSI method contains the wavefront slope data. The intensity at each spatial coordinate in the aperture corresponds to the wavefront slope at that coordinate. There are two major tasks namely, to isolate the wavefront slope from the intensity values and to estimate the wavefront errors from the wavefront slope values. The methods used to perform these major tasks are explained in chapter six. The original interferogram contains the noise and the actual phase information. The Fourier method is superior to use in these situations. The Fourier method and its advantages over other methods are explained. Since no two interferograms are necessary for the PSI method, it is advantageous to use the Fourier method to retrieve the wavefront slope from the intensity data. The data thus obtained has  $2\pi$  ambiguity and a suitable method has been used to remove such ambiguities. This method is called *phase unwrapping*. After estimating the wavefront slope, the next task is to estimate the wavefront errors from these slope data. As derivatives of the Zernike polynomials can be written as a function of Zernike polynomial, this property has been exploited to derive the actual Zernike coefficients from the slope data.

After completing the study of the polarization shearing interferometer through its theoretical simulations, laboratory experiments were performed to demonstrate the efficacy of the method. The necessary optical set up for using two crossed BC has been explained. The different optical components and their specifications are presented. The experimental procedure is explained in detail in the sixth chapter. The experiments were carried out at the Photonics Division of Indian Institute of Astrophysics. Measurements were carried out using two wavefront sensors, namely, Shack Hartmann (SH) wavefront sensor and Polarization Shearing Interferometer (PSI) to compare the performances. To represent atmospheric turbulence, a thin phase plate was chosen, as a substitute to atmosphere induced errors, for this experimental purpose. The interferograms and the Shack Hartmann images were recorded using Charge Couple Device (CCD) detector in similar environmental situations. The data reduction was carried in LabView platform and the results were derived in terms of Zernike polynomial for both the wavefront sensing methods. Using the Zernike coefficients the wavefront was reconstructed. Details are given in chapter five. The discrepancies in the values of the Zernike coefficients are discussed, which are mainly due to the accuracies of the method. Due to larger spatial sampling, the PSI results are more accurate than that the Shack Hartmann method. The efficacy of the PSI method is discussed.

An attempt has been made to provide an alternative method of wavefront sensing using polarization shearing interferometer for adaptive optics application. The theory and the experimental results prove that the method offers a suitable choice for wavefront sensing. One of the main reason for ignoring shearing interferometry as a potential wavefront sensor had been that it requires two orthogonal records in order to completely estimate the wavefront errors. In this work, it has been proved that the method of polarization shearing interferometry using two

crossed Babinet compensators provide a means of reconstructing the wavefront using a single record. The advantages of this method, over others have been effectively brought out. As a part of the future plan this wavefront sensor will be used in a telescope to estimate the wavefront errors.

# Chapter 2

## Imaging Through Atmospheric Turbulence

The wavefronts from a distant star approaching the Earth are nearly perfect plane waves, coherent, in the sense that their phase is nearly uniform in a plane transverse to the direction of propagation. During its passage through the atmosphere, these wavefronts are distorted randomly by moving through different layers or cells with differences in the refractive index (Fig.2.1).

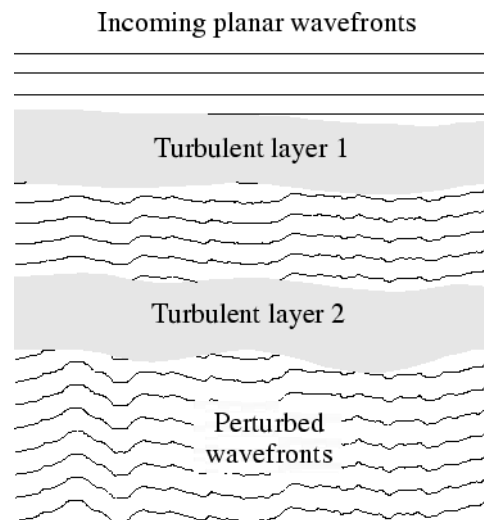


**Fig.2.1 A schematic of the wave propagation through turbulent atmosphere**

These variations in the refractive index arise from variations in density, which are caused by temperature fluctuations (Roddier, 1999). There are many models describing atmospheric turbulence, but the most commonly used one is the introduced by Kolmogorov in 1961 (Kolmogorov, 1961). The theory based on Kolmogorov turbulence has been comprehensively reviewed elsewhere (Roddier, 1999).

## 2.1 The statistics of the amplitude and Phase perturbations

In classical theory the wave propagation is treated as

$$\psi_o(\mathbf{r}, t) = A \exp [i(\phi_o + 2\pi\nu t + \vec{k} \cdot \vec{r})] \quad (2.1)$$

where  $\psi_o(\mathbf{r}, t)$  is the complex field at  $\mathbf{r}$  and time  $t$ ,  $\phi_o$  represents the a phase offset,  $\nu$  represents the frequency of the light determined by  $\nu = c|k|/2\pi$  and  $A$  the amplitude of the light. As wavefronts pass through the atmosphere they are perturbed by refractive index variations resulting in the fractional change in the amplitude and phase in a given time. The time scales for these variations will be set by the speed refractive index fluctuations in the atmosphere.

To quantify the effect of the atmosphere it is useful to decompose the atmosphere artificially into a number of distinct layers. Every layer consists of a number of turbulent cells of varying sizes and varying densities, both spatially and temporally. Thus the refractive index at any arbitrary point  $\vec{r}$  can be written as,

$$n(\vec{r}, t) = \langle n \rangle + \delta n(\vec{r}, t) \quad (2.2)$$

Where  $\delta n(\vec{r}, t)$  is the fluctuation in the refractive index,  $\vec{r}$  being a 3 dimensional vector  $\vec{r} \equiv x, y, z$ , while  $\langle n \rangle$  is the average refractive index of air. As is well known, the average  $\langle \delta n(\vec{r}, t) \rangle = 0$ , while Kolmogorov proved from pure dimensional arguments:

$$D_{nn}(\rho) = \langle |\delta n(\vec{r}, +\vec{\rho}) - \delta n(\vec{r})|^2 \rangle = C_{nn}^2 \rho^{2/3} \quad (2.3)$$

In the range  $\ell_o < \rho < L_o$  called inertial range. Since  $\ell_o \sim 1$  mm or less (called the inner scale of turbulence) while  $L_o \sim$  several tens of meters, this is also the region of importance for us as a typical telescope has a diameter  $1 \sim 5$  meters. The actual phase change depends on the transient in the air pocket and thickness of the turbulent layer and will vary with time.

In the inertial range, the statistical properties of the phase perturbations can be specified using a spatial structure function  $D_\phi$  as is given below. This structure function is valid for distances between an empirically determined inner scale and outer scale ( $l < r < L$ ). The spatial structure function is equal to the mean squared value of the difference between the phase perturbations at two points on the base of the layer, which are separated by a vector  $\rho$ . Mathematically,

$$\begin{aligned} D_\phi(\vec{\rho}) &= \langle |\phi_j(\vec{r}) - \phi_j(\vec{r} + \vec{\rho})|^2 \rangle \\ &= 2.91 \left( \frac{2\pi}{\lambda} \right)^2 (\cos \gamma)^{-1} |\rho|^{5/3} \int_0^\infty C_n^2(z) dz \\ &= 6.88 \left( \frac{|\rho|}{r_o} \right)^{5/3} \end{aligned} \quad (2.4)$$

where  $\vec{r}$  and  $\vec{\rho}$  are spatial points separated by a distance  $\rho$  and  $\langle \rangle$  denotes ensemble average over all points,  $\lambda$  is the wavelength,  $\gamma$  is the angle of observation measured from zenith,  $C_n^2$  is the refractive index structure constant which is a function of height  $z$  above ground and  $r_o$  is the fundamental Fried-parameter (Fried, 1965) defined by

$$r_o = \left[ \frac{2.91}{6.88} \left( \frac{2\pi}{\lambda} \right)^2 (\cos \gamma)^{-1} \int_0^{\infty} C_n^2(z) dz \right]^{-3/5} \quad (2.5)$$

It characterizes the effect of atmospheric turbulence at a particular wavelength. The  $r_o$  value is dependent on the integrated magnitude of refractive index variations in the atmosphere as added over all the layers. This relation points out the link between the value of  $r_o$  at the telescope and the varying value of  $C_n^2$  with height, which features strong contributions at different altitudes. The quantity  $r_o$  also depends on the zenith angle  $\gamma$  and the wavelength of observation. The length scale  $r_o$  is a measure of the phase coherence length of the light wave, as it arrives at the telescope aperture. Hence, a larger value of  $r_o$  implies better seeing. “Seeing” being described as the angular separation that the telescope can resolve, one can say

$$\theta_{seeing} = \frac{\lambda}{r_o} \sim \lambda^{-1/5} \quad (2.6)$$

Therefore, the seeing is better in the infra red compared to the visible region. It shows that an  $r_o$  value of 10 cm at 550 nm corresponds to 53 cm at 2.2 micron. Clearly, a telescope with an aperture diameter greater than  $r_o$  is limited by atmospheric turbulence to the resolving power of a telescope with an aperture diameter of only  $r_o$ . At optical wavelengths,  $r_o$  can be as large as 30 cm in very stable atmospheric conditions.

The mean square wavefront phase distortion over a circular aperture of diameter  $D$  (Rodier, 1999) can be expressed as

$$\sigma_1^2 = 1.03 \left( \frac{D}{r_o} \right)^{5/3} \quad (2.7)$$

Noll (1976) has shown that the spatial power spectrum of phase fluctuations due to Kolmogorov turbulence:

$$\Phi(k) = 0.023r_o^{-5/3}k^{-11/3} \quad (2.8)$$

The integral over the power spectrum gives the variance of the phase. The integral over  $\Phi(k) \propto k^{-11/3}$  is infinite. This means that the variance of the turbulent phase grows very fast for low  $k$ , which is a well known property of Kolmogorov turbulence. In reality, low order frequencies are truncated by the outer scale of turbulence, as modeled by the more realistic Von Karman spectrum.

## 2.2 Temporal and anisoplanatic effects

The wavefront phase distortions occur spatially and temporally. These phase fluctuations occur with a varying speed according to the wind velocity. In such case, the structure function of the wavefront phase becomes

$$D_\phi = \langle |\phi(r, t) - \phi(r, t + \tau)|^2 \rangle \quad (2.9)$$

Assuming “Taylor” approximation of a ‘frozen-in-turbulence’ a mean propagation velocity  $\bar{v}$  of air the temporal variations occur over a time scale  $\tau_o$  given by

$$\tau_o = 0.314 \frac{r_o}{\bar{v}} \quad (2.10)$$

which is of the order of few milliseconds. These time scales are also called ‘*coherence time*’. For adaptive optics the reciprocal of the coherence time indicates the required bandwidth of the closed loop correction system. Greenwood (Greenwood, 1977) after more elaborate analysis, gave a definition for the required bandwidth being, called the ‘Greenwood

frequency' that is often used to specify adaptive optics system. For a single layer, this frequency is

$$\nu = 0.43 \frac{v}{r_o} \quad (2.11)$$

As an example, if the turbulent layer moves at a speed of 10m/s, the closed loop bandwidth for  $r_o = 11$  cm, in the visual band (550 nm) is around 39 Hz.

So far, it has been assumed that a single plane wave originating from a star at an angular distance  $\gamma$  from zenith. The light of a star at a slightly different angular position travels through slightly different portions of the atmosphere and this puts the limitation in the compensated field of view. It occurs because of differences between wavefronts coming from different directions. This effect is called Anisoplanicity. As the angular separation between the observational star and the neighboring star increases the image quality decreases. For a weighted average 'h' of the layer altitudes, the anisoplanicity error is

$$\sigma_{aniso}^2(\theta) = 6.88 \left( \frac{\theta \bar{h}}{r_o \cos \gamma} \right)^{5/3} \quad (2.12)$$

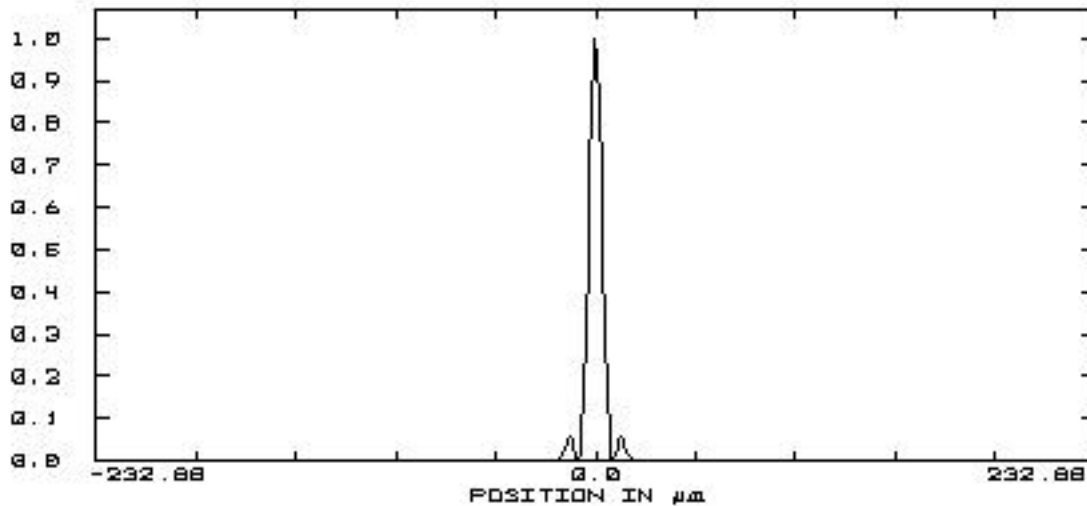
The  $\sigma_{aniso}^2$  depends on two atmospheric parameters  $\bar{h}$  and  $r_o$ . For the rms error to be less than 1 radian, the angular distance must be less than

$$\theta_o = (6.88)^{-3/5} \frac{r_o \cos \gamma}{\bar{h}} = 0.314 \frac{r_o \cos \gamma}{\bar{h}} \quad (2.13)$$

This angular distance is called iso-planatic angle.

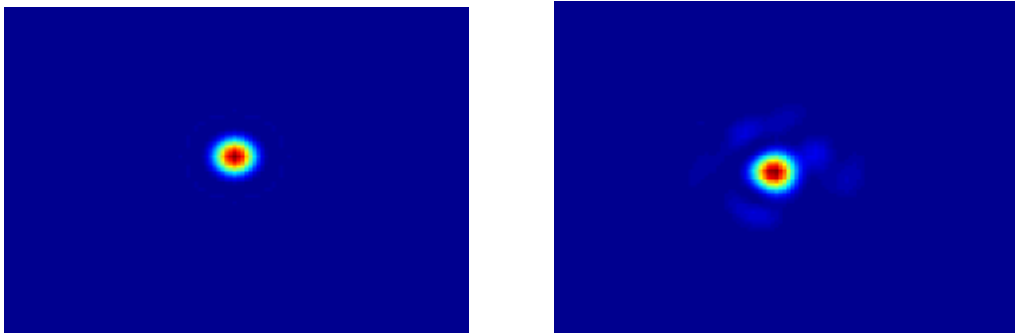
## 2.3 Image Formation

It is interesting to determine how the atmospheric turbulence affects the image quality. In the absence of turbulence, the image exhibits an Airy pattern which is called diffraction limited.



**Fig.2.2 The Airy pattern of a telescope image**

As the strength of the turbulence increases the width of the Airy pattern increases as seen in the figures. The optical transfer function of the telescope and the atmospheric turbulence determine the quality of the astronomical image. Here it is shown how the turbulence reduces the image quality obtained from a telescope.



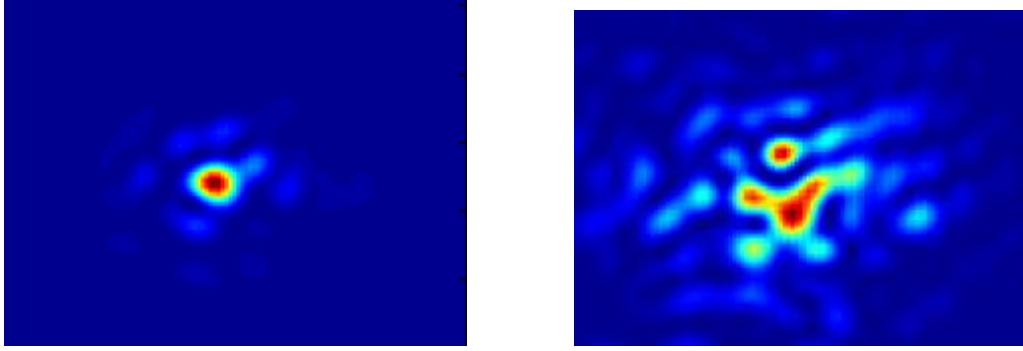


**Fig.2.3 The effect of image quality due to turbulence. (a) No turbulence (b) Week turbulence (c) Moderate turbulence and (d) Strong turbulence.**

The images presented above are reproduced from the Ph.D thesis by Seward (Seward, 2005) for the demonstration of the image quality deterioration due to Fried parameter ( $r_0$ ) in other words atmospheric turbulence. In such cases the value of  $C_{nn}$  has the following values

Strong turbulence	$19.65 \times 10^{-14}$
Moderate turbulence	$40.07 \times 10^{-15}$ to $19.60 \times 10^{-14}$
Weak turbulence	$63.65 \times 10^{-15}$ to $40.07 \times 10^{-15}$
No turbulence	$63.65 \times 10^{-16}$ and below

All units are in  $m^{-2/3}$

To achieve close to diffraction limited performance of the telescope, these effects have to be sensed and removed. The first method of correcting the effects of atmospheric turbulence to produce a nearly a diffracted image was, by the method of speckle interferometry. Labeyrie (1970) proposed a statistical method of reconstructing the image of an object from an image taken through atmospheric turbulence. This method cannot be applied for on line evaluation of the wavefront and correction. Diffraction limited images are obtained by the post processing of the speckle data obtained at very short exposures of few milli-seconds. Long exposures average out the seeing effect.

### 2.3.1 Long Exposure Imaging

A long exposure image can be considered as an image taken over a period longer than the coherence time. The point spread function for long exposure images is

$$\bar{P}_{LE} = \bar{P}_o(f)\bar{P}_a(f) \quad (2.14)$$

Here,  $\bar{P}_o(f)$  is the Optical Transfer Function (OTF) of the telescope and  $\bar{P}_a(f)$  is the atmospheric transfer function. The phase structure function of the atmosphere is given in eqn. (2.2) and so the OTF of the turbulence is

$$OTF_{urb}(r) = \exp \left[ -3.44 \left( \frac{\lambda f |r|}{r_o} \right)^{5/3} \right] \quad (2.15)$$

The atmospheric Point Spread Function (PSF) is the Fourier transform of the OTF.

### 2.3.2 Short Exposure Imaging

In the case of short exposure image, the atmosphere is considered to be frozen during the integration time of the exposure. A short-exposure image is equivalent to a tilt-free image. A time averaged short exposure image can be obtained, if the tilt is corrected in real time, for example, with a steering mirror. The expression for the short exposure OTF of Kolmogorov turbulence is [Fried, 1966].

$$OTF_{turb}(r) = \exp \left[ -3.44 \left( \frac{\lambda f |r|}{r_o} \right)^{5/3} \left( 1 - \alpha \left( \frac{\lambda f |r|}{D} \right)^{1/3} \right) \right] \quad (2.16)$$

The term  $\alpha$  is a constant and takes the value of 1 if the telescope is in the near field imaging ( $L \ll D^2 / \lambda$ ) of the turbulence. The PSF of the short exposure image is the ensemble average of the re-centered images and is again determined by taking the Fourier transform of the optical transfer function.

## 2.4 Zernike representation of atmospheric turbulence

Zernike polynomials are widely used for describing the classical aberrations of an optical system (Born & Wolf, 1965). They have the advantage that the low order polynomials are related to the classical aberrations like, spherical aberration, coma and astigmatism. Fried (Fried, 1965) used these Zernike polynomials to describe the statistical strength of aberrations produced by the atmospheric turbulence.

Zernike polynomials are a set of orthonormal polynomials, defined on a unit circle and hence are convenient to express the turbulent wavefront in the circular aperture telescope. The central obscuration can be treated as a special case and presently ignored. The modified Zernike polynomials for annular pupil has been extensively dealt in the literature (Dai and Mahajan, 2007). Noll (1976) has introduced a normalization for the Zernike polynomials that is perfectly suited for application of Kolmogorov turbulence. The Zernike polynomials are usually written in polar form  $\rho$  and  $\theta$ .

$$\begin{aligned} Z_{j_{even}} &= \sqrt{n+1} R_n^m(\rho) \sqrt{2} \cos(m\theta), \text{ for } m \neq 0 \\ Z_{j_{odd}} &= \sqrt{n+1} R_n^m(\rho) \sqrt{2} \sin(m\theta), \text{ for } m \neq 0 \\ Z_j &= \sqrt{n+1} R_n^0(\rho), \text{ for } m=0 \end{aligned} \quad (2.17)$$

$j$	$n$	$m$	$Z_j(\rho, \theta)$
1	0	0	1
2	1	1	$2\rho \cos \theta$
3	1	1	$2\rho \sin \theta$
4	2	0	$\sqrt{3} (2\rho^2 - 1)$
5	2	2	$\sqrt{6}\rho^2 \sin 2\theta$
6	2	2	$\sqrt{6}\rho^2 \cos 2\theta$
7	3	1	$\sqrt{8} (3\rho^3 - 2\rho) \sin \theta$
8	3	1	$\sqrt{8} (3\rho^3 - 2\rho) \cos \theta$
9	3	3	$\sqrt{8}\rho^3 \sin 3\theta$
10	3	3	$\sqrt{8}\rho^3 \cos 3\theta$
11	4	0	$\sqrt{5} (6\rho^4 - 6\rho^2 + 1)$
12	4	2	$\sqrt{10} (4\rho^4 - 3\rho^2) \cos 2\theta$
13	4	2	$\sqrt{10} (4\rho^4 - 3\rho^2) \sin 2\theta$
14	4	4	$\sqrt{10}\rho^4 \cos 4\theta$
15	4	4	$\sqrt{10}\rho^4 \sin 4\theta$
16	5	1	$\sqrt{12} (10\rho^5 - 12\rho^3 + 3\rho) \cos \theta$
17	5	1	$\sqrt{12} (10\rho^5 - 12\rho^3 + 3\rho) \sin \theta$
18	5	3	$\sqrt{12} (6\rho^5 - 4\rho^3) \cos 3\theta$
19	5	3	$\sqrt{12} (6\rho^5 - 4\rho^3) \sin 3\theta$
20	5	5	$\sqrt{12}\rho^5 \cos 5\theta$
21	5	5	$\sqrt{12}\rho^5 \sin 5\theta$
22	6	0	$\sqrt{7} (20\rho^6 - 30\rho^4 + 12\rho^2 - 1)$
23	6	2	$\sqrt{14} (5\rho^6 - 20\rho^4 + 6\rho^2) \sin 2\theta$
24	6	2	$\sqrt{14} (5\rho^6 - 20\rho^4 + 6\rho^2) \cos 2\theta$

.....contd.

$j$	$n$	$m$	$Z_j(\rho, \theta)$
25	6	4	$\sqrt{14} (6\rho^6 - 5\rho^4) \sin 4\theta$
26	6	4	$\sqrt{14} (6\rho^6 - 5\rho^4) \cos 4\theta$
27	6	6	$\sqrt{14}\rho^6 \sin 6\theta$
28	6	6	$\sqrt{14}\rho^6 \cos 6\theta$
29	7	1	$4 (35\rho^7 - 60\rho^5 + 30\rho^3 - 4\rho) \sin \theta$
30	7	1	$4 (35\rho^7 - 60\rho^5 + 30\rho^3 - 4\rho) \cos \theta$
31	7	3	$4 (21\rho^7 - 30\rho^5 + 10\rho^3) \sin 3\theta$
32	7	3	$4 (21\rho^7 - 30\rho^5 + 10\rho^3) \cos 3\theta$
33	7	5	$4 (\rho^7 - 6\rho^5) \sin 5\theta$
34	7	5	$4 (\rho^7 - 6\rho^5) \cos 5\theta$
35	7	7	$4\rho^7 \sin 7\theta$
36	7	7	$4\rho^7 \cos 7\theta$
37	8	0	$3 (10\rho^8 - 140\rho^6 + 90\rho^4 - 20\rho^2 + 1)$

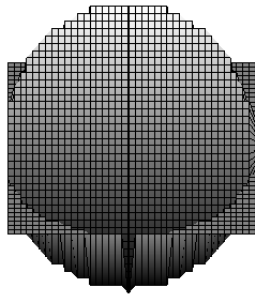
**Table 2.1 Zernike orthonormal polynomials  $Z_j$  for  $j = 1$  to 37,  $n$  is the radial order of the polynomial and  $m$  the azimuthal frequency. Index  $j$  is the polynomial ordering number and even  $j$  correspond to symmetric modes ( $\cos m\theta$ ) and odd  $j$  correspond to antisymmetric modes ( $\sin m\theta$ ).**

where

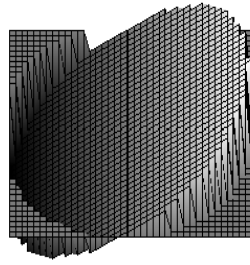
$$R_n^m(\rho) = \sum_{s=0}^{\frac{n-m}{2}} \frac{(-1)^s (n-s)!}{s! \left(\frac{n+m}{2} - s\right)! \left(\frac{n-m}{2} - s\right)!} \rho^{n-2s} \quad (2.18)$$

According to Noll's numbering system,  $j$  is used instead of  $n$ , the radial order and  $m$  the azimuthal order. The two indices  $m$  and  $n$  are whole

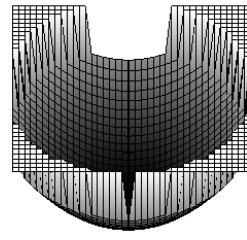
## Examples of Zernike Modes



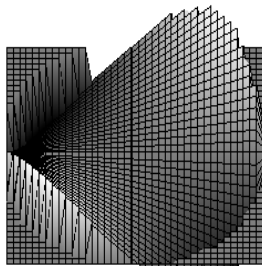
X-Tilt



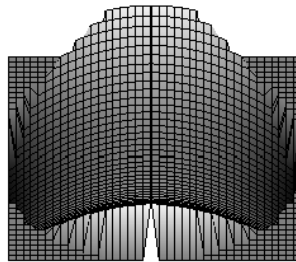
Y-Tilt



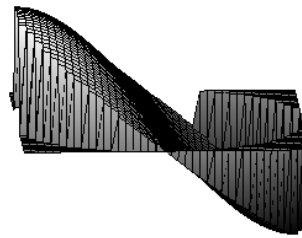
Defocus



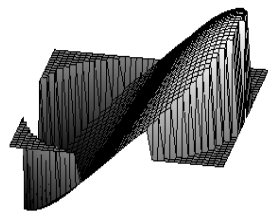
Astigmatism X



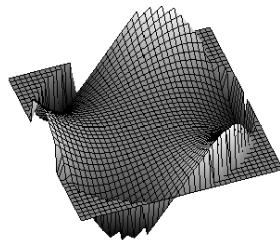
Astigmatism Y



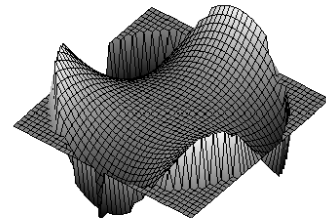
Primary Y Coma



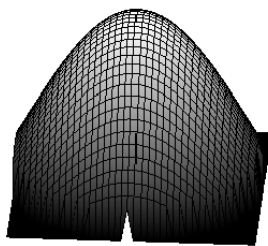
Primary X Coma



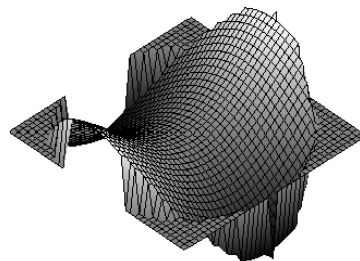
Triangular Coma X



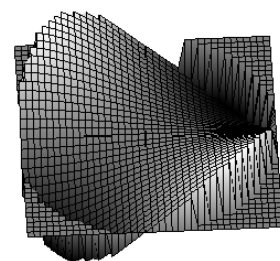
Triangular Coma Y



Spherical



Sec. Astigmatism X



Sec. Astigmatism Y

**Fig.2.4 Graphical representation of few Zernike modes**

numbers satisfying  $m \leq n$  and  $n-m$  is even. The total number of modes up to a given radial order is therefore

$$j_n = \frac{(n+1)(n+2)}{2} \quad (2.19)$$

The low order Zernike polynomials (Table 2.1), where the columns and rows indicate azimuthal and radial order respectively, and Figure 2.3 displays them graphically.

The polynomial expansion of an arbitrary wavefront  $\phi(\rho, \theta)$  over the unit circle is defined as

$$\phi(\rho, \theta) = \sum_{i=1}^{\infty} a_i Z_i(\rho, \theta) \quad (2.20)$$

and the coefficients  $a_i$ , are determined using the principle of orthogonality of polynomials as

$$a_i = \pi^{-1} \int \Phi(\rho, \theta) Z_j(\rho, \theta) \rho d\rho d\theta \quad (2.21)$$

Since Zernike polynomials have the unique property of representing each mode individually, one can estimate the contributions by the atmosphere by estimating the individual Zernike terms. The mean square value or the variance of the phase aberration is equal to infinity and the mean square residual phase error across the aperture can be written as

$$\sigma_{\phi}^2 = \langle \phi^2 \rangle - \sum_{j=1}^N \langle |a_j|^2 \rangle \quad (2.22)$$

However, the variance of the piston removed aberration is finite.

$$\begin{aligned} \Delta_1 &= \langle \Phi^2 \rangle - \langle a_1^2 \rangle \\ &= 1.0299(D/r_o)^{5/3} \end{aligned} \quad (2.23)$$

If the aberration be due to first “J” Zernike polynomials, it is written as

$$\phi_j(\rho, \theta) = \sum_{i=1}^J a_i Z_i(\rho, \theta) \quad (2.24)$$

Then the variance or the mean square residual error of the remaining aberrations can be expressed as

$$\begin{aligned}\Delta_J &= \pi^{-1} \iint \langle \phi(\rho, \theta) - \phi_J(\rho, \theta) \rangle^2 \rho d\rho d\theta \\ &= \Delta_1 - \sum_{j=2}^J \langle a_j^2 \rangle\end{aligned}\quad (2.25)$$

When no correction is applied then

$$\Delta_1 \equiv \sigma_\phi^2 = 1.0299(D/r_o)^{5/3} \Rightarrow \sigma_\phi = 1 \text{ radian when } D = r_o \quad (2.26)$$

In other words, the Fried's parameter is the diameter of the circle whose variance is equal to 1 rad<sup>2</sup>. Variance of the other residual phase errors contributed by the atmosphere in units of  $(D/r_o)^{5/3}$  is given in the Table 2.2

$\Delta_1=1.0299$	$\Delta_{12}=0.0352$
$\Delta_2=0.582$	$\Delta_{13}=0.0328$
$\Delta_3=0.134$	$\Delta_{14}=0.0304$
$\Delta_4=0.111$	$\Delta_{15}=0.0279$
$\Delta_5=0.0880$	$\Delta_{16}=0.0267$
$\Delta_6=0.0648$	$\Delta_{17}=0.0255$
$\Delta_7=0.0587$	$\Delta_{18}=0.0243$
$\Delta_8=0.0525$	$\Delta_{19}=0.0232$
$\Delta_9=0.0463$	$\Delta_{20}=0.0220$
$\Delta_{10}=0.0401$	$\Delta_{21}=0.0208$
$\Delta_{11}=0.0377$	$\Delta_J = 0.2944J^{-\sqrt{3}/2}$ (For large J)

**Table 2.2 The residual variance  $\Delta_j$  of Kolomogorov turbulence after after the first j modes are removed (Noll, 1976).**

It is seen that  $\Delta_j \propto J^{-\frac{\sqrt{3}}{2}} = J^{-0.87}$ , i.e. falls with  $J$ . But this fall not being sufficiently fast, one is required to keep sufficient number of Zernike polynomials. In the present work, it has been investigated up to 21 polynomials.

### 2.4.1 Phase Variance and Image quality

The final image quality is usually expressed in terms of Strehl ratio that defines the peak of the point spread function to the peak of the diffraction limited point spread function.

$$S = \frac{I(0,0)_{aberr}}{I(0,0)_{diff}} \quad (2.27)$$

Many approximations for the Strehl ratio have been investigated (Mahajan 1982, 1983) and the best approximation found was empirical and the Strehl ratio is related to the variance of the phase aberration across the pupil by

$$S = \exp(-\sigma_\phi^2) \quad (2.28)$$

For small arbitrary aberrations  $\sigma_\phi^2 \ll 1$ ,  $S = 1 - \sigma_\phi^2$

A system is well corrected when  $S \geq 0.8$ , the equality being called the Marechal criterion (Born and Wolf, 1980). At the Marechal limit

$$\sigma_\phi^2 = \left(\frac{2\pi}{\lambda}\right)^2 \sigma_w^2 = 0.2 \text{rad}^2 \quad (2.29)$$

corresponding to an rms wavefront aberration of  $\sigma_\phi = \frac{\lambda}{14}$  or a wavefront variance of  $\sigma_w^2 = \lambda^2 / 200$

# Chapter 3

## Adaptive Optics System and its Elements

The application of adaptive optics for improving image resolution and quality of large optical telescopes has revolutionized the approach to ground-based astronomy. Adaptive Optics (AO) is a technique that corrects the corrugated wavefront in a closed loop configuration to attain diffraction limited performance of the ground-based telescopes (Hardy 1998). It is a means for real time compensation of the image degradation. An AO system basically consists of three main components, a wavefront sensor, a wavefront corrector and a control system. A portion of the beam from the telescope is diverted to the wavefront sensor to estimate the aberrations induced in the beam due to atmospheric turbulence. The wavefront control system computes the control signals for the wavefront corrector and sends it to the correcting device. This servo loop is repeated continuously to get a corrected image. This chapter reviews the different components of the AO system. The schematic of an AO system is given in Figure 3.1.

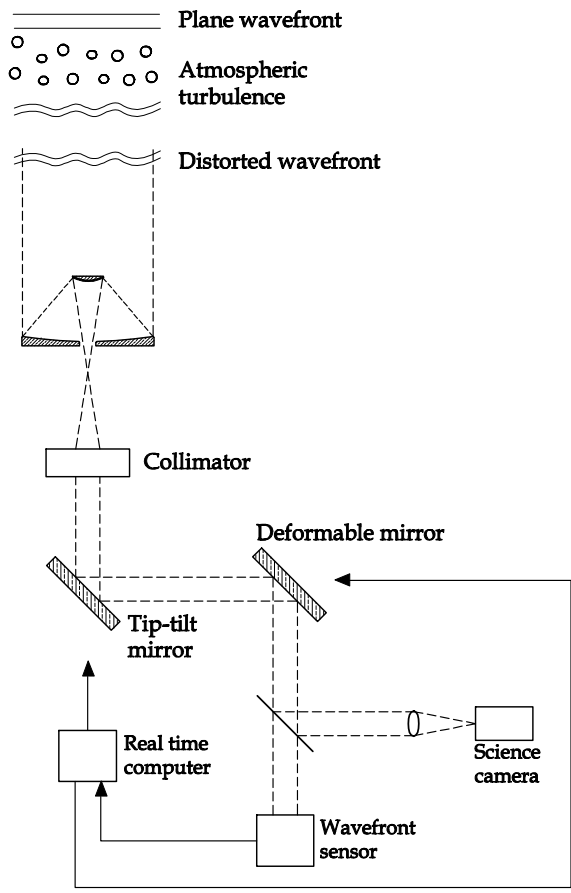


**Fig.3.1: Schematic of an Adaptive Optics System**

The main components for an adaptive optics system are: (1) Wavefront sensor, (2) tip-tilt mirror (3) deformable mirror, and (4) Wavefront controller. Wavefront sensor is the most critical part of the adaptive optics system. Effectiveness of the AO system directly relates to the accuracy and efficiency of the wavefront sensor.

**3.1 Wavefront Sensing**

A wavefront sensor is the heart of the adaptive optics system. A wavefront sensor provides the estimate of the wavefront distortion

produced by the telescope system and atmospheric turbulence at the pupil plane. It is of prime importance to evaluate the wavefront with enough spatial resolution and suitable speed for real time compensation. The wavefront sensor must efficiently use the star light. So it should preferably work on broad spectral band width. Secondly, the Wavefront sensor must use the photons efficiently. Thirdly, the wavefront sensor must be linear over the full range of atmospheric disturbances. Most sensors evaluate the wavefront gradients (the spatial first derivative) or the curvature (Laplacian) over an array of sub-apertures of the wavefront.

The performance of the wavefront sensor depends on the effective measurement of the errors in the incoming wavefront. Thus a highly accurate and efficient wavefront sensor is very much desirable. The present work is aimed at developing a simple and accurate wavefront sensing method suitable for such applications. Some of the existing methods commonly used have certain inherent shortcomings. The present method aims at versatility and improvement upon them.

### **3.1.1. Concept and Methods of Wavefront Sensing**

A comparative study of different wavefront sensing methods has been undertaken. This chapter outlines the basic concepts of some of the major wavefront sensing techniques that are currently used.

A wavefront sensing is to characterize the wavefront distorted by atmospheric turbulence and quantifying the parameters for real time correction. According to the diffraction theory the complex amplitude of the wave at the pupil plane of the telescope is given by

$$A(x,y) = \exp[-i 2\pi/\lambda W(x,y)] \quad (3.1)$$

The term  $\frac{2\pi}{\lambda} w(x,y)$  represents the phase of the propagating optical wave. The phase contains all the information of the aberrations of the system. It is impossible to estimate the phase directly. Nevertheless, it can be done using indirect methods. This can be done either at the focal plane or in the image/focal plane. The two fundamental methods of wavefront sensing are geometric and interferometric. The geometric methods are Shack Hartmann wavefront sensor, Curvature sensing etc. The interferometric methods are in general based on lateral shearing interferometry. It is also possible by deconvolution technique (Primot J. et al, 1990) to retrieve the wavefront from the turbulence degraded images. A general tutorial text on wavefront sensors is provided by Joseph Geary (1995).

### **3.1.2 Shack Hartmann Wavefront Sensor**

Presently Shack Hartmann (SH) method is the most commonly used method. It is the modified (Platt and Shack, 2001) and improved version of the Hartmann test used for large mirror testing. In the Hartmann test, a wavefront is sampled in a number of locations by means of an opaque screen with a set of holes placed at the telescope pupil. As a result, when light propagates through the holes, a set of spots is produced on the recording plane. The local slope of the wavefront at each sample point can be evaluated from the direction in which most of the light emerges from the corresponding hole, that is, from the spot position. It is based on the principle of displacement of the image due to the local slope in the wavefront (Tyson, 1991; Rousset, 1999).

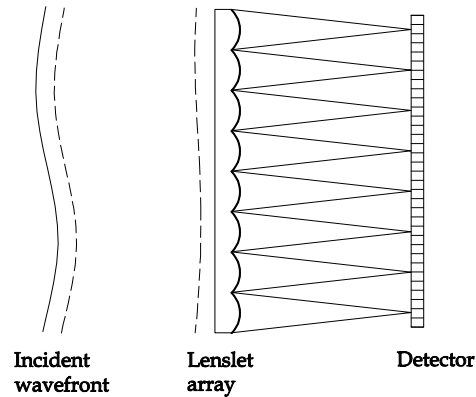


**Fig.3.2. Schematic of a Shack Hartmann sensor.**

In the Shack Hartmann sensor, an array of holes is replaced by a microlens array (Fig.3.2). The lenslet array is positioned in a plane conjugate to the telescope pupil, to sample the incoming wavefront. The incident wavefront is sampled into small sub-apertures using a lenslet array, which produces the Fraunhofer diffraction pattern corresponding to the wavefront sampling, on to the detector plane. If the incident wavefront is planar, then the lenslet forms an image at its focus. If, on the other hand the incident wavefront is distorted and non planar, then a portion of the distorted beam corresponding to each sub aperture, forms an off axis image in its focal plane. Measurement of the difference between the two image positions gives an estimate of the wavefront slope over the sub aperture. By measuring the displacements of the image in the  $x$  and  $y$  directions, an array of  $x$  slope and  $y$  slope estimates at the aperture is obtained. The slope of the wavefront is related as

$$x \text{ slope} = \frac{\Delta_x}{f \cdot M} \quad \& \quad y \text{ slope} = \frac{\Delta_y}{f \cdot M} \quad (3.2)$$

where  $f$  is the focal length of the lenslet and  $M$  is the magnification between the lenslet plane and telescope entrance plane.

Usually a CCD is used as a detector to record the images of the spots. The center of gravity of each spot is measured using the formula

$$g_x = \frac{\sum_{l,m} x_{l,m} I_{l,m}}{\sum_{l,m} I_{l,m}} \quad \text{and} \quad g_y = \frac{\sum_{l,m} y_{l,m} I_{l,m}}{\sum_{l,m} I_{l,m}} \quad (3.3)$$

Where  $x_{l,m}$  and  $I_{l,m}$  are the intensity and the position coordinates of the CCD pixel. The sum is made over all the pixels in the lenslet field and normalized over the signal. Hence, we measure a set of local slopes of the wavefront. Modal wavefront estimation using Zernike polynomials is one way in which the wavefront from the local slopes can be reconstructed.

The wavefront can be expressed by

$$w(x_i, y_i) = \sum_{j=0}^N C_j Z_j(x_i, y_i) \quad (3.4)$$

where the  $Z_i(x,y)$  are the Zernike polynomials and  $C_i$  are the coefficients of the Zernike modes. Several methods have been developed that are computationally stable. Solving the above matrix equation using Single Value Decomposition (SVD) method, the Zernike coefficients are evaluated. The entire wavefront can be estimated knowing the Zernike coefficients. The Shack Hartmann sensor suffers from low spatial frequency and the measurement noise arises from an uncertainty in the determination of centroid position of each spot and limited in terms of range and accuracy of measurement dictated by CCD performance and diffraction effects of the lenslet array. The wavefront estimation performance will be fundamentally limited by both the measurement technique and the noise propagation.

### 3.1.3 Curvature Wavefront Sensor

The curvature sensor (CS) has been proposed and developed by Roddier (1988) to make wavefront curvature measurement instead of wavefront slope measurements. In this, the wavefront sensor aims at measuring the second derivative of the wavefront slope. It measures the image at two locations, one before focus called *intrafocal* image and the other outside focus called *extrafocal* image (Fig.3.3). The intensity distributions of the images are a measure of wavefront curvature, i.e. its second derivative, in the telescope pupil.

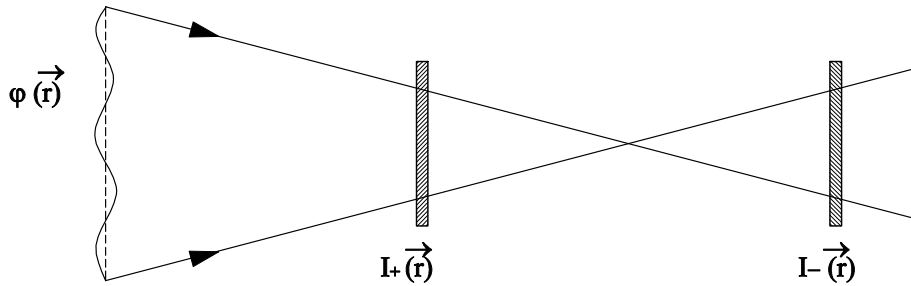


**Fig.3.3 Principle of Curvature sensor**

A local wavefront curvature in the pupil plane produces excess illumination, say in plane  $P_1$  and lack of illumination in plane  $P_2$ . On the pupil edge, the same difference between the two illuminations provides a measure of the radial tilt. In geometrical optics approximation, the normalized difference between the two intensity distributions is related to the wavefront phase  $\phi$  in the pupil plane by

$$\frac{I_1(r) - I_2(r)}{I_1(r) + I_2(r)} = \frac{f(f-l)}{2l} \left[ \frac{\partial}{\partial \rho} \phi(\rho, \theta) \delta_c - \nabla^2 \phi(\rho, \theta) \right] \quad (3.5)$$

where  $\delta_c$  is a linear impulse distribution around the pupil edge.  $I_1$  and  $I_2$  are the intensities in the two planes and  $\nabla^2$  is the Laplacian operator  $\frac{\partial^2 \phi}{\partial \rho^2}$  is the first derivative of the wavefront,  $f$ , the focal length of the telescope and  $l$  is the distance of the irradiance plane. It is the irradiance transport equation and the phase retrieval has been worked out by (Ichikawa et.al, 1988). The normalization of the difference in illumination makes the sensor insensitive to scintillation and works well for extended sources. In CS the choice of the distance  $l$  is very critical. To summarize, increasing the distance  $l$  increases spatial resolution on the wavefront measurement but decreases sensitivity. On the other hand, a smaller distance yields a higher sensitivity to low order aberrations.

### **3.1.4 Pyramid Wavefront Sensor**

The concept of pyramid wavefront sensor was suggested in the mid-1990s (Pugh et al, 1995) is based on the modified Focault knife edge test used in optical testing. This technique was later proposed in the familiar form by Ragazzoni (1996). Like Shack Hartmann sensor it measures the first derivative of the wavefront. A pyramid lens with four equal faces is placed with its vertex on the nominal focus of the optical system. The four faces deflect the beam in four different directions, depending on which face of the prism gets the incoming ray. A field lens is used to re-image the pupil of the telescope. In the pupil plane a CCD detector is used to measure the individual signals of the four faces (Fig.3.4).

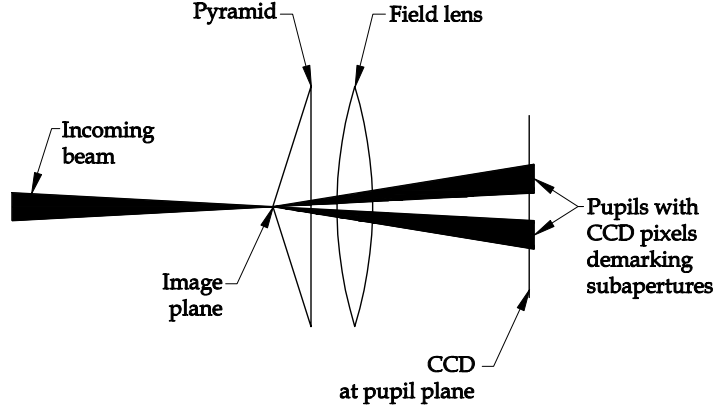


**Fig.3.4. Principle of Pyramid Sensor**

In order to improve the sensitivity Ragazzoni proposed to oscillate the pyramid to allow all the aberrated rays to sweep over the four faces. In such case, each face will receive a particular intensity of illumination that shall be proportional to the displacement of the rays with respect to the pyramid vertex. After an integer number of oscillation cycles, the four pupil signals  $I_1, I_2, I_3, I_4$  are combined and normalized by the sum. Hence it is possible to retrieve the derivatives or slopes  $\frac{\partial \psi(x, y)}{\partial x}$  and  $\frac{\partial \psi(x, y)}{\partial y}$  of the wavefront along two orthogonal axes.

$$\left| \frac{\partial \psi(r)}{\partial r} \right| = \delta \theta_x \frac{(I_1 + I_2) - (I_3 + I_4)}{I_1 + I_2 + I_3 + I_4} \frac{\partial \psi(x, y)}{\partial x} = \delta \theta_x \frac{(I_1 + I_4) - (I_2 + I_3)}{I_1 + I_2 + I_3 + I_4} \quad (3.6)$$

and

$$\frac{\partial \psi(x, y)}{\partial y} = \delta \theta_y \frac{(I_1 + I_2) - (I_3 + I_4)}{I_1 + I_2 + I_3 + I_4} \quad (3.7)$$

where  $\delta\theta_x$  and  $\delta\theta_y$  are the modulation introduced in the  $x$  and  $y$  directions such that

$\delta\theta > \left| \frac{\partial\psi(r)}{\partial r} \right|$ . More details on the calculations and improvement on the oscillation were done by Riccardi et al. (1998).

The work on pyramid sensor for adaptive optics application is reported in the literature (Esposito and Riccardi, 2001). The energy distribution of a pyramid wavefront sensor over the pupil is non-uniform. Most of the illumination is over the edges of the pupil leading to low signal to noise ratio. This adds more complication in the closed loop adaptive optics system and procedure is quite time consuming.

### **3.1.5 Shearing Interferometer Based Wavefront Sensor**

Shearing interferometry is another technique to measure wavefront phase through intensity measurements (Sandler et al, 1994) for adaptive optics applications. The basic approach is to produce an interference pattern between the wavefront and a sheared or displaced replica of itself. In this way, the phase variations, which cannot be measured directly because of its high temporal frequency, are converted into intensity variations (fringe pattern) in the pupil plane. Shearing interferometry is self-referencing and does not require a coherent reference source. Like SH sensor, Shearing interferometry measures the wavefront slope.

A wavefront may be sheared in different ways.

- a. *Laterally*, by displacing the wavefront a replica by a fraction of the aperture and made to interfere.
- b. *Rotationally*, by rotation of the replica wavefront by an angle and combining it keeping the same origin.

c. *Radially*, by magnifying a replica and combining it with the original wavefront.

The lateral shearing interferometer (Wyant, 1975) is the most commonly used method for real time wavefront correction systems. Lateral shear can be produced in many ways. A wavefront  $e^{ikw(x,y)}$  is sheared by a small amount  $\Delta x$  and made to interfere by itself. A schematic of lateral shearing of wavefront is shown in figure 3.5.

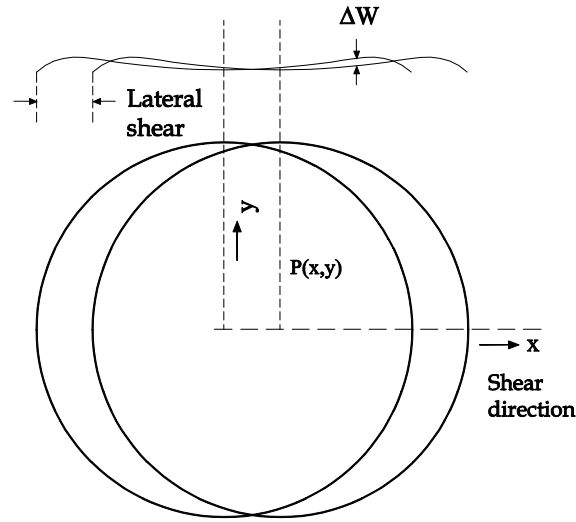


**Fig.3.5 A schematic representation of the lateral shearing of the wavefront.**

The interference pattern  $I(x,y)$  of the interferogram can be written as

$$I(x,y) = \exp\left\{ikw\left(x - \frac{\Delta x}{2}\right), y\right\} + \exp\left\{ikw\left(x + \frac{\Delta x}{2}\right), y\right\} \quad (3.8)$$

where the wavefront is sheared in the x direction by  $\Delta x/2$

Expanding and simplifying

$$I(x,y) = A \cos\left(k \frac{\partial w}{\partial x} \Delta x\right) \quad (3.9)$$

The phase in the cosine term is directly proportional to the slope of the wavefront at the measured position. To reconstruct the complete wavefront, the data containing x shear and y shear are required. In such

cases, one needs to obtain two interferometric records. There are many ways to produce a shearing wavefront. The text book on optical testing by Malacara (1992) gives a detailed account of the shearing interferometers used for optical testing. Shearing interferometer offers better choice for its linearity, better signal processing and added spatial information. The suggested methods employ refraction or reflection to produce two interfering beams and the optical system generates fringes whose period is proportional to wavelength, restricting operation to lower spectral band width.

Birefringent crystals are the best suitable optical devices to provide shearing wavefronts. An efficient approach is to separate the two orthogonally polarized beams and analyzing the beams using an analyzer. Shearing interferometer using birefringent prisms have been described by Saxena (1979), Hardy & Mac Govern (1987), and Sandler et al.(1994) particularly for AO applications.

### **3.2 Wavefront correcting system**

The wavefront corrector is a component in the adaptive optics train which is used to compensate for any aberrations due to atmosphere or imperfections in the telescope optics. The corrector is an electro-opto-mechanical device and the physical movement is proportional to the applied voltage. There are basically two different types of wavefront correctors presently in use to correct two distinct ranges of frequencies. Following text gives a brief account of the wavefront correctors used in AO system. In the recent past, many new developments have taken place in the manufacturing of flexible and micro-electro-mechanical based correcting devices. Since, the aim of the thesis is on wavefront sensing, only a brief account of the tip-tilt mirrors and deformable mirrors are given for the sake of completeness.

### 3.2.1 Tip-tilt Mirror:

The simplest form of adaptive optics is *tip-tilt* correction, which corresponds to correction of the tilts of the wavefront in two dimensions. This is performed using a rapidly moving tip-tilt mirror which makes small rotations around two of its axes. A significant fraction of the aberration introduced by the atmosphere can be removed in this way. Tip-tilt mirrors are widely used in stellar and solar imaging, to correct the aberrations introduced by the atmosphere on the light path and to improve the image quality over the aperture. Tip-tilt mirrors are effectively segmented piezo-electric actuator driven by external voltage having only one segment which can tip and tilt, rather than having an array of multiple segments which can tip and tilt independently. Basically, the actuators operate in push pull mode.

A tip-tilt mirror is introduced in the optical path of the telescope as shown in Fig.1.1. The tip tilt mirror corrects the wandering of the center of the seeing disc and its frequency is in the order of 50Hz. It may be required to give a stroke typically few tens of microns peak to peak. Tip tilt mirrors generally cannot correct rapid fluctuations in the wavefront provide medium or low bandwidth pointing in real time.

### 3.2.2 Deformable Mirror

The residual phase errors are corrected by the use of deformable mirrors (DM). They are made of a very thin mirror whose shape can be changed by the force applied by many actuators stacked behind the mirror. For astronomical purposes, the number of actuators that a DM should possess, is proportional to

$$N = D/r_o^2 \quad (3.10)$$

where  $D$  is the telescope diameter and  $r_o$  is the Fried's parameter. The required stroke ranges to a few microns. The response time  $\tau$  typically, is the time to sweep the turbulence cell pattern across the Fried distance  $r_o$  by the mean wind velocity. This makes proportional  $\tau \propto r_o/v$ , where  $v$  is the velocity of the wind, and its value is in the order of few milliseconds. Individual voltages are applied to the actuators to change the shape of the DM described by its influence function.

Several types of deformable mirrors have been made. Some of the important features of the deformable mirrors are discussed here.

*segmented mirror* consists of an array of single tip-tilt elements. The single elements can be moved independent of each other and they can be replaced easily. The motion of the individual mirrors is restricted to piston and tilt. The main drawback of this mirror is high fitting error and edge diffraction effects induced by gaps between segments. *Bimorph mirrors* consist of two piezoelectric wafers which are bonded together and oppositely polarized, parallel to their axes. An array of electrodes is deposited between the two wafers. When a voltage is applied to the Piezoelectric Transducer (PZT) material it expands in area as in a bimetallic strip. The curvature of the surface is proportional to the applied voltage.

*Membrane mirror* consist of a thin reflecting membrane stretched over a ring and deformed by means of electrostatic forces in a partial vacuum chamber.

$$\nabla^2 Z(x, y) = -P(x, y)/T_m \quad (3.11)$$

where  $Z(x, y)$  is the deformation of the membrane,  $P(x, y)$  is the pressure and  $T_m$  is the tension of the membrane. The effect of applying a local pressure is to change the local curvature of the membrane.

### **3.3 Wavefront Controller:**

An adaptive optics system can be defined as a closed loop servo system. Wavefront sensors measure the shape of the wavefront and produce signals that represent the wavefront. It may be modal or zonal representation. It is the function of the controller to translate these signals and relay them to the correcting device. In most cases, parallel paths are employed whereby one channel controls lower order aberration modes, such as focus and tilt while another channel simultaneously controls the higher order wavefront errors with deformable mirror.

The functions of the controller can be described in two parts. In the first part, the wavefront is reconstructed from the input signals from the wavefront sensor on the basis of deformable mirror actuators geometry. It estimates the control vector containing the control voltages, which are to be fed to the tip-tilt and deformable mirror. The second stage, involves the hardware using digital to analog converters, control voltages are generated and fed to the tip-tilt and deformable mirrors to enable the required correction. Although, adaptive optics control systems often analyze and direct many parallel channels of information, most of the systems in practice are based on single channel linear processing algorithms. Advancement of digital computers allows the parallel operations to be performed at very high speed.

# Chapter 4

## **Polarization Shearing Interferometer based wavefront sensor**

Adaptive Optic systems measure and correct errors in optical systems by using a wavefront sensor combined with a deformable mirror and appropriate control hardware and software. Three main wavefront sensing techniques are outlined in the previous chapter. Of these, Shack Hartmann method is most widely used by different groups around the world.

Various methods of shearing interferometry have been devised for optical testing (Malacara, 1992). The use of shearing interferometry has been studied extensively since 1970s for phase measurement of the atmospheric turbulence. Hardy and Mac Govern (1987) mention in their article that an efficient approach for shearing interferometry is to separate two beam by polarization using birefringent prisms. This class of interferometers is called Polarization interferometers (Francon and Mallick, 1971). The use of birefringent prisms as a lateral shearing interferometer (Saxena, 1979, Malacara, 1992, Hyun-Ho Lee et. al, 2003) for optical testing has been extensively reported in the literature. In order to reconstruct a two-dimensional wavefront, it is necessary to measure the slope in two directions separately. Lateral Shearing Interferometers (LSI) normally uses two orthogonal shear directions. The present work

reported in this thesis is devoted to the development of a Polarization Shearing Interferometer (PSI) based on the use of a Babinet Compensator (BC) as a wavefront shearing device where a single interferogram can provide complete information about the incident wavefront. This chapter describes the basic use of single BC and subsequently a suitable scheme for the use of two crossed Babinet Compensators for PSI based wavefront sensing. Necessary theory has been presented based on Fourier optics to establish that a single interferogram can be efficiently used as a wavefront sensor.

#### **4.1 Babinet Compensator (BC)**

The Babinet Compensator (BC) was invented in the nineteenth century by Jacques Babinet, a French physicist, mathematician and an astronomer, who used this device for the study of polarized light in microscopy. The Babinet Compensator is widely used as an effective optical device for the measurement of retardation between the ordinary ray (o) and extraordinary ray (e) i.e. to study the degree of birefringence. A Babinet Compensator can be adjusted to provide a variable path difference. The BC has been exploited for accurate measurement of phase differences (Hariharan and Sen, 1960) and for the evaluation of aspheric surfaces (Saxena, 1979). The Babinet Compensator consists of paired quartz wedges, of small wedge angle, which are cut in such a fashion that one is positioned with the optic axis parallel to the edge, while the other has the axis perpendicular to the edge (Fig.4.1). When the two wedges are optically cemented they act as a plane parallel plate of thickness  $h$ . The theory of the Babinet Compensator using Jones Calculus and the criteria for proper choice of the compensator parameters has been worked out in detail (Pandya and Saxena, 1978).

### Optical axis of the system

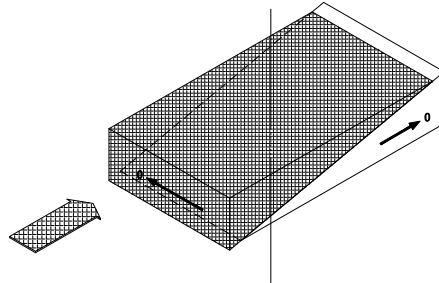


**Fig.4.1 A Babinet Compensator prisms showing the preferential direction of the optic axis in each prism.**

As can be seen from figure 4.1 the optical path difference in each wedge increases from the edge to the base and the birefringence has opposite values in the wedges. The extraordinary axes of the two plates are perpendicular to each other so the roles of the ordinary and extraordinary ray are reversed as the light travels through one plate and then the other. A phase difference or retardation that is accumulated in first wedge may be partially or completely canceled out by second wedge.

Let  $n_e$  and  $n_o$  be the ordinary and extraordinary refractive indices of quartz and  $h_1$  and  $h_2$  be the thickness of the two wedges at some particular point. When two wedges are combined and on passing through both wedges, the phase difference between the two rays is

$$\delta = \frac{2\pi}{\lambda} (n_e - n_o)(h_1 - h_2) \quad (4.1)$$

A dark fringe appears where the net optical phase difference through the compensator becomes zero and a bright fringe when the phase difference is  $\pi$  and continues in a direction at right angles to the zero line as the distance increases. Between crossed polarizers, dark and bright bands

are observed in monochromatic light at a separation distance of one wavelength of optical path difference. A typical fringe BC fringe pattern is shown in figure 4.2.

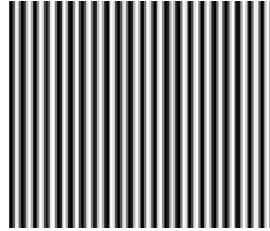


**Fig.4.2. Typical view of the fringes seen in collimated monochromatic light from a Babinet Compensator when placed between two crossed polarizers. Fringes are equally spaced and depend upon the wedge angle of the prisms.**

The intensity is given as

$$I \propto \sin^2(\delta_1 - \delta_2) \quad (4.2)$$

where  $\delta_1$  and  $\delta_2$  are the phase differences introduced by the wedges 1 and 2 respectively. In white light, the polarization colors appear in rising orders. In polarized light microscopy, measurements are conducted by observing the fringe shift caused by the addition of the optical path difference of the specimen under observation. In optical testing the fringe shifts and the shape changes due to the change of phase of the incoming wavefront provides the estimate of the wavefront errors.

Important conclusions drawn from this study (Pandya and Saxena, 1978) are included here for the proper choice of the BC components and precautions for the use. For any accurate quantitative application, the various possible defects have to be taken into account and their effects on the performance of the compensator have to be evaluated. These

defects can be classified into (i) Defective Polaroid (ii) Misalignment of polaroids, (iii) Fabrication defects. The compensator should be examined for the presence of fabrication defects. These are readily revealed by the appearance of fringes when is mounted at the azimuth of zero or  $\pi/2$  with respect to the crossed polaroids. It should then be arranged at an azimuth of  $\pi/4$  with respect to the polaroids for optimum sensitivity. The polaroids pair should be carefully chosen so as to satisfy the criterion the values of  $P_{\parallel}$  and  $P_{\perp}$  should be 0.9 and 0.1 for the range of wavelength used in the investigation. The accuracy in the crossing the polaroids, however, is not critical.

## **4.2. Polarization Shearing Interferometer (PSI) using single BC for the evaluation of surface/wavefront errors**

The single Babinet Compensator has been effectively exploited for testing concave aspheric surfaces (Saxena, 1979). The theory of the method and its effectiveness for detecting small surface errors was demonstrated in this paper. A schematic of the optical set up for testing a concave aspheric surface using single BC is shown in Fig.4.3. In this arrangement, a cone of light from a source, kept at the radius of curvature, is incident on the test surface and after reflection passes through the Babinet Compensator, placed between the polarizer and analyzer. At the focal point F2 one observes a fringe pattern due to the different phase changes introduced between extraordinary (e) and ordinary (o) vibrations at different points during the oblique passage of the ray.

The phase difference  $\delta$  in this case is given by

$$\delta = \frac{2\pi}{\lambda}(n_e - n_o)(d_1 - d_2) \quad (4.3)$$

Where  $d_1$  and  $d_2$  are the actual path lengths through the wedges respectively. A small error in the mirror surface alters the phase of the

incident beam. The fringe pattern represents the phase changes due to the errors present at the pupil plane. The number of fringes seen at the observation plane is also proportional to the distance of the Babinet compensator from the focus F2.

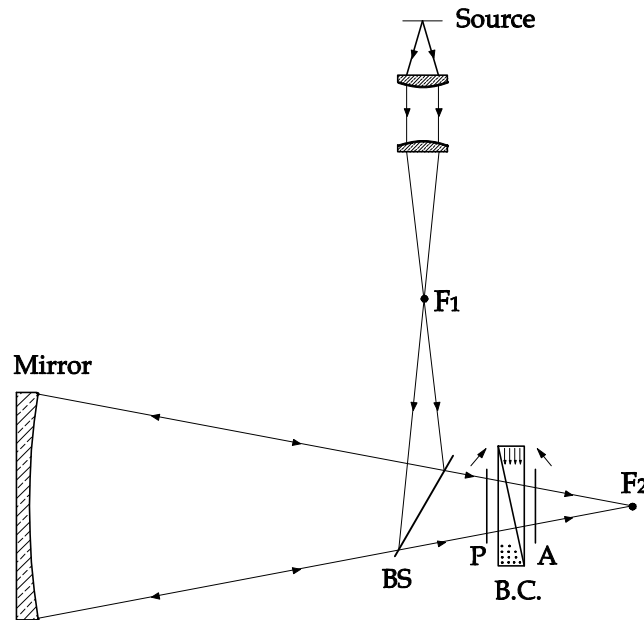


**Fig.4.3 A schematic of the optical setup for testing a concave mirror using a single Babinet Compensator. A lens (not shown) is used to image the mirror plane on to the detector.**

The shear introduced by the BC is given by

$$S = 2 (n_e - n_o) \tan \alpha R \quad (4.4)$$

where  $n_e$  and  $n_o$  are the refractive indices for the extraordinary and ordinary rays of the birefringent material,  $S$  is the amount of shear and  $\alpha$  is the wedge angle of the BC and  $R$  is the Radius of curvature of the mirror under test. A wavefront is considered to be nearly spherical of radius  $R$  so that the wavefront errors may be regarded as small deviations from its sphericity. The wavefront may be expressed as  $W(x,y)$  over the aperture. When the wavefront is sheared by an amount  $s$  the

error at a point  $x,y$  is  $W(x-s,y)$ . This is illustrated in Fig.3.5. The resulting path difference  $W(x,y) - W(x-s,y) = \Delta W(x,y)$  which is equal to  $n\lambda$ . When  $s$  is small the wavefront error may be written as  $\frac{\partial w}{\partial x} s$ . Thus

$$\Delta W(x,y) s = n\lambda \quad (4.5)$$

Considering a specific situation for primary aberrations for  $W(x,y)$  it can be written as

$$W(x, y) = A(x^2 + y^2)^2 + By((x^2 + y^2) + C(x^2 + 3y^2) + D(x^2 + y^2) + Ey + Fx \quad (4.6)$$

The wavefront error for defocusing may be written as

$$W(x, y) = D(x^2 + y^2) \quad (4.7)$$

In this situation

$$\frac{\partial w}{\partial x} s = 2Dxs \quad (4.8)$$

The defocusing coefficient is given by

$$D = \frac{R_o - l}{2R_o^2} = \frac{d}{2R_o^2} \quad (4.9)$$

The shape, spacing and position of these bright and dark fringes will depend upon the wavelength of light used, incoming phase of the wavefront and the physical properties of the compensator. A typical fringe pattern is shown in Figure 4.4.

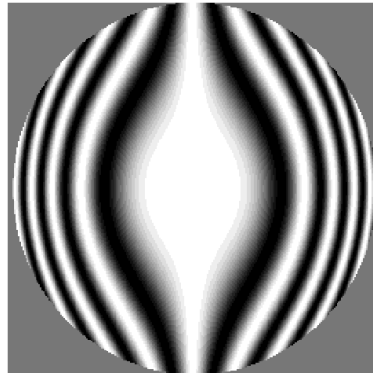


**Fig.4.4. Typical interferogram using single Babinet compensator for an aspheric surface. BC is placed inside focus of the convergent beam.**

Besides, the number of fringes will depend upon the distance of the BC from the vertex of the test mirror and the angle at which the rays are traversing through it. A detailed geometrical theory is explained in the literature (Jerrard, 1949). The surface departures of the test optics are evaluated by determining the difference between the positions of the fringes from the test optics to the true one. The sensitivity of this instrument also has been explained. It has been shown that with suitable precautions, the minimum detectable phase change that can be measured is as low as  $2\pi$  milli-radians.

### **4.3. Polarization Shearing Interferometer using two crossed BC**

Saxena and Jayarajan (1980) has proposed an alternative approach by using two crossed Babinet compensators for optical testing of aspheric surfaces. A typical arrangement of the two crossed BC is shown in Figure 4.5.

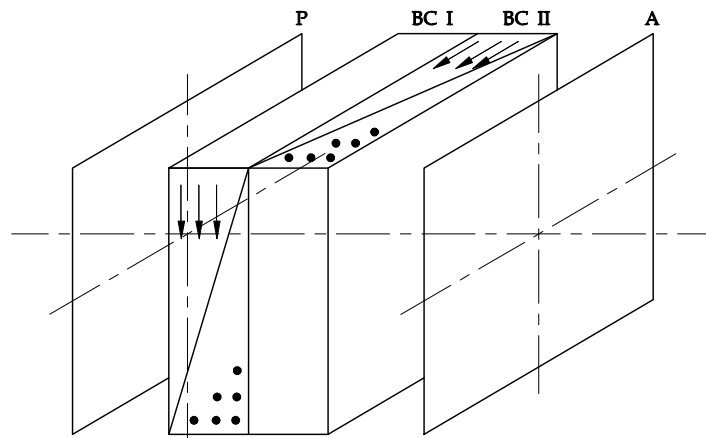


**Fig.4.5 Two crossed Babinet Compensator arrangement**

The two identical Babinet compensators are placed closed to one another with their preferential optic axes are crossed to each other. A typical optical test set up for testing a concave mirror is shown in Figure 4.6. In the optical set up a point source of light, kept at the radius of curvature of the test mirror, is made to incident on the test mirror and up on reflection passes through the two Babinet compensators which are placed on either side of the focus  $F_2$ . The two compensators are crossed to one another and they are placed at a distance  $d_1$  and  $d_2$  from the focus  $F_2$ . The sheared wavefronts in two orthogonal directions gives an interference pattern with fringes oriented at  $45^\circ$  in the observation plane. The fringe width also reduced to half the value obtained from individual compensators. In optical testing, the interferometric fringes are the true representation of the characteristics of the test mirror in the observation plane. The resultant path difference  $\Delta W$  is due to the path difference between the sheared wavefront and the original wavefront and the phase difference is

$$\delta = \frac{2\pi}{\lambda} \Delta w(x, y) \quad (4.10)$$

The resultant interferogram is due to the shearing of the wavefronts in two orthogonal directions. The geometrical approach (Saxena and Lancelot, 1982) for the formation of fringes is discussed in the following section.

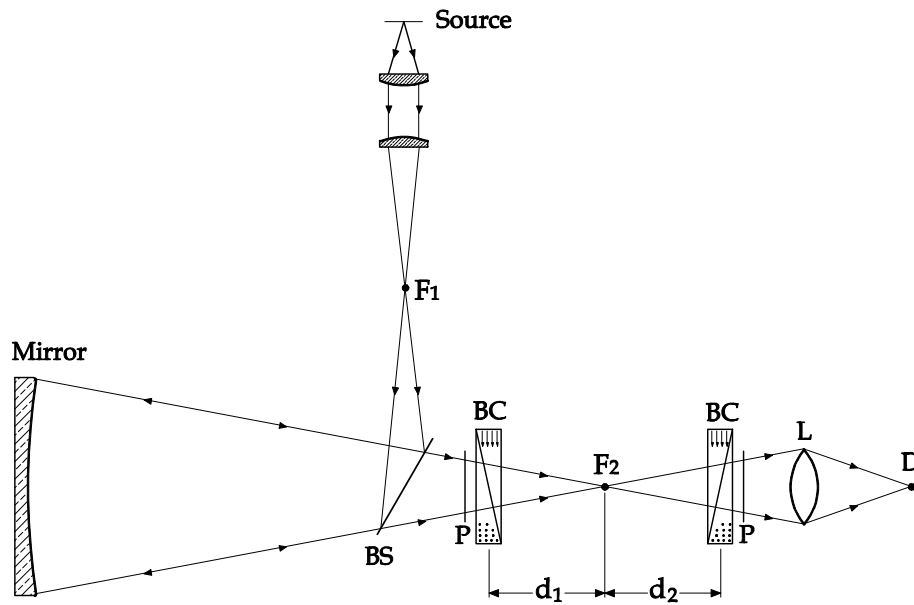


**Fig.4.6 A schematic of the optical set up for testing a concave mirror using two crossed Babinet Compensator. Note that the two compensators are placed on either side of the focus  $F_2$ . Optic axes are shown parallel for figure clarity. For actual measurement BC2 is to be rotated by  $90^\circ$ . Lens L images the mirror surface (pupil plane) on the detector.**

#### **4.3.1 A Geometrical approach for the fringes**

In the optical set up shown in Fig. 4.6 the compensators are placed on each side of the paraxial center of curvature with the line of equal thickness at right angles to each other and coinciding with the X and Y coordinate axes respectively. The two compensators are located at distances  $l_1$  and  $l_2$  from the mirror vertex, such that the distance from the paraxial center of curvature is given by  $d_1 = R_o - l_1$  and  $d_2 = R_o - l_2$ . Since the two compensators produce shear in two mutually perpendicular directions, one along the X axis and the other along the Y

axis, location of the bright fringes in the resulting interferogram can be represented by

$$\frac{\partial w}{\partial x} s + \frac{\partial w}{\partial y} t = n\lambda \quad (4.11)$$

where  $s$  and  $t$  are the shear in X and Y directions respectively, given by

$$s = 2(n_e - n_o) \tan \alpha_1 R_o \quad \text{and} \quad t = 2(n_e - n_o) \tan \alpha_2 R_o \quad (4.12)$$

where  $n_e$  &  $n_o$  are the refractive indices of the extraordinary and ordinary rays,  $\alpha_1$  &  $\alpha_2$  are the wedge angles of the compensators and  $R_o$  is the radius of curvature of the system. If they are two identical compensators having equal wedge angles then,  $\alpha_1 = \alpha_2 = \alpha$ ; in such case the amount of shear in both the X and Y directions are same.

$$s = t = 2(n_e - n_o) \tan \alpha R_o \quad (4.13)$$

Considering the primary aberrations and specifically in the case of defocusing the equation becomes

$$D_1 = \frac{R_o - l_1}{2R_o^2} = \frac{d_1}{2R_o^2} \quad (4.14)$$

$$D_2 = \frac{R_o - l_2}{2R_o^2} = \frac{d_2}{2R_o^2} \quad (4.15)$$

When only defocusing error is present, the wavefront error can be written as

$$\Delta W(x, y) = 2D_1xs + 2D_2yt \quad (4.16)$$

where  $D_1$  and  $D_2$  are the defocus coefficients. Hence, from equation 4.2 the intensity at the detector plane is

$$I(x, y) \propto \sin^2 \left( \frac{2\pi}{\lambda} \Delta w(x, y) \right) \quad (4.17)$$

More comprehensive interferograms for different aberrations are presented in chapter 5.

#### **4.3.2 A Fourier approach for the fringes**

In the following section, a mathematical treatment for the two crossed BC is being dealt with. The amplitude transmittance function for a plane wavefront in the case of a single BC has been worked out by Pandya and Saxena (1978) using Jones calculus. By extending their approach to a most generalized expression for the amplitude transmission function for two crossed BC the equation can be written as

$$M(x, y) = a_o \exp[i2\pi\{x/d_1 + y/d_2\}] + b_o \exp[-i2\pi\{x/d_1 + y/d_2\}] \quad (4.18)$$

where  $a_o$  and  $b_o$  are the constants taking into account the imperfections in polarizer and analyzer,  $d_1$  and  $d_2$  are the respective half fringe widths for the two compensators obtained with a plane wavefront ( Saxena and Lancelot, 1990).

The complex amplitude at the pupil plane is

$$U(x_o, y_o) = P(x_o, y_o) \exp \left\{ i \frac{2\pi}{\lambda} W(x_o, y_o) \right\} \quad (4.19)$$

where  $P(x_o, y_o) = 1$  inside the pupil

= 0 outside the pupil

$W(x_o, y_o)$  is the wavefront aberration in units of wavelength

The complex amplitude function after the BC is given by

$$U(x', y') = \tilde{U}(x', y') M(x', y') \quad (4.20)$$

where  $\tilde{U}(x', y')$  is the Fourier transform of  $U(x_o, y_o)$

The amplitude distribution at the detector plane can be taken as the convolution of  $U(x_o, y_o)$  with the Fourier transform of  $M(x', y')$ . On substitution it gives

$$U(x_1, y_1) = a_o \left[ \exp i 2\pi / \lambda \left\{ W \left( x_1 + \frac{\lambda f}{d_1}, y_1 + \frac{\lambda f}{d_2} \right) \right\} \right] + b_o \left[ \exp -i 2\pi / \lambda \left\{ W \left( x_1 - \frac{\lambda f}{d_1}, y_1 - \frac{\lambda f}{d_2} \right) \right\} \right] \quad (4.21)$$

and the Intensity

$$I(x_1, y_1) = U(x_1, y_1) U^*(x_1, y_1) \quad (4.22)$$

$$I(x_1, y_1) = a_o^2 + b_o^2 + 2a_o b_o \cos \left[ \frac{2\pi}{\lambda} \left\{ W \left( x_1 + \frac{\lambda f}{d_1}, y_1 + \frac{\lambda f}{d_2} \right) - W \left( x_1 - \frac{\lambda f}{d_1}, y_1 - \frac{\lambda f}{d_2} \right) \right\} \right] \quad (4.23)$$

$$I(x_1, y_1) = a_o^2 + b_o^2 + 2a_o b_o \cos \left[ \frac{2\pi}{\lambda} \left\{ W \left( x_1 + \frac{s}{2}, y_1 + \frac{t}{2} \right) - W \left( x_1 - \frac{s}{2}, y_1 - \frac{t}{2} \right) \right\} \right] \quad (4.24)$$

where  $s$  and  $t$  are the shear introduced by the two BC in two orthogonal directions respectively.

Defining

$a_o^2 + b_o^2 = K_o$  and  $2a_o b_o = K_1$ ; it can be rewritten as

$$I(x_1, y_1) = K_o + K_1 \cos \left( \frac{2\pi}{\lambda} \Delta W \right) \quad (4.25)$$

where  $\Delta W = \left\{ W \left( x_1 + \frac{s}{2}, y_1 + \frac{t}{2} \right) - W \left( x_1 - \frac{s}{2}, y_1 - \frac{t}{2} \right) \right\}$

and  $K_o$  is the constant background intensity and  $K_1$  is the modulation factor. Equation 4.25 gives the most generalized equation of the two crossed Babinet Compensator polarizing shearing interferogram.

The equation 4.25 represents a familiar interferometric expression for cosine fringes and it is the same representation of the equation obtained through geometrical approach.

$$I(x, y) = K_o + K_1 \cos \phi(x, y) \quad (4.26)$$

where the phase  $\phi(x, y)$  contains the desired information of wavefront slope and  $K_o$  and  $K_1$  represent the background intensity and the modulation of the cosine fringes respectively. In this case there is no requirement of carrier frequency to identify the actual phase of the original wavefront. The phase term itself contains the carrier frequency

which is represented by the defocus term as explained in the text before. Hence, compared to many other shearing interferometers, this PSI does not need any other external carrier frequency and thereby eliminates one source of error due to carrier frequency. Deriving the phase factor from the cosine fringes yields the derivative of the actual phase of the incident beam.

#### **4.4 Accuracy of the Phase measurement using BC based PSI**

The accuracy of the phase measurement of the BC based Polarization Shearing Interferometers depends primarily on the value of wedge angle of the BC and also governed by the factors explained in section 4.1. In the proposed intensity mode of operation accuracy and sensitivity of the measurement will also depend on the dynamic range of the detector. By suitable choice of the BC parameters, with due precautions and using a 10 bit accuracy of the detector, local phase errors at any point of the wavefront can be estimated to a close theoretical limit of  $2\pi$  milli radians or  $\lambda/1000$  wavefront errors.

The application of this method for wavefront sensing in reference to AO systems and the method of phase retrieval from single interferometric fringe record, is explained in the later chapters.

# Chapter 5

## Theoretical Simulations

This chapter deals with the theoretical simulations of the proposed wavefront sensor for adaptive optics application. In a telescope imaging system, the major sources of error, is from the atmospheric turbulence apart from other sources like, fabrication error and noise. A wavefront sensor computes these wavefront errors in real time and sends the signals for the control computer for adaptive correction. It is important to understand the Polarization Shearing Interferometer theoretically and its efficacy to sense the wavefront errors and its limitations. A systematic theoretical study has been undertaken. In the first part of the section, explanations about the simulations that were carried out with specific case of wavefront errors or primary aberrations of an optical system with respect to the Polarization Shearing Interferometer wavefront sensor is given. In the later part, the wavefront was generated using Zernike polynomials and the wavefront errors caused due to atmospheric turbulence was incorporated. The errors due to the fabrication in terms of ripple and the noise were also simulated and presented. From these simulation studies the optimum parameters for which the PSI wavefront sensor could be used in AO system has been derived. The theoretical simulation helps one to understand the behavior

of the fringe patterns in different circumstances. Simulations were also carried out with varying noise levels and atmospheric turbulence.

## 5.1 Basis of theoretical simulation

A simple wavefront equation having third order aberrations as derived by Kingslake (1978) is given below

$$W(x, y) = A(x^2 + y^2)^2 + By((x^2 + y^2) + C(x^2 + 3y^2) + D(x^2 + y^2) + Ey + Fx \quad (5.1)$$

- where A    Primary Spherical aberration  
 B        Primary Coma  
 C        Primary Astigmatism  
 D        Defocus  
 E        Tilt in X direction  
 F        Tilt in Y direction

When the shear value in X and Y directions are small, the shearing wavefront can be approximated as the first order derivative function as

$$\Delta W = \frac{\partial W}{\partial x}s + \frac{\partial W}{\partial y}t \quad (5.2)$$

where  $s$  and  $t$  are the shears in the  $x$  and  $y$  directions respectively. The intensity at the detector plane (eqn.4.25) can be written as

$$I = K_o + K_1 \cos\left(\frac{2\pi}{\lambda} \Delta W(x, y)\right) \quad (5.3)$$

The fringes in the observing plane or the detector plane, is due to the gradient of the wavefront errors expressed by  $\Delta W(x, y)$ . Simulations were carried using IDL and LABVIEW. In the later part of the chapter the simulations using Zernike polynomials were carried out taking into account the errors due to atmospheric turbulence.

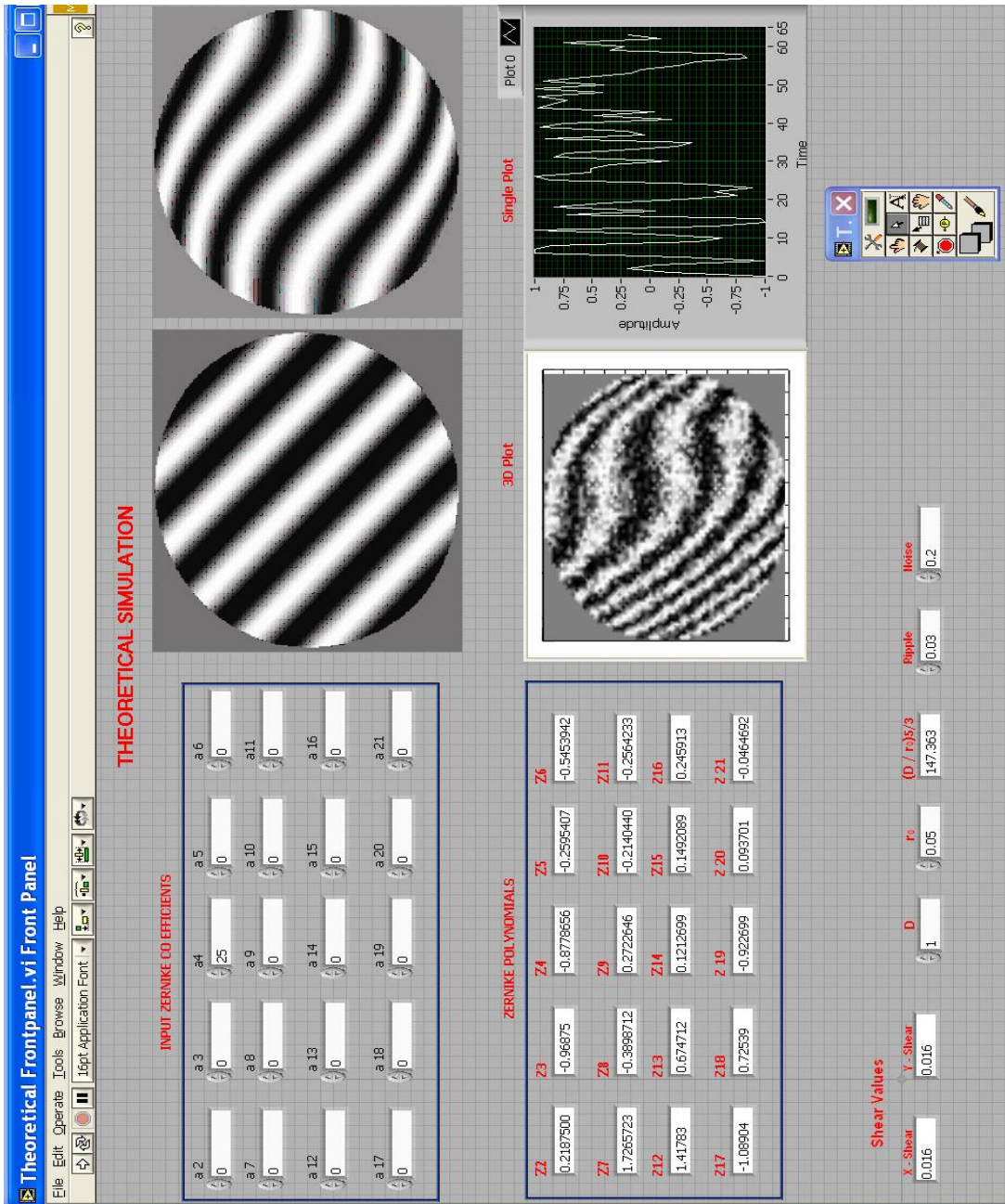


**Fig. 5.1 Front Panel of the Lab VIEW for the theoretical simulation of PSI records.**

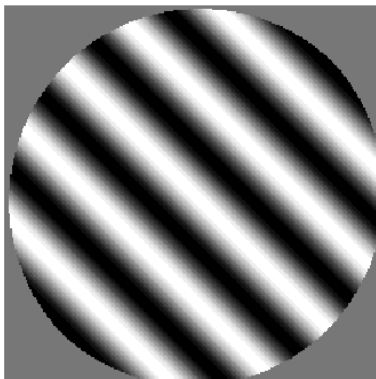
## 5.2 Fringe Profiles in ideal conditions

In the case of Polarization Shearing Interferogram, the ideal conditions are described as the system having no aberrations but only defocus term. The defocus in this case means the distance between the Babinet Compensators and the focus. Considering the equation 5.1 for the general wavefront, the sheared wavefront for various aberrations can be written. Keeping only the defocus and taking the other coefficients A, B, C, E & F equal to zero, the wavefront derivative takes the form,

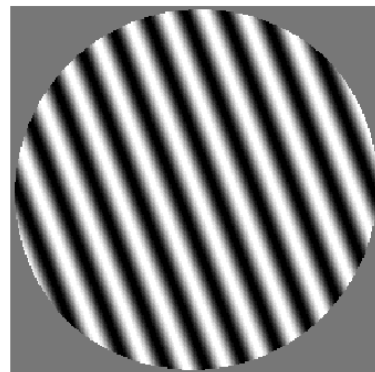
$$\frac{\partial W(x, y)}{\partial x} s = 2D_1 x s \quad \text{and} \quad \frac{\partial W(x, y)}{\partial y} t = 2D_2 y t \quad (5.4)$$

$$D_1 = \frac{d_1}{2R_o^2} \quad \text{and} \quad D_2 = \frac{d_2}{2R_o^2} \quad (5.5)$$

$s$  and  $t$  are the shears in the  $x$  and  $y$  directions respectively.



a



b.

**Figure 5.2 Typical Polarization Shearing Interferogram in the presence of defocus only. (a).  $D_1 = D_2$ ; (b)  $D_1 \neq D_2$ ;**

When the BC is kept equidistant from the focus and  $s = t$  (Fig. 5.2 (a)) the fringes are oriented at  $45^\circ$  to the coordinate axis. Figures 5.2 (b) shows

when  $D_1 \neq D_2$ ; the orientation of the fringes changes and will depend on the ratio  $\frac{D_1 s}{D_2 t}$ .

### 5.2.1 Effect of Shear in the interferogram

A detailed study on the effect of interferogram profiles due to different shear values have been done. The shear are expressed in terms of the aperture. For the normalized aperture of 1 the shear values are generally in the ratio of  $\sim 0.1$ . A few typical cases has been reported in the figure 5.3.

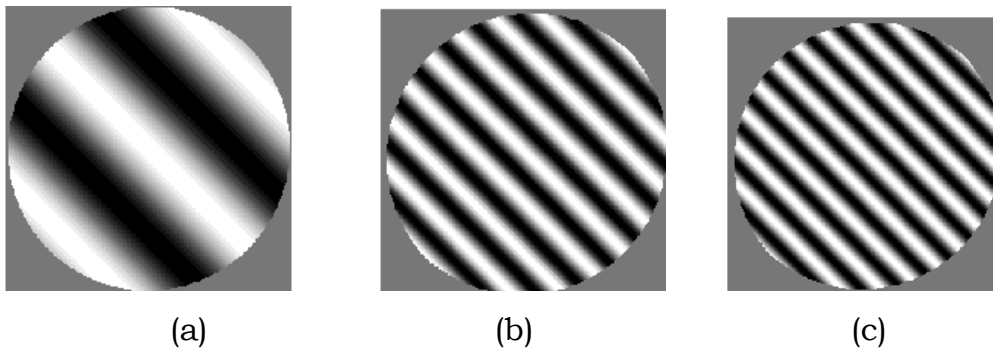


**Figure 5.3 Typical PSI interferogram profiles for various shear values. Equal shear values  $s = t$ ; and equal defocus values  $D_1 = D_2$ ; have been assumed in this case. The normalized shear values are (a)  $s = 0.025$ ; (b)  $s = 0.5$ ; (c)  $s = 0.075$ .**

For the maximum sensitivity an optimum shear value and the defocus values have to be chosen. When the shear values are too large, the fringes become too crowded and difficult to detect. It is better to choose the shear values with reference to the dynamic range of the detector being used in the optical system.

### 5.3 Effect of Third order aberrations in fringe profiles

In order to study the effect of primary aberrations namely, spherical aberration, coma, astigmatism and the x and y tilt in an optical system, interferometric fringe profiles were simulated using the third order equations.

#### 5.3.1 Spherical aberration and Defocus

In the presence of spherical aberration the wavefront error takes the form as

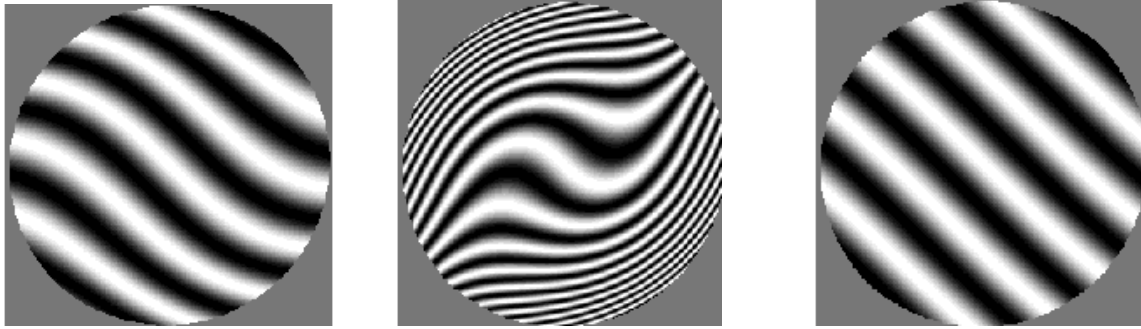
$$\frac{\partial W(x, y)}{\partial x} s = 4Axs(x^2 + y^2) + 2D_1xs \quad (5.6)$$

$$\frac{\partial W(x, y)}{\partial y} t = 4Ayt(x^2 + y^2) + 2D_2yt \quad (5.7)$$

and the intensity at the detector plane is

$$I = K_o + K_1 \cos \left( \frac{2\pi}{\lambda} 4Axs(x^2 + y^2) + 2D_1xs + 4Ayt(x^2 + y^2) + 2D_2yt \right) \quad (5.8)$$

These expressions are very similar to the one described by Malacara (Malacara, 1992), except that these expressions are derived for two dimensional case. For spherical aberration, the fringe shape takes an S shape and the curvature depends on the amount of spherical aberrations present in the system. These expressions hold true in the case of single BC case wherein the shear in either of the directions is made zero. When the magnitudes of the aberrations are very large, the fringes become crowded and the S shape fringes (Fig.5.4) are distorted and reduce the sensitivity of the measurement. At the same time when the aberrations are very small say about  $\lambda/10$  the profiles tend towards straight line.



(a)

(b)

(c)

**Figure 5.4 Typical PSI interferometric fringe profiles for spherical aberration and defocus. Different values of spherical aberrations are chosen. (a)  $A = 1 \lambda$ ; (b)  $A = 10 \lambda$ ; (c)  $A = \lambda/10$**

### 5.3.2 Primary Coma and defocus

In the presence of primary coma alone the wavefront error takes the form as

$$\frac{\partial W(x, y)}{\partial x} s = 2Bxys + 2D_1xs \quad (5.9)$$

$$\frac{\partial W(x, y)}{\partial y} t = B(x^2 + 3y^2)t + 2D_2yt \quad (5.10)$$

and the intensity at the detector plane is

$$I = K_o + K_1 \cos \left( \frac{2\pi}{\lambda} 2Bxys + 2D_1xs + B(x^2 + 3y^2)t + 2D_2yt \right) \quad (5.11)$$

and shown in Figure 5.5.

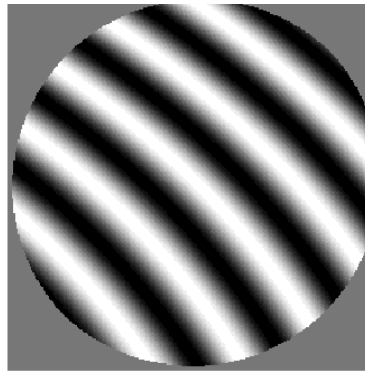


**Figure 5.5 Typical PSI interferogram for coma and defocus combined.**

### 5.3.3 Primary Astigmatism and defocus

In the presence of primary coma alone the wavefront error takes the form as

$$\frac{\partial W(x, y)}{\partial x} s = 2C_{xs} + 2D_{1,xs} \quad (5.12)$$

$$\frac{\partial W(x, y)}{\partial y} t = 2D_{2,yt} - 2C_{yt} \quad (5.13)$$

and the intensity at the detector plane is

$$I = K_o + K_1 \cos \left( \frac{2\pi}{\lambda} 2C_{xs} + 2D_{1,xs} + 2D_{2,yt} - 2C_{yt} \right) \quad (5.14)$$

Figure 5.6 shows the effect of astigmatism and defocus. Note that the fringes broadening at one end and narrowing at the other end.

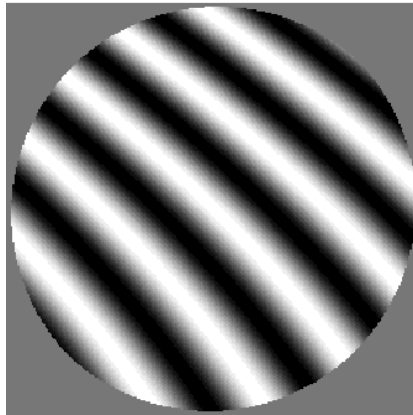


**Figure 5.6 Typical PSI interferogram for Primary Astigmatism and Defocus.**

### 5.3.4 Tilt in X and Tilt in Y

Tilt in X and Y directions results in lateral shift of the fringes in the direction of the resultant shear. When the shear values are chosen to be equal, the lateral shift will be 45 degrees to the direction of the fringes.

### 5.3.5 All Primary Aberrations

When the wavefront error is assumed to have all the primary aberrations (Fig.5.7) then the intensity at the detector plane takes the form as

$$I = K_o + K_1 \cos \left( \begin{array}{l} \frac{2\pi}{\lambda} 4Ax(x^2 + y^2) + 2Bxy + 2Cxs + 2D_1x + E \quad s + \\ \frac{2\pi}{\lambda} 4Ay(x^2 + y^2) + B(x^2 + 3y^2) - 2Cy + 2D_2y + F \quad t \end{array} \right) \quad (5.15)$$

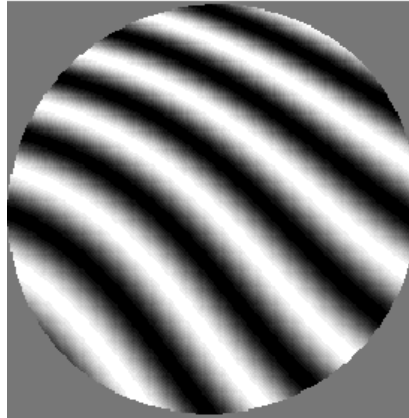


**Fig.5.7 Typical PSI interferogram having primary aberrations.**

## 5.4 Interferogram Simulations using Zernike Polynomial

The use of Zernike polynomials for describing the aberrations introduced by the atmospheric turbulence is well known. The PSI wavefront sensor measures the wavefront slope. The representation of a wavefront using Zernike polynomial has been detailed in chapter 2. Noll (1976) has introduced the integral representation and the derivatives of the Zernike polynomial. The derivatives of the Zernike Polynomials can be written as a linear combination of Zernike polynomial. Hence, the slope information from the wavefront sensor can be conveniently expressed as a function of the Zernike polynomials. Detailed theory of the Zernike polynomials has been reported in chapter 2 and the results are only used in this section. The basic interferometric equation is given by eqn.5.3.

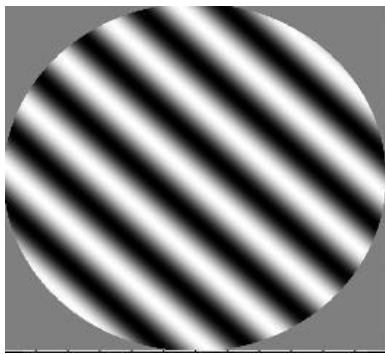
And the gradient of the Zernike polynomial is represented by

$$\nabla Z_j = \sum_j \gamma_{jj'} Z_{j'} \quad (5.16)$$

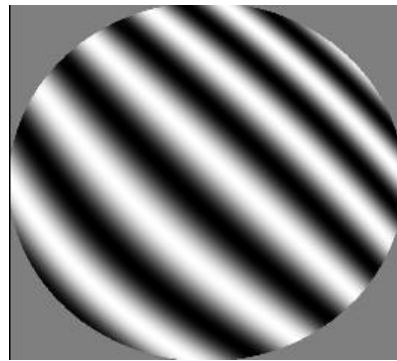
And the wavefront slope is explicitly written as

$$\Delta W(x, y) = \sum_{j=1}^n a_j \left( s \sum_j \gamma_{xjj'} Z_{j'} + t \sum_j \gamma_{yjj'} Z_{j'} \right) \quad (5.17)$$

where  $\gamma_{jj'}$  is called Zernike Derivative matrix. It is presented in Table 5.1. Upon proceeding with Zernike coefficients, the interferograms are simulated (Fig.5.8) for different values of the Zernike coefficients representing different aberrations.



(a)



(b)

**Fig.5.8 Simulated PSI interferograms using the Zernike coefficients (a) only defocus term and all other coefficients is zero. (b) inclusive of all Zernike coefficients.**

## 5.5 Effect of atmospheric turbulence, noise and ripples in the PSI record

An important characteristic of the wavefront sensor is the output interferogram visibility. It is defined as

$$V = \frac{(I_{\max} - I_{\min})}{(I_{\max} + I_{\min})} \quad (5.18)$$

Fringe visibility is a quantitative measure of the contrast of the fringe pattern. In adaptive optics the phase aberration amplitude is continuously changing. This leads to continuous variation in the fringe visibility and contrast. In the absence of the atmospheric turbulence, as seen from the simulations of the interferograms, the visibility is limited only by the noise level and the polarizer and the analyzer imperfections (Pandya and Saxena, 1978). Rigorous numerical simulations of the atmospheric turbulence (Tubbs, 2004, 2005) and the effect of wavefront corrugations on fringe motion has been extensively studied. Another important characteristic of the wavefront sensor is the sensor's nonlinearity; that is the nonlinearity of the phase - intensity transformation. This nonlinearity is characterized by the correlation between the phase  $\phi(r)$  and the output intensity  $I(r)$ . In the presence of atmospheric turbulence induced phase distortions, the wavefront tilts cause the displacement of the fringes. When the displacements are large enough, the fringes become crowded making the detection more cumbersome.

Rigorous simulations of the atmospheric turbulence, is not the scope of the present work but an effort has been made to understand the behavior of the PSI interferometric fringes in the presence of atmosphere like noise. Simulations were performed having a uniform intensity and introducing random phase variations inside a circular aperture of

diameter  $D$ . The input phase variations were characterized by the variance of the Zernike coefficients (Noll, 1976).

The mean square residual error is defined as

$$\Delta = \langle \phi^2 \rangle - \sum_{j=1}^J \langle |a_j|^2 \rangle \quad (5.19)$$

where  $\langle \phi^2 \rangle$  is the phase variance and  $a_j$  are the Zernike coefficients.

The approximated equation is given by

$$\Delta_j \approx 0.2944 J^{-\sqrt{3}/2} D/r_o^{5/3} \quad (\text{rad}^2) \quad (5.20)$$

Based on the above equations, and from the mean residual errors calculated by Noll given in table 2.2, some sample simulations were carried out for few values of  $D/r_o$  are shown in the figure 5.9 a-d.

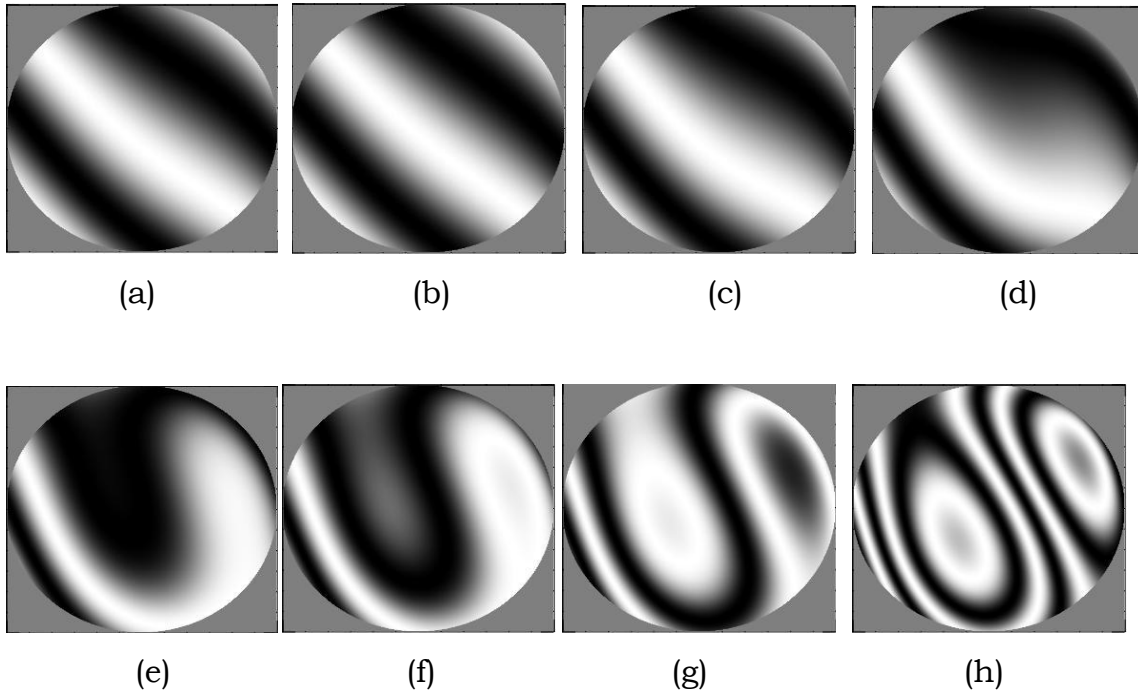


**Fig.5.9 Simulated PSI interferograms corresponding to different  $r_o$  values and  $D=1$ . (a)  $r_o = 1$ , (b)  $r_o = 0.75$ , (c)  $r_o = 0.5$ , (d)  $r_o = 0.25$ , (e)  $r_o = 0.125$ , (f)  $r_o = 0.1$ , (g)  $r_o = 0.05$ , (h)  $r_o = 0.025$**

The simulated results show the presence of atmospheric induced distortions by the change in the value of  $r_o$ . The visibility and contrast in the interferograms do not change considerably whereas it causes the displacement of the fringes quite appreciably. The orientation of these fringes also changes. The value of  $r_o$ , also keep changing with time. The effect of other sources of noise is not taken into consideration for simulating the above interferograms. The results were computed with one fringe in the field of view.

### **5.5.1 Effect of noise**

The signal to noise ratio of an interferogram is a quality estimation factor. It is a measure of how strong the signal is with respect to the external noise present at the time of observation. The CCD detectors produce noise due to the stray photons apart from the original signal. In one dimensional, the profile of the noise free interferogram (Fig.5.10.a.) provides a pure sinusoidal pattern (Fig.10.b.) and the amplitude of this sinusoidal wave can be regarded as the strength of the signal. In the presence of white noise (Fig.5.10.d.), in one dimensional profile, the sinusoidal pattern is enveloped with high frequency components (Fig.5.10.e). The noise is removed in the Fourier domain by subtracting these frequencies. Observation of the Fourier transforms (Fig.10.c. & 10.f.) of both the interferograms shows the Gaussian noise in the fringe pattern translates into white noise in the Fourier domain. The noise is the standard deviation of the resultant image obtained by subtracting the sinusoidal component from the fringe pattern.

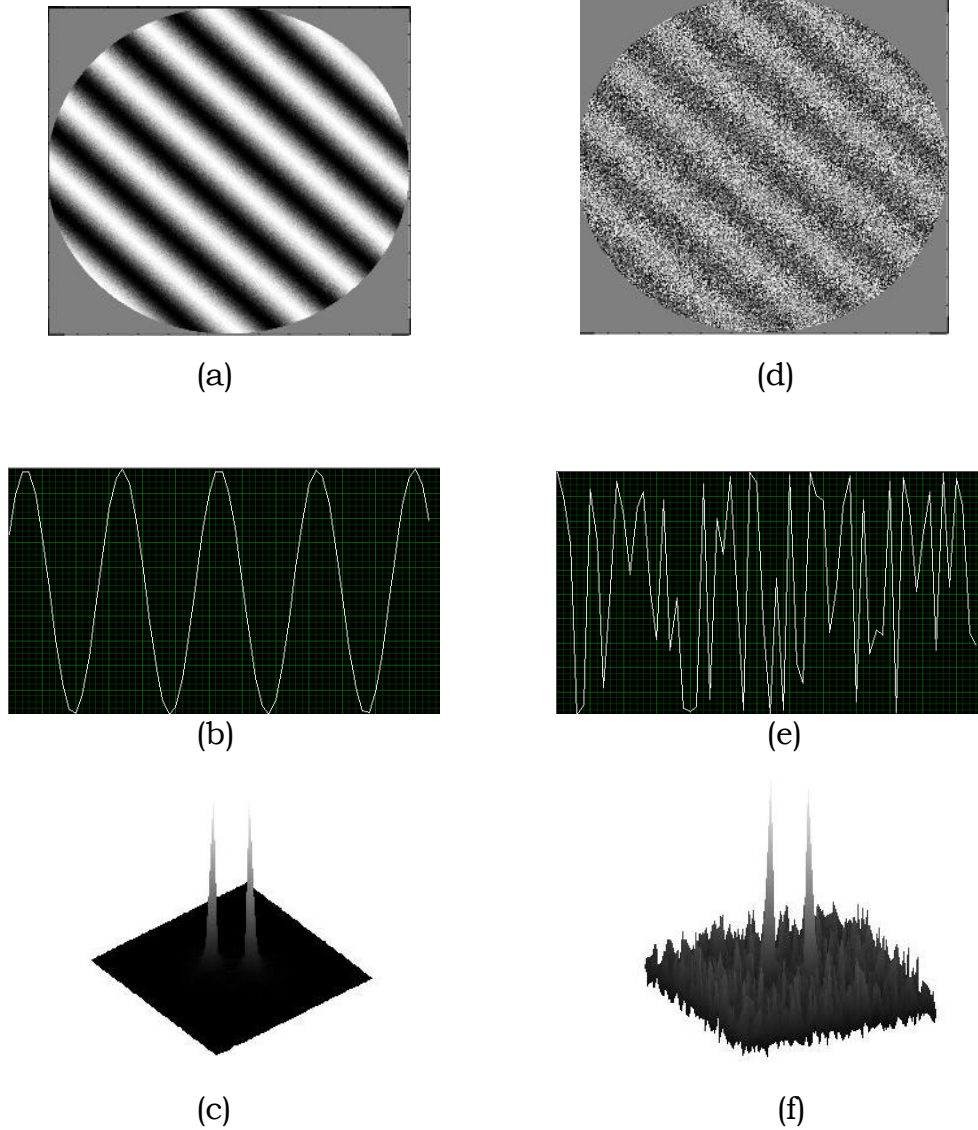


**Fig.5.10 (a) A Noise-free fringe pattern; (b) a one dimensional profile; (c) Fourier transform of (a); (d) A noisy fringe pattern; (e) one dimensional profile; (f) Fourier transform of (d).**

The presence of random noise, alters the visibility and the contrast of the fringes drastically. For visualization and for illustration purposes, a random noise was additionally introduced in the same simulation. The effect of varying noise level on PSI are shown in Fig.5.11.

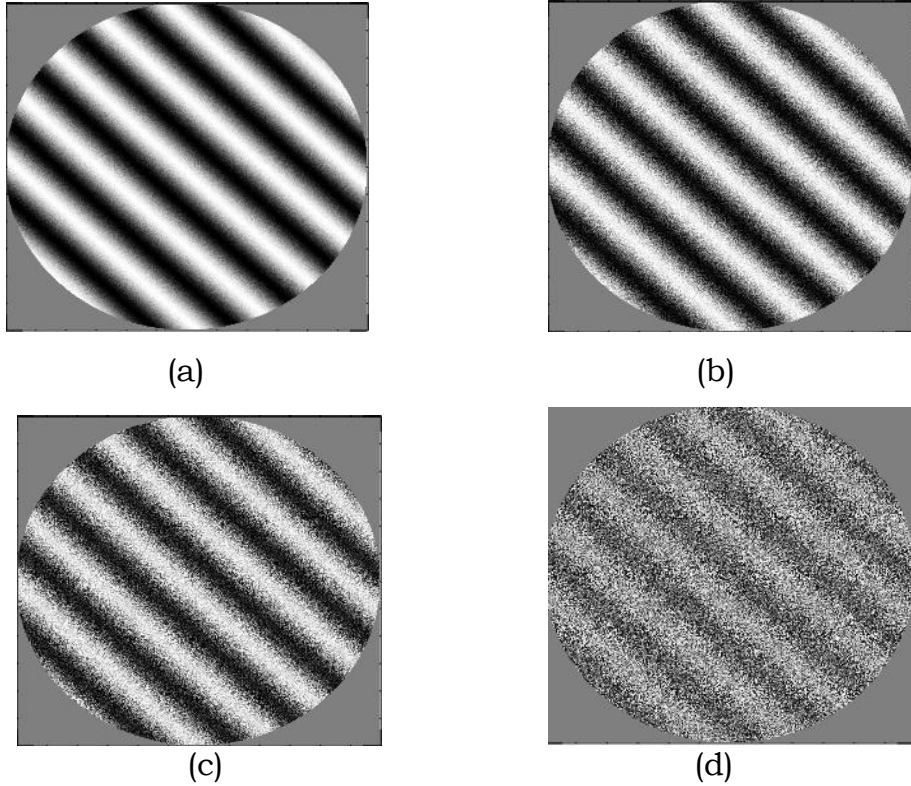


**Fig.5.11 The effect of noise on PSI interferograms. The effect of noise introduced in the interferometric equation as an added random term in the phase. (a)  $\delta < 0.05$  (b)  $\delta < 0.15$  (c)  $\delta < 0.25$  (d)  $\delta < 0.5$**

These visualizations show that the performance of the PSI wavefront sensor can only be limited by the presence of noise during the observation. The noise is represented as a random number obtained from a normal distribution. The value of noise introduced as a random number into the interferometric equation

$$I = K_o + K_1 \cos(\varphi + \delta) \quad (5.21)$$

## 5.5.2 Ripples

The next source of error comes from the inherent fabrication errors. These errors are from low frequency to high frequency components. The following Figures in 5.12 show the presence of ripples produced during the fabrication of the optics, which reduces the fringe visibility and introduces high frequency components into the system.

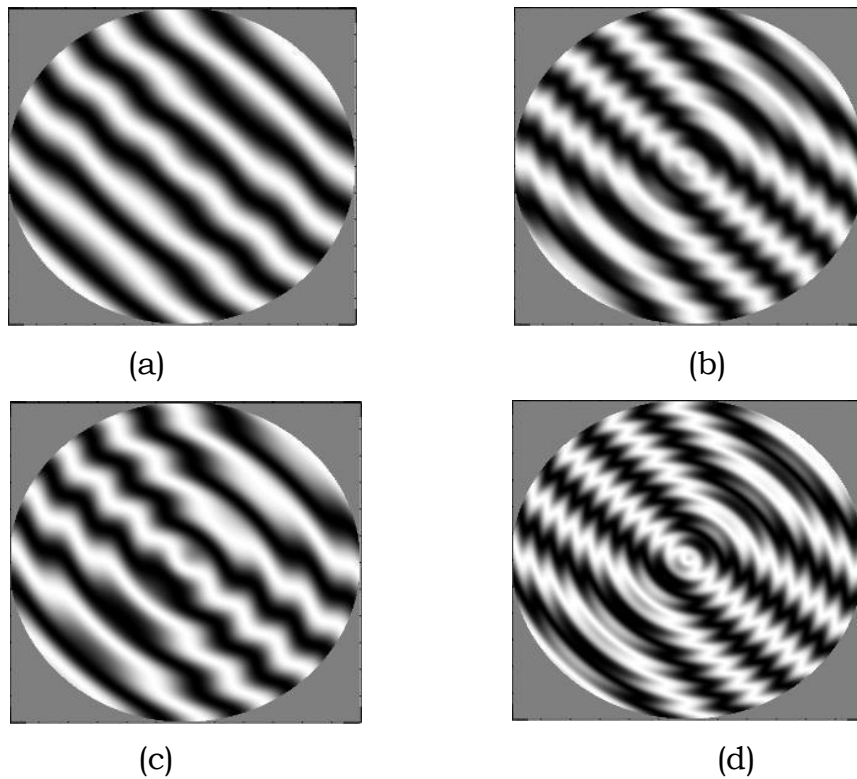


**Fig.5.12 Simulated PSI interferograms for ripples. The ripples are created as cosine function introduced into the phase factor of the interferometric equation.(a)  $\delta < 0.03; \alpha = 30.$ , (b)  $\delta < 0.03; \alpha = 90.$ , (c)  $\delta < 0.05; \alpha = 45$  (d)  $\delta < 0.5; \alpha = 120.$ ,**

The ripples are the static errors which do not change in time. These errors can be evaluated and subtracted from the interferogram. Different amount of ripples are demonstrated in the simulated interferograms.

Since these ripples and noise are of high frequency compared to the modulation frequency, it is convenient to remove these using Fourier transform technique.

The theoretical simulations help to understand and visualize the polarization shearing interferometric fringes behavior in the presence of various aberrations in an optical system. It also demonstrated the capability of the interferometer in measuring the phase errors introduced by the atmospheric turbulence with the use of Zernike polynomials. The method proves to be a promising option for the measurement of wavefront errors in the presence of atmospheric turbulence for an adaptive optics system.

# Chapter 6

## Reconstruction of the wavefront from Polarization Shearing Interferogram

Typical simulations of the Polarization Shearing Interferometer (PSI) records were discussed in the last chapter. The two dimensional wavefront has to be reconstructed from the shearing interferograms. Several methods (Harbers et al. 1996; Humphries et al. 1997; Okuda et al. 2000; Peiyong Liang et al. 2006;) are suggested to perform this task. This chapter is devoted to the analysis of a single PSI interferogram to estimate errors for appropriate correction for an AO system. Fourier analysis approach has been adopted for determination of local phase of the proposed PSI interferogram. The Fourier transform method is resistant to noise and is highly efficient and very simple to apply. The phase thus recovered is measured with an integral multiple of  $2\pi$  uncertainties. The process of removing these uncertainties is called *phase unwrapping*. After phase has been completely unwrapped, the data contains the derivatives of the original phase of the wavefront. The derivative of the wavefront phase can conveniently be written in terms of

Zernike polynomials, to estimate the wavefront errors. The Zernike coefficients provide the complete information of the wavefront.

Generally, interferogram analysis has been divided into two major categories by their use of either a single or multiple interferogram analysis. Several methods are suggested in the literature in both categories (Creath 1981; Takeda et al. 1982; Greivenkamp and Bruning 1992). The multiple interferogram techniques combine several separate measurements. Generally, in the case of lateral shearing interferogram, measurements taken from two orthogonal directions are combined to determine the phase of the interferogram. There is no one method which can be universally adopted for interferogram analysis. In adaptive optics situations, where the processing of the interferogram has to be carried out in minimum possible time, analysis of the single interferogram is a preferred choice.

## **6.1 Single Interferogram Analysis of Polarization Shearing Interferogram**

The Fourier Transform method is most commonly used for solving the case of single interferogram analysis. A complete study of the existing method was undertaken in order to choose the most appropriate one for the Polarization Shearing Interferogram analysis. The basic assumption is that the intensity variations are caused by the phase variations rather than the amplitude fluctuations.

### **6.1.1 Fourier Transform Analysis of the PSI Interferogram**

Since early 1980s, Fourier transform techniques for interferogram fringe pattern analysis and wavefront recovery have gained widespread acceptance as the leading methods for single interferogram analysis.

(Takeda et al. 1982; Nugent 1985; Bone et al. 1986; and Roddier C & Roddier F 1987). Fourier transform methods offer greater flexibility in the separation of the low frequency and high frequency components in the spatial frequency spectrum.

The irradiance distribution in an interferogram can be described as

$$I(x, y) = A(x, y) + B(x, y) \cos 2\pi f_o \cdot r + \phi(x, y) \quad (6.1)$$

where  $A(x, y)$ , and  $B(x, y)$ , are the unwanted irradiance variations arising due to the imperfections in the optical system, and  $\phi(x, y)$  represents the phase of the interferogram and  $f_o$  is the spatial carrier frequency. A typical one dimensional irradiance distribution of an interferogram and its Fourier transform is shown in Figure 6.1

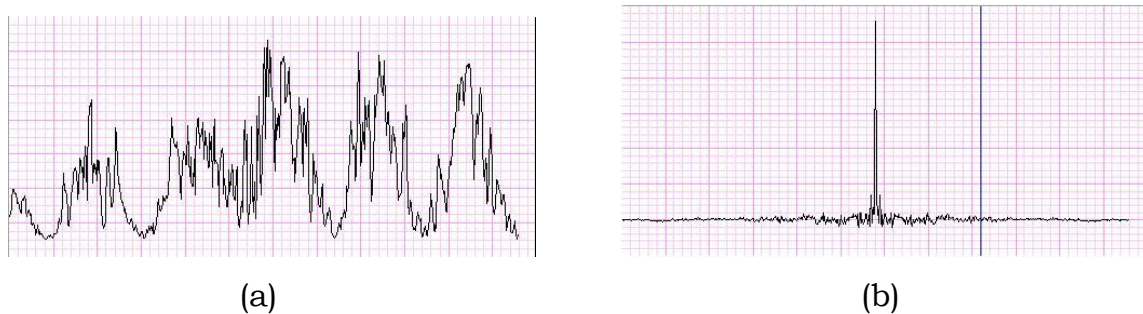


**Fig.6.1 (a) A typical one dimensional noisy interferogram profile and (b) Fourier Transform of the interferogram**

In the present case of Polarization Shearing Interferometry, the phase  $\phi(x, y)$  is related to the slope  $\Delta W(x, y)$  of the actual wavefront. In general, for the analysis of single interferogram, a spatial carrier frequency is introduced in the phase term to facilitate analysis. In this case, an additional carrier frequency is not required as it is contained in the  $\phi(x, y)$ . The carrier frequency comes handy by means of the defocus term in the Zernike polynomial and it corresponds to the distances of the BC on either side of the focus (eqn. 5.5) and it is explicitly written in the above equation.

To facilitate the Fourier representation of the interferogram, the intensity function is re-written in the complex form as

$$I(x, y) = A(x, y) + \frac{1}{2}B(x, y) \begin{bmatrix} \cos 2\pi f_o.r + \phi(x, y) + i \sin 2\pi f_o.r + \phi(x, y) \\ + \cos 2\pi f_o.r + \phi(x, y) - i \sin 2\pi f_o.r + \phi(x, y) \end{bmatrix} \quad (6.2)$$

In a more convenient form in one dimensional it can be re-written as

$$I(x, y) = A(x, y) + C(x, y)\exp(i2\pi f_o x) + C^*(x, y)\exp(-i2\pi f_o x) \quad (6.3)$$

where

$$C(x, y) = \frac{1}{2}B(x, y)\exp(i\phi(x, y)) \quad (6.4)$$

and \* denotes complex conjugate.

Performing Fourier Transform operation in one dimensional using FFT algorithm results in

$$\tilde{I}(f, y) = \tilde{A}(f, y) + \tilde{C}(f - f_o, y) + \tilde{C}^*(f + f_o, y) \quad (6.5)$$

where  $\tilde{I}$ ,  $\tilde{A}$ ,  $\tilde{C}$  represents the Fourier transforms of  $I$ ,  $A$ , &  $C$  respectively. Since,  $A(f)$  and  $C(f)$  are low spatial frequency components, they are strongly peaks at zero frequency. Depending on the phase aberrations present in the system,  $\tilde{C}$  and  $\tilde{C}^*$  typically consist of a narrow peak near zero frequency. The presence of the carrier frequency shifts  $\tilde{C}$  and  $\tilde{C}^*$  by  $f_o$  and  $-f_o$ . Choosing either of a spectra say,  $\tilde{C}(f - f_o)$  and translate it by  $\pm f_o$  on the frequency axis toward the origin to obtain  $\tilde{C}(f, y)$ . By doing this process, the fringe modulations are separated out and all the unwanted background noise has been filtered out. Prior knowledge of the spatial frequency, which has been dictated by the defocus term, enables easier identification of the modulation frequency. Again using the FFT algorithm, compute the inverse Fourier transform

$\tilde{C}(f, y)$  with respect to  $f$ , to obtain  $C(x, y)$ . The wavefront slope information is contained in  $C(x, y)$ .

Now the intensity distribution after removing all the unwanted amplitude variations,

$$I(x, y) = C(x, y) = \frac{1}{2} B(x, y) \exp(i\phi(x, y)) \quad (6.6)$$

and  $\phi(x, y)$  is computed as

$$\phi(x, y) = \arctan \left[ \frac{\text{Im } c(x, y)}{\text{Re } c(x, y)} \right] \quad (6.7)$$

The phase thus obtained is indeterminate to a factor of  $2\pi$ .

### 6.1.2 Phase Unwrapping or Determination of Wavefront slope

The phase, as per the above equation, is measured within an integer multiple of  $2\pi$ . Due to the periodic nature of the arctangent, the phase  $\phi(x, y)$  is determined within an arbitrary multiple of  $2\pi$ , in some cases, within a multiple of  $\pi$ . It is imperative to reconstruct the actual wavefront slope from the value of  $\phi(x, y)$  which is discontinuous. Each point in  $\phi(x, y)$  is related to the actual wavefront slope by an arbitrary number of  $2\pi$  steps.  $\phi(x, y)$  is called a modulo  $2\pi$  wavefront slope and is related to the actual wavefront slope by the relation

$$\phi_{\text{actual}}(x, y) = \phi(x, y) \bmod 2\pi \quad (6.8)$$

Several approaches are suggested in the literature (Takeda et al. 1982; Macy 1983; Bone et al. 1986; C. Roddier & F Roddier 1987) to solve this inverse problem. The modulus  $2\pi$  wavefront slope is used to reconstruct the actual wavefront slope such that  $\phi(x, y)$  is a continuous function. The procedure to be followed is explained as follows.

The first step in making this determination is to compute the difference of the phase  $\phi(x, y)$  from the adjacent points.

$$\Delta\phi(x, y) = \phi(x_i, y) - \phi(x_{i-1}, y) \quad (6.9)$$

Since the variation in the wavefront slope is slow compared with the sampling interval, the absolute value of the difference is much less than  $2\pi$  at points where the distribution is continuous. But it becomes almost  $2\pi$  at locations where the  $2\pi$  phase jump occurs. Hence, by setting an appropriate criterion for the absolute value for the difference, say  $0.9 \times 2\pi$ , we can specify all the points at which the  $2\pi$  jump takes place. Repeating this procedure by appropriately adding or subtracting  $2\pi$  at the points of discontinuity the ambiguity is overcome. As a result, a continuous wavefront slope distribution is obtained.

## 6.2 Wavefront determination from wavefront slope data using Zernike polynomial

The aberrated wavefront has to be reconstructed from the wavefront slopes derived from the above method. The wavefront aberrations can be well represented by Zernike polynomials. A brief overview of the Zernike polynomials has been discussed in the chapter 2. The derivatives of the Zernike polynomials can be expressed as a linear combination of Zernike polynomial (Noll, 1976). They are written as

$$\Delta Z_j = \sum_j \gamma_{jj} Z_j \quad (6.10)$$

Alternatively

$$\Delta\phi = \sum_j \left( \sum_j a_j \gamma_{jj} \right) Z_j \quad (6.11)$$

where  $\gamma_{jj}$  are the coefficients of the Zernike expansion of the derivative of the  $j^{\text{th}}$  Zernike. The matrix  $\gamma$  is called Zernike derivative matrix and it is given in Noll, 1976. It is presented here as a Table 4.1. The wavefront slope as derived from this method can be written as in equation 5.2.

$$\Delta W(x, y) = \frac{\partial w}{\partial x} s + \frac{\partial w}{\partial y} t$$

where  $\frac{\partial W}{\partial x}$  &  $\frac{\partial W}{\partial y}$  correspond to the x and y derivatives of the wavefront slope. Therefore

$$\frac{\partial W}{\partial x} = \sum_j \left( \sum_j a_j \gamma_{jj}^x \right) Z_j \quad \text{and} \quad \frac{\partial W}{\partial y} = \sum_j \left( \sum_j a_j \gamma_{jj}^y \right) Z_j \quad (6.12)$$

So that combining (5.2), (6.11) and (6.12),

$$\Delta W(x, y) = s \sum_j \left( \sum_j a_j \gamma_{jj}^x \right) Z_j + t \sum_j \left( \sum_j a_j \gamma_{jj}^y \right) Z_j \quad (6.13)$$

In matrix notation this equation can be written as

$$\mathbf{W} = \mathbf{A} \mathbf{Z}$$

Where  $\mathbf{W}$  contains the values of the wavefront slope,  $\mathbf{A}$  the Zernike coefficients which are to be determined and  $\mathbf{Z}$  is the Zernike polynomial corresponding to the coefficients with a multiplicative factor of shear. The number of measurements is typically more than the number of unknowns, so a least square solution is useful. This over determined system is solved as follows:

$$\begin{aligned} \mathbf{W} \mathbf{Z}^T &= \mathbf{A} \mathbf{Z} \mathbf{Z}^T \\ \mathbf{W} \mathbf{Z}^T (\mathbf{Z} \mathbf{Z}^T)^{-1} &= \mathbf{A} (\mathbf{Z} \mathbf{Z}^T) (\mathbf{Z} \mathbf{Z}^T)^{-1} \\ \mathbf{A} &= \mathbf{W} \mathbf{Z}^T (\mathbf{Z} \mathbf{Z}^T)^{-1} \end{aligned} \quad (6.14)$$

		$m'$	1	1	0	2	2	1	1	3	3	0	2	2	4	4	
		$J'$	1	2	3	4	5	6	7	8	9	10	11	12	13	14	15
$m$	$j$																
0	1																
1	2		2														
1	3																
0	4			$2\sqrt{3}$													
2	5				$\sqrt{6}$												
2	6			$\sqrt{6}$													
1	7						$2\sqrt{3}$										
1	8		$\sqrt{8}$			$2\sqrt{6}$		$2\sqrt{3}$									
3	9						$2\sqrt{3}$										
3	10							$2\sqrt{3}$									
0	11			$2\sqrt{5}$					$2\sqrt{10}$								
2	12			$\sqrt{10}$					$2\sqrt{5}$		$2\sqrt{5}$						
2	13				$\sqrt{10}$			$2\sqrt{5}$		$2\sqrt{5}$							
4	14										$2\sqrt{5}$						
4	15									$2\sqrt{5}$							
1	16		$\sqrt{12}$			6		$3\sqrt{2}$				$2\sqrt{15}$	$\sqrt{30}$				
1	17						$3\sqrt{2}$							$\sqrt{30}$			
3	18							$3\sqrt{2}$					$\sqrt{30}$				
3	19						$3\sqrt{2}$							$\sqrt{30}$		$\sqrt{30}$	
5	20														$\sqrt{30}$		
5	21																$\sqrt{30}$

**Table 6.1 Zernike Polynomial X Derivative  $\gamma_{jj}^x$  matrix elements**

		m'	0	1	1	0	2	2	1	1	3	3	0	2	2	4	4
		J'	1	2	3	4	5	6	7	8	9	10	11	12	13	14	15
m	j																
0	1																
1	2																
1	3		2														
0	4				2√3												
2	5			√6													
2	6				-√6												
1	7		√8			2√6		-2√3									
1	8						2√3										
3	9							2√3									
3	10							-2√3									
0	11				2√5				2√10								
2	12				-√10				-2√5		2√5						
2	13			√10						2√5		-2√5					
4	14										-2√5						
4	15											2√5					
1	16						3√2									√30	
1	17		√12			6		-3√2					2√15	-√30			
3	18						-3√2								-√30		√30
3	19							3√2						√30		-√30	
5	20																-√30
5	21															√30	

**Table 6.2 Zernike Polynomial Y derivative  $\gamma_{ij}^y$  matrix elements**

**A** provides the Zernike coefficients. Note that the piston term is not calculated in the above method as it is zero and it moreover, it is not necessary. Using the Zernike coefficients, the aberrated wavefront is reconstructed as

$$W(x, y) = \sum_{j=2}^N a_j Z_j \quad (6.15)$$

where  $a_j$ s are the Zernike expansion coefficients. So far the considerations have involved, derivations based on the theory for  $\Delta W_x$  and  $\Delta W_y$ , with the resulting polynomial expressions formulated always in terms of a circle of unit radius. Measurement of the shearing interferograms, in the pupil overlaps region and the fitting of the circle polynomials to these have been carried out. For small shear, the pupil overlap region is close in position and size to that of the original pupil. For larger shear values ( $S > 0.1$ ) corrections are required for the changed geometry in which the fringes are produced and measured. These corrections are described by Atad et al.(1990). For the present considerations with shear values  $S$  and  $T < 0.1$ , these corrections are negligible.

### **6.3 Sensitivity**

The sensitivity of the wavefront sensors is defined as the ability to measure the wavefront errors in the turbulent atmosphere. In the case of the Polarization Shearing Interferometer the sensitivity of the device lies in the choice of the Babinet Compensators (BC). The wedge angle of the BC and the f-ratio of the optical system being used, determine the amount of shear produced by the shearing device in the optical beam. As suggested (Welsh et al., 1995), the optimum value of the shear for a Gaussian source distribution is

$$s_{opt} = 1/\sqrt{\pi}\beta \quad (6.16)$$

where  $\beta$  is the ratio of the angular size of the source to the seeing limited angular resolution. It is also suggested that the  $s < 0.25$  is resistant to the degradation caused due to the atmospheric turbulence. In the case of PSI a shear value of 0.1 to 0.25 is comfortably achieved by proper choice of wedge angle to suit the optical system. The appropriate value of the shear is chosen based on the pupil aperture, fringe parameters, detector resolution and the dynamic range of the detector. The measuring sensitivity of the Polarization Shearing Interferometer (PSI) can be evaluated by the minimum detectable wavefront aberration (Xu, et al, 2006). Hence, the real sensitivity lies on the ability of the BC to detect the smallest phase change. It has been shown (Saxena, 1979) that the minimum detectable phase change is  $2\pi$  milli radians. The sensitivity of the method depends on the position of the BC near the focus. When the two crossed BC are placed very close to the focus of the optical system, there appears only a single fringe in the field of view. A small phase error alters the intensity of point in the observation image plane. Hence, maximum sensitivity can be obtained in this position and a small error in the position or location will not alter the sensitivity drastically. Secondly, the sensitivity of the method depends on the spatial resolution of the detector pixels. With the advent of small pixel size detector the sensitivity is bound to improve for better. Finally, the sensitivity of any shearing interferometer depends on the shear value.

# Chapter 7

## Details of the Laboratory Experimental Work and Results

In order to validate the performance of the proposed wavefront sensor using Polarization Shearing Interferometer, laboratory experiments were carried out in our laboratory. An optical design has been worked out for carrying out the experiments with Polarization Shearing Interferometer (PSI-WS) and Shack Hartmann Wavefront Sensor (SH-WS). The optical system has been designed in such a way where the two measurements can be carried out in the same optical bench. The details of the optical layout for both the measurements and the experimental procedures followed are presented. A static phase plate, to represent atmospheric turbulence, was used to estimate the wavefront errors by PSI-WS and SH-WS.

Turbulence plates should produce aberrated waves that have temporal and spatial characteristics. Different methods exist to obtain a phase screen or plate either by using a CD ROM plastic support (Pinna et al, 2004) or by etching on glass plates (Stefan, 2006) or by rotating glass plates to create atmospheric turbulence

(Rhoadarmer and Angel 2001). However, for testing purposes, a static phase plate consisting of two plane thin glass plates with a thin film of air is considered. Though, this plate may not exactly quantify or simulate atmospheric turbulence, it was chosen to introduce random errors into the system and is adequate to test the principles of wavefront sensing described in this thesis. This phase plate was initially calibrated using the Zygo interferometer. The measurements were taken in quick succession on the same optical bench, with the identical environmental conditions. The results of the PSI-WS are compared with the results of SH-WS. The wavefront profile, Zernike coefficients, peak to valley (PV) and the rms deviation of the wavefront deviation are estimated using the above methods and compared.

## **7.1 Laboratory Experiment with Shack Hartmann Wavefront Sensor**

### **7.1.1 Optical Design and Layout**

The optical design of the experimental set up was worked out. The main parameters in designing the optical system are the size of the Shack Hartmann lenslet array and the detector array size. The optical design included a beam reducer system, which consists of a combination of lenses to re-collimate the beam to a smaller diameter. The system consists of second collimator and using the optical design the conjugate pupil plane was located. The entire optics procured from reputed

companies (with tested standardization norms), were rigidly housed in a single metal tube, to avoid any moving parts of the system.

The schematic of the optical layout for the wavefront sensing experiment is given in Fig.7.1. It consists of collimators, re-imaging optics, wavefront sensor and detector, coupled to the recording system.

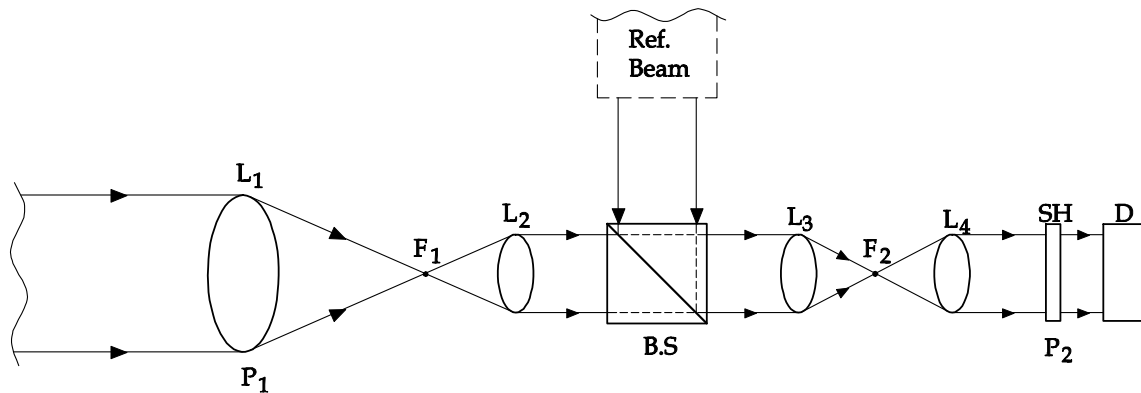


**Fig.7.1 Schematic diagram of the optical layout for SH wavefront sensor**

The collimated beam of 100 mm aperture is simulated using Zygo interferometer operating at the wavelength 632 nm. A 100 mm aperture  $f/3$  lens represents telescope optics and the pupil plane, which focuses the collimated beam to focus at  $F_1$ . The lens combination  $L_2$ ,  $L_3$  and  $L_4$  re-images the pupil plane  $P_1$  at  $P_2$  with reduced beam diameter equivalent to the size of the detector array size. The Shack Hartmann lenslet array is placed at the conjugate pupil plane  $P_2$ . The focus of the lenslet array lies at the detector plane. A reference beam was generated using a 25 mm collimator and passes through the beam splitter. The Shack Hartmann lenslet array was procured from AOA and the specifications are given below.

Details	Specification
Lenslet Array Size	20 x 20
Diameter of the lenslet	500 $\mu$
Focal length of the lenslet	30 mm

DALSA CA-D7 1024 T area CCD detector was used for recording of the SH images and for the interferometric records. The important specifications of the CCD camera are:

Details	Specifications
Camera Resolution	1056 x 1024
Sensor Size	12.288 mm x 12.288 mm
Pixel Size	12 $\mu$ m x 12 $\mu$ m
Frame rate	8 Hz
Dynamic Range	10 bit

### **7.1.2 Shack Hartmann Experiment:**

In the laboratory setup a collimated beam is derived from a Zygo interferometer as described in the last section. The actual experiment was performed in an anti vibration isolation table and the components mounted as per the optical layout of Fig.7.1. A neutral density filter was introduced in the optical beam to control the intensity of the light and to have better contrast. A special adapter was fabricated to house the Shack Hartmann lenslet array and the adapter was fitted on to the

detector housing such that the detector plane lies at the focal plane of the lenslet array. The actual photograph of the set up is shown in the Fig.7.2. The Shack Hartmann images were acquired using the DALSA CCD camera.

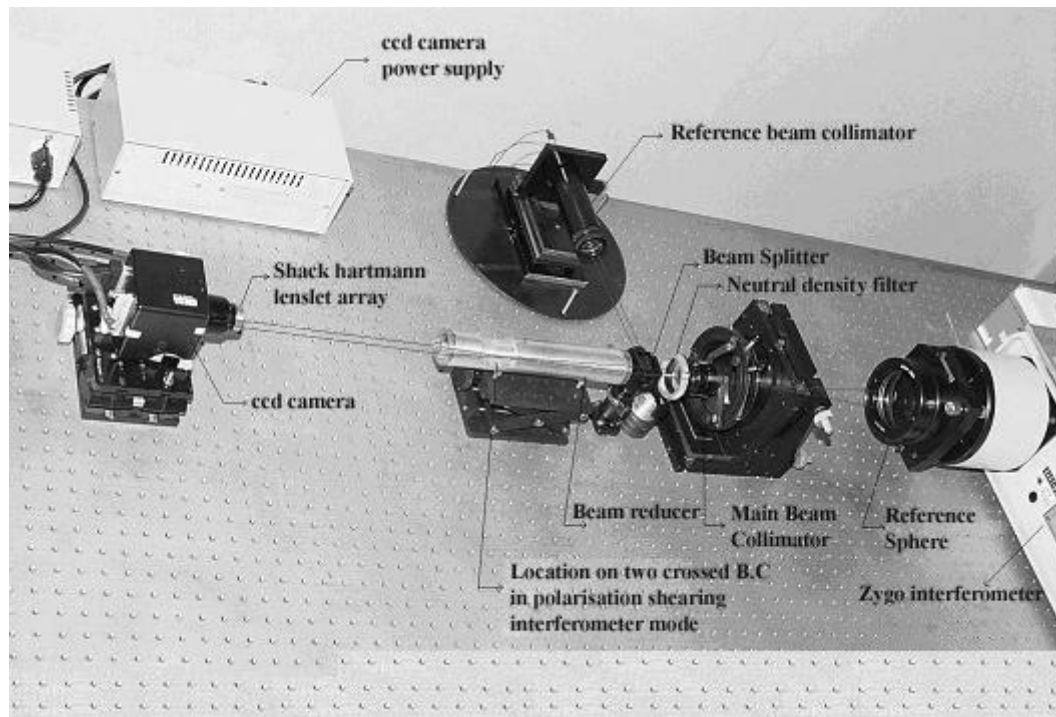


**Fig. 7.2 Photograph of the Actual set up**

First, using the reference beam the optics was aligned such that the images were centered to the detector. The reference images were recorded using the laser source. The reference image is shown in Fig. 7.3.

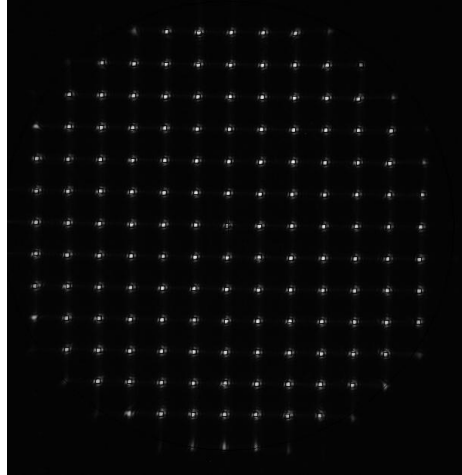


**Figure 7.3 CCD image of the Shack Hartmann spots of the reference beam.**

After recording the reference image, the turbulator or phase plate was introduced at the pupil plane  $P_1$  as discussed before and without changing any parameter in the optical set up, the shack Hartmann image was again recorded. The aberrated Shack Hartmann image recorded as above is shown in Fig. 7.4.

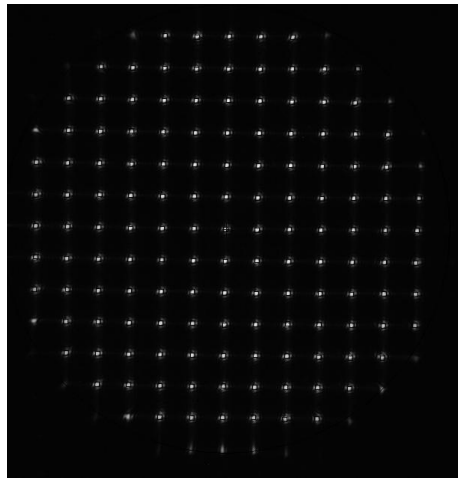


**Fig.7.4 The CCD images of the Shack Hartmann spots of the aberrated beam.**

The exact characteristics of the turbulence plate is not of prime importance as we are not duplicating exact atmospheric turbulence in the plate.

### 7.1.3 Data Analysis and Results:

The software for the analysis of the Shack Hartmann images was written in the LabView platform. The standard data reduction procedure expressing the slope as a function of Zernike polynomial (Primot et al, 1990) has been adopted. The complete analysis was carried out using the software written by ourselves for this purpose. The basic steps used in the analysis are as follows.

- a. Fixing of the origin for both the records
- b. Keeping the same origin determines the centroids of the spots in both the images.
- c. Calculation of the slope of the wavefront at every co-ordinate
- d. Fitting of the derivative of the Zernike polynomials to the slope
- e. Estimation of the Zernike coefficients by least square fit
- f. Wavefront reconstruction
- g. Plotting of the wavefront surface
- h. Computation of Variance, Peak to Valley and rms deviation of the wavefront

The Figures 7.5 (a) and 7.5 (b) show the method of identifying the centroids for the Shack Hartmann spots. To reduce the computation time a small area around each spot was chosen and the co-ordinate of maximum density was computed using the algorithm discussed in chapter 6.

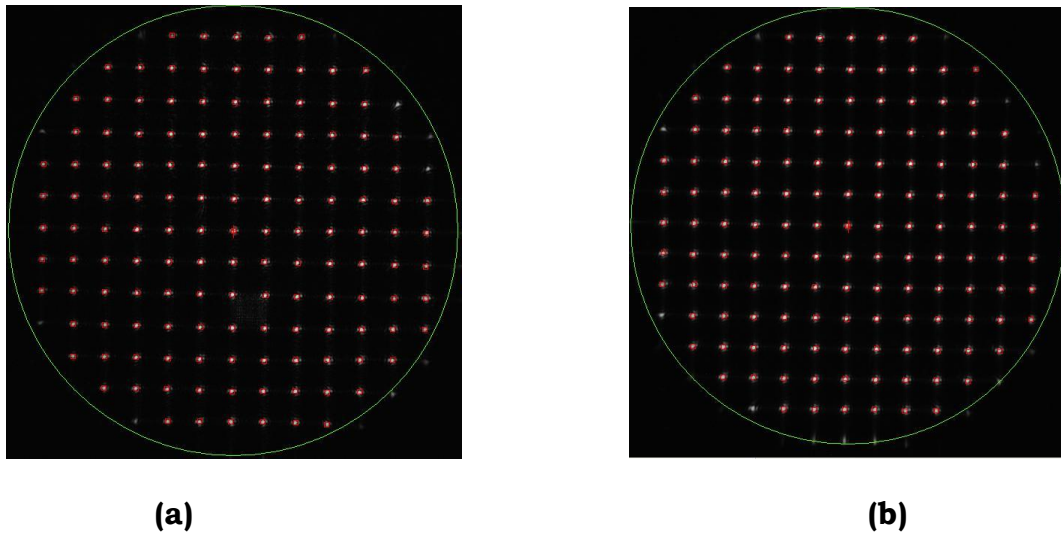


**Fig.7.5 A small area around each spot has been marked for computing the centroid of the spots (a) reference spots (b) Spots due to aberrated beam.**

The centroids for each record were calculated and the difference computed. The difference gives the value of the slope of the wavefront at that particular co-ordinate. The slope values are fitted to the derivatives of the Zernike polynomials as discussed in the theory. In this case, 21 Zernike co-efficients have been taken for wavefront determination. Using the least square method of fitting the Zernike co-efficients were computed. The wavefront surface was reconstructed by using the Zernike coefficients excluding the tip-tilt terms. The wavefront surface determined is shown in Fig. 7.6

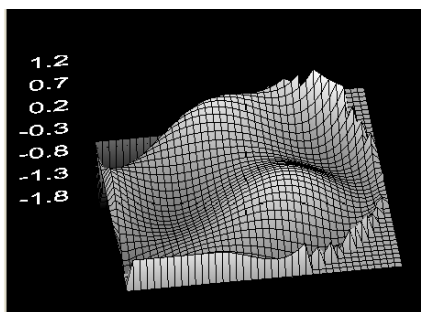


**Fig.7.6 The 2D representation of the wavefront error computed from the Shack Hartmann method.**

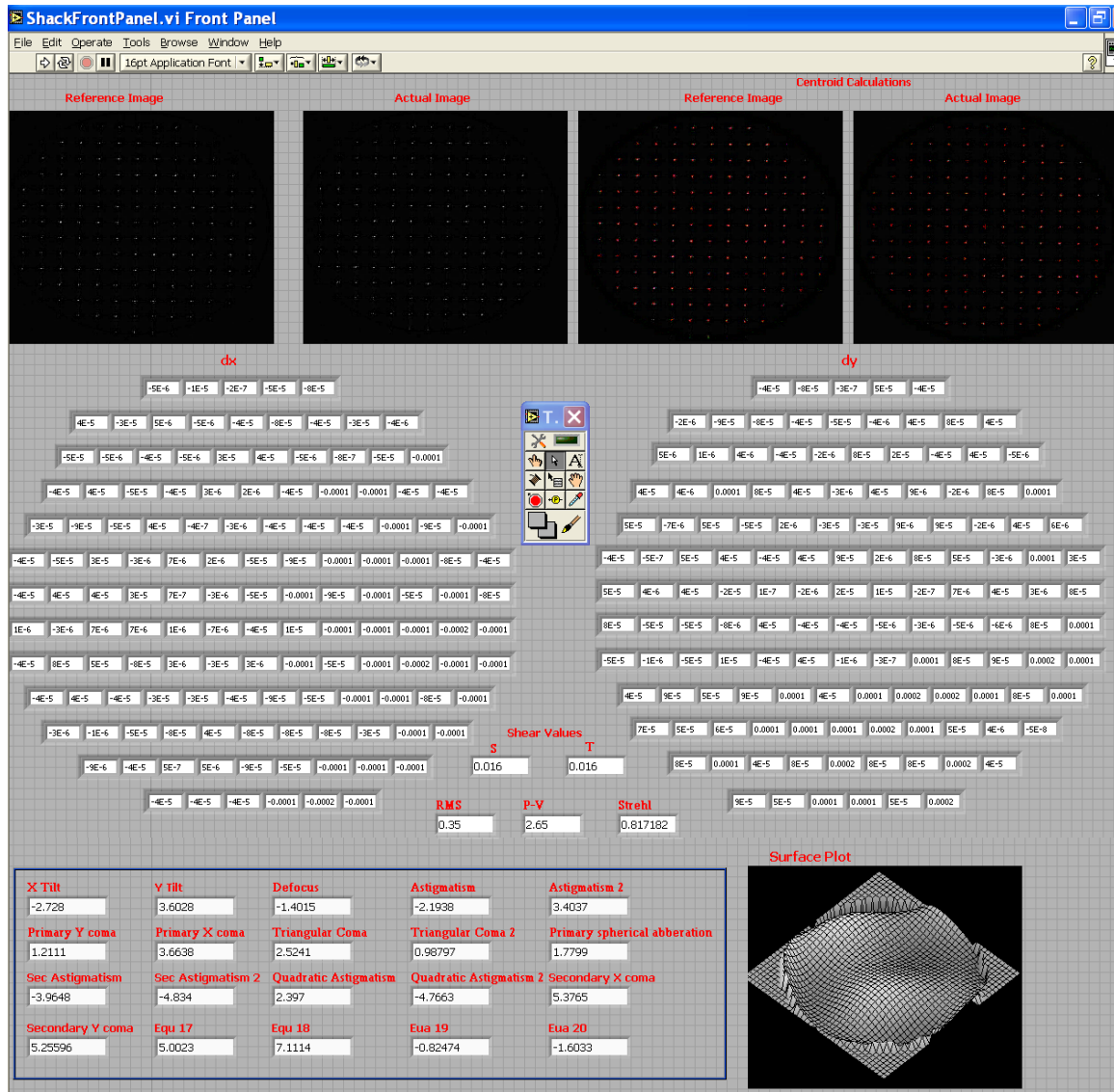


**Fig. 7.7 Front Panel of the Lab VIEW for the reduction of Shack Hartmann record.**

The wavefronts were mainly evaluated using the three measures namely, Strehl Ratio, Peak to Valley and the rms deviation. These measurements were calculated from the Zernike coefficients computed using the above methods. The tip-tilt and the defocus terms were removed from the estimate.

## 7.2 Laboratory Experiment using Polarization Shearing Interferometer Wavefront Sensor

The optical layout (Fig.7.8) for conducting the experiment with Polarization Shearing device, is very similar to the optical lay out for SH experiment. The optical system has been designed in such a way that with minimal change in the system optics two wavefront sensors can be conveniently employed in the same setup. Perhaps, this has another advantage when sensing has been done by two independent methods reliability also improves. The schematic of the optical lay out for the Polarization Shearing Interferometer experiment is shown below.

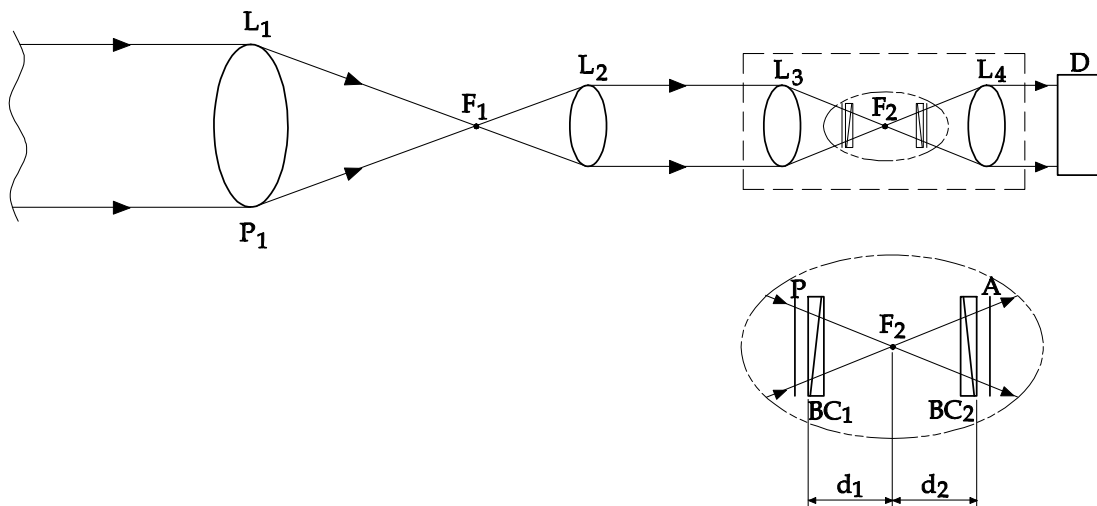


**Fig.7.8 Schematic diagram of the optical layout for Polarization Shearing Interferometer wavefront sensor. The positions of the BC are shown in the inset.**

The polarization Shearing Device is introduced in between the re-imaging optics. The device is located in such a way that the focus of the imaging optics lies on either side of the Babinet compensators. The polarization shearing device consists of a polarizer (P), analyzer (A) and two Babinet compensators (BC). The polarizers were procured from Edmund Optics and the Babinet compensators were procured from Halle, Germany. The optical specifications of the Babinet compensators are given in the table below.

<b>Aperture</b>	<b>15 x 15 mm</b>
<b>Wedge Angle</b>	<b>5 degrees</b>
<b>Material</b>	<b>Quartz</b>
<b>Surface accuracy</b>	$\lambda/20$
<b>Refractive Index</b>	
<b>a. Ordinary Ray</b>	<b>1.54424</b>
<b>b. Extra-ordinary Ray</b>	<b>1.55335</b>

### **7.2.1 Polarization Shearing Interferometer Experiment:**

The laboratory set up for the measurement using Polarization Shearing Interferometer is given in Figure 7.8. The beam reducer optics, the polarizer (P), two crossed Babinet compensators (BC) and the analyzer (A) are housed in a specially made aluminium tube. The close-up view of the BC is shown in the Figure 7.9.

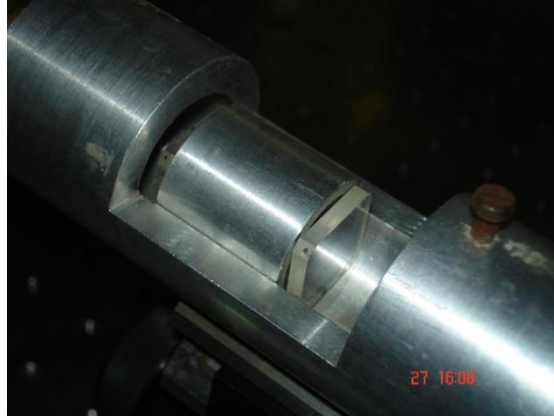


**Fig.7.9 A close up view of the mounting of the two crosses Babinet compensators in a cell**

The interferometric fringes projecting on the pupil plane is re-imaged on to the CCD detector using a lens  $L_3$ . The Dalsa Camera has been used as a detector. Number of interferometric records was obtained for the evaluation of the phase plate. One of the sample records is shown in Figure 7.10

Note that the inherent errors in the optical system. Later, the wavefront error plate or turbulator was introduced near the pupil plane (P1) of the Zygo interferometer beam. Proper attention and care was taken that the same face of the wavefront error plate was introduced into the optical path for SH experiment and PSI experiment, such that the results could be compared. These experiments were performed in quick succession such that other environmental parameters remain the same.

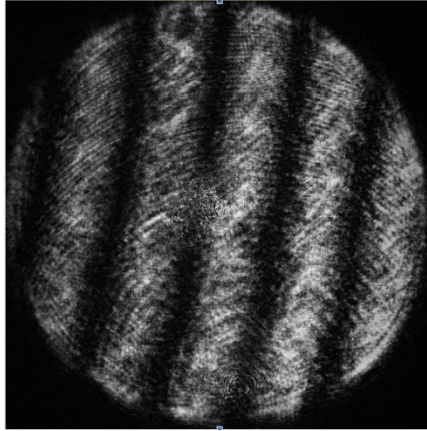


**Fig.7.10 The Interferometric record of the Polarization Shearing Interferometer obtained in the laboratory after introducing the phase error plate at the pupil plane of the optical system**

### **7.2.2 Data Analysis and Results:**

The data analysis of the PSI interferometric data has been carried out in the Lab View platform. The following methodology as shown in Figure 7.11 has been adopted based on the theory discussed in chapter 5.

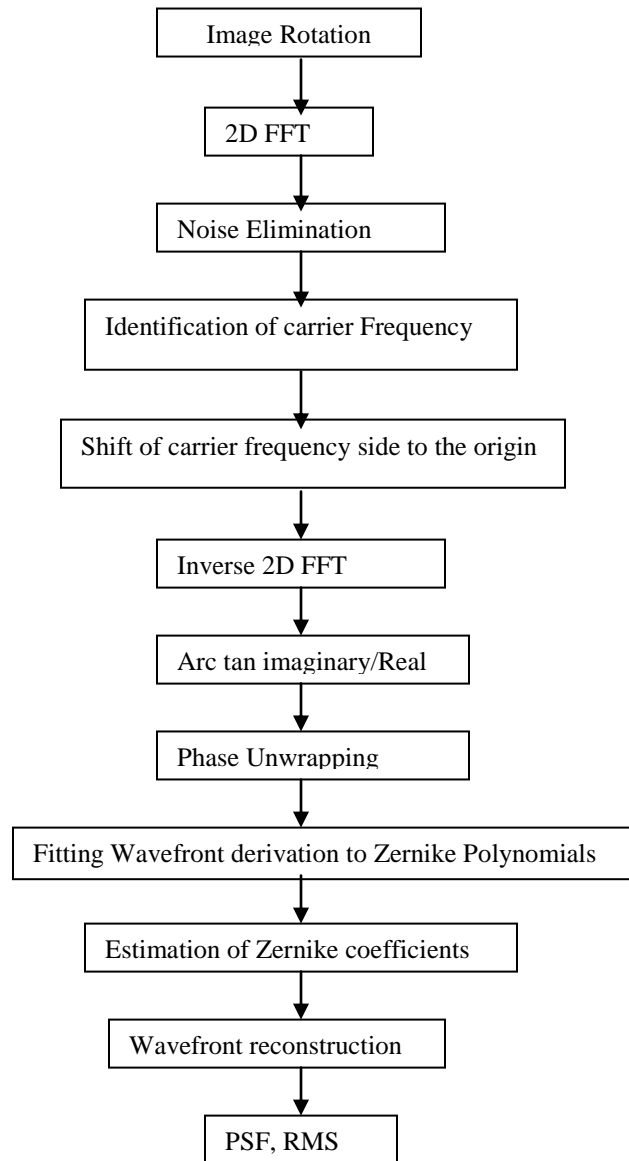


**Fig.7.11 Flow chart of the methodology adopted**

The Polarization Shearing interferogram is rotated by an angle equal to the ratio of the distances  $d_1$  and  $d_2$ . The inherent noise, in the interferograms were removed using the two dimensional Fourier transform

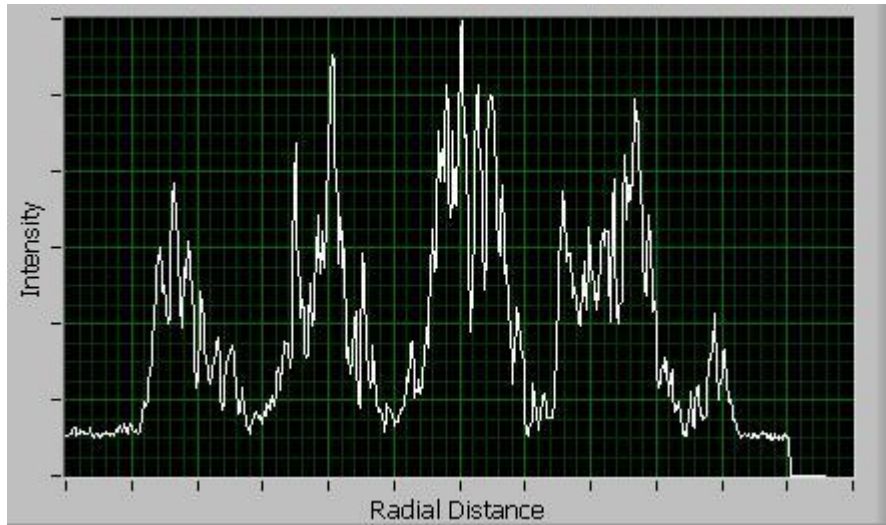


**Figure 7.12 A radial profile of the Polarization Shearing Interferogram showing the presence of high frequency noise**

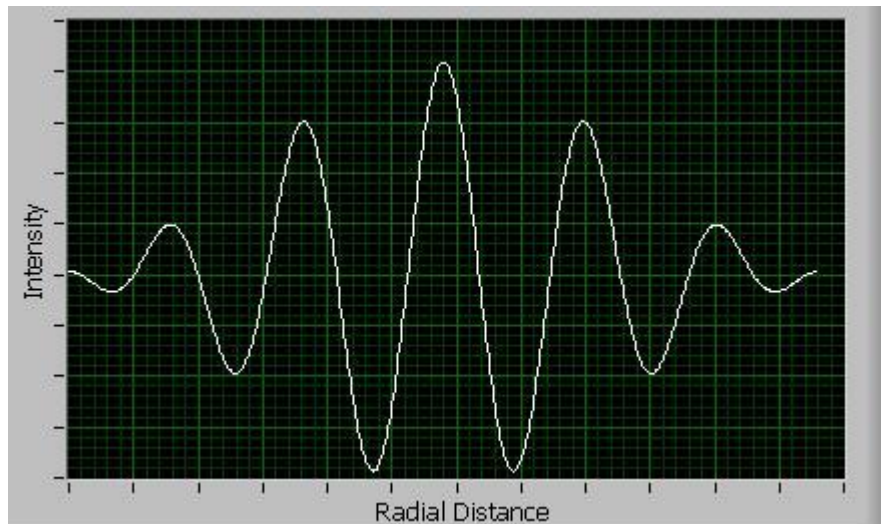


**Figure 7.13 The same radial profile of the interferogram after removing the high frequency noise using two dimensional Fourier transform technique.**

technique. A radial profile of the interferogram with noise and the noise removed by the Fourier transform method is shown in Figures 7.12 and

7.13 respectively. The carrier frequency i.e. the number of fringes in the field of view corresponds to the distance of the two Babinet Compensators on either side of the focus as seen from the intensity oscillations in Figure 7.13. This particular frequency is the predominant frequency in the Fourier Transform domain.

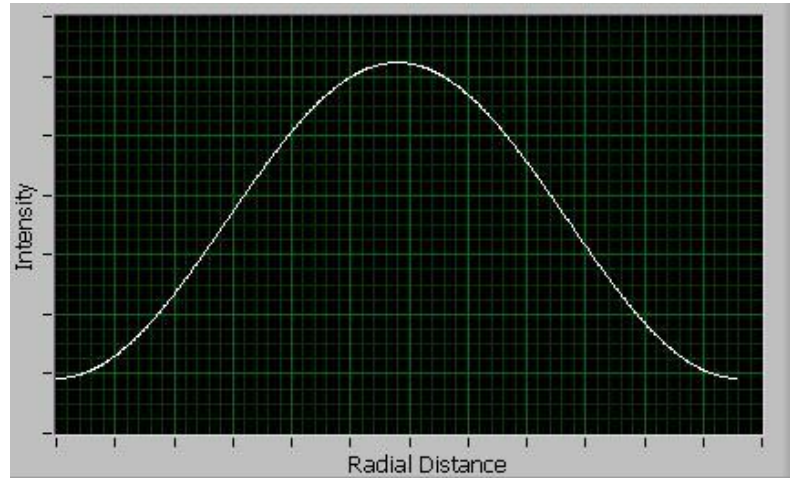


**Figure 7.14 The radial profile across the interferogram after removing the carrier frequency from the field of view.**

To recover the phase derivative, first suppress this Fourier mode corresponding to the carrier frequency and are thus left with the residual intensity profile with  $2\pi$  ambiguity is given in Figure 7.15. The next task is to remove  $2\pi$  ambiguity which is called phase unwrapping. On removal of the  $2\pi$  ambiguity by methods discussed in chapter 6.1.2. the phase derivative was computed and one dimensional ambiguity removed from Fig.7.15 is shown in Figure 7.16., The two dimensional map of the phase derivative thus obtained is as shown in Figure 7.17.

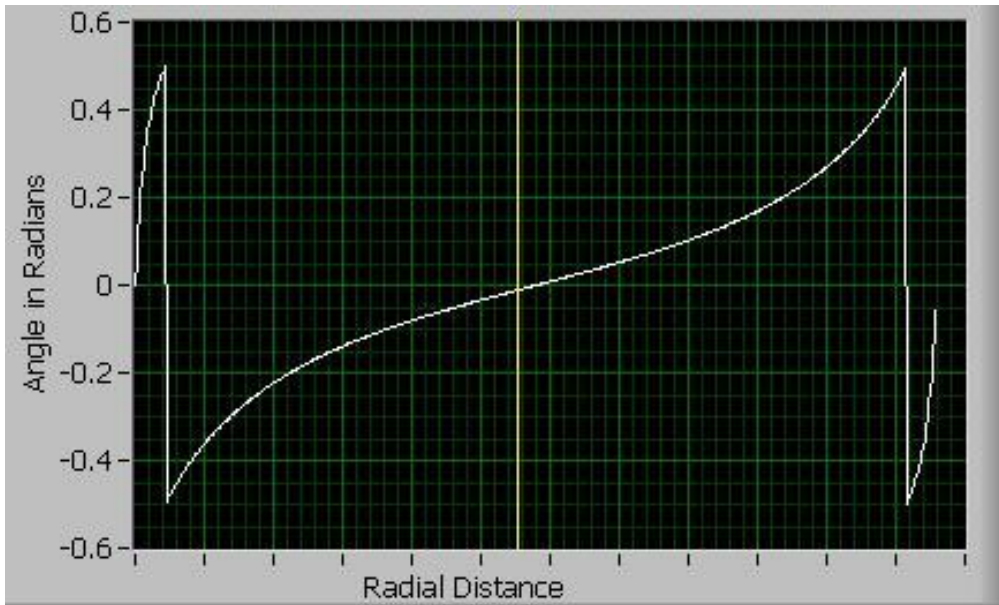


**Figure 7.15** A radial profile showing the  $2\pi$  ambiguity



**Figure 7.16** The radial profile after the  $2\pi$  ambiguity removed

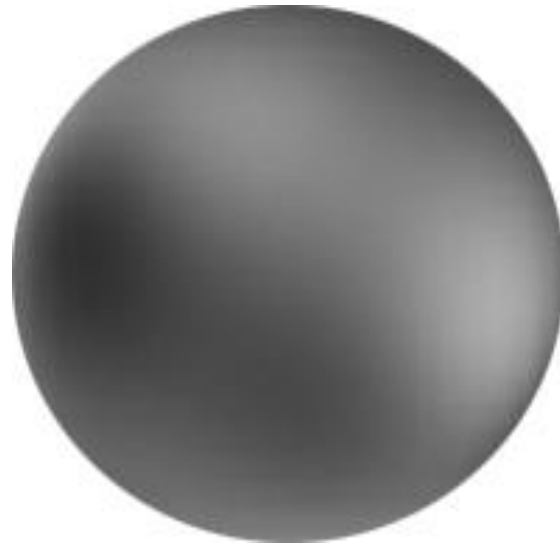


**Figure 7.17 The two dimensional phase derivative inclusive of the shear factor.**

The derivative of the Phase was fitted to the Zernike polynomial as discussed and using least squares matrix inversion method the Zernike coefficients were determined. By virtue of the derivative the piston term is removed.

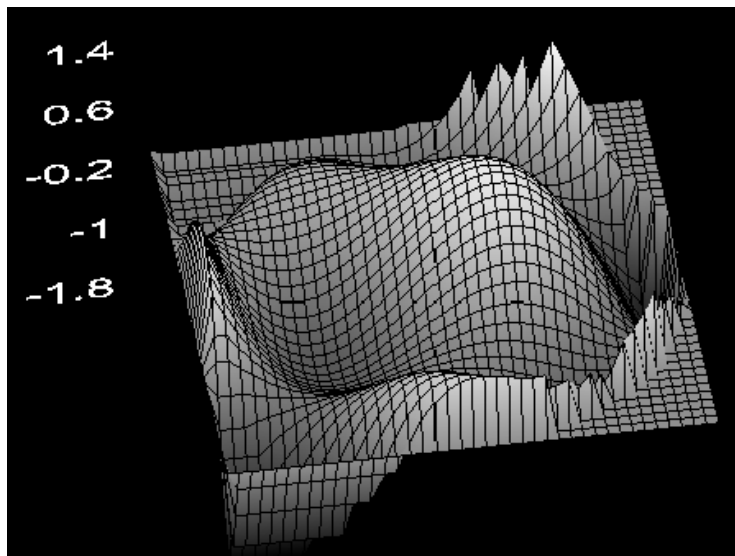


**Fig.7.18 The 2 D wavefront error map (in  $\lambda$ ) of the phase plate as computed from the Zernike polynomials.**

After removing the x-tilt and y-tilt and the defocus term the wavefront is recomputed using the Zernike polynomials. The 2 dimensional wavefront error computed is shown in Figure 7.18. The Zernike coefficients are compared (Fig.7.19) in the bar diagram.

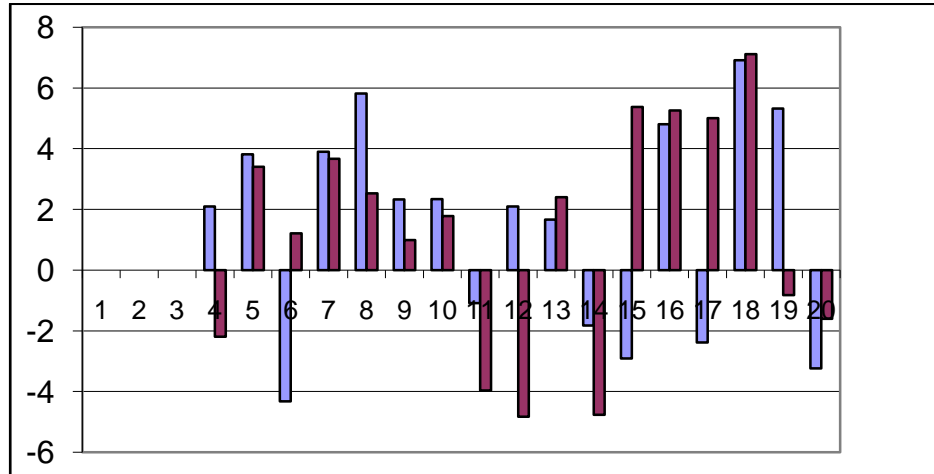


**Fig.7.19 A comparative plot of the 20 Zernike coefficients computed by the SH and PSI method**

The wavefront variance is defined as

$$\sigma_w^2 = \iint (W(\rho, \phi))^2 \rho d\rho d\phi - \left[ \iint W(\rho, \phi) \rho d\rho d\phi \right]^2$$

$$\sigma_w^2 = \sum_{n,m} a_{n,\pm m}^2 - a_{0,0}^2$$

where  $a_{n,m}$  are the Zernike coefficients derived from the above analysis. In practice, the variance is computed using integration method. According to the definition of Strehl ratio, which is related to the variance of the wavefront, these values are computed from the Zernike coefficients. The rms deviation of the wavefront is computed as

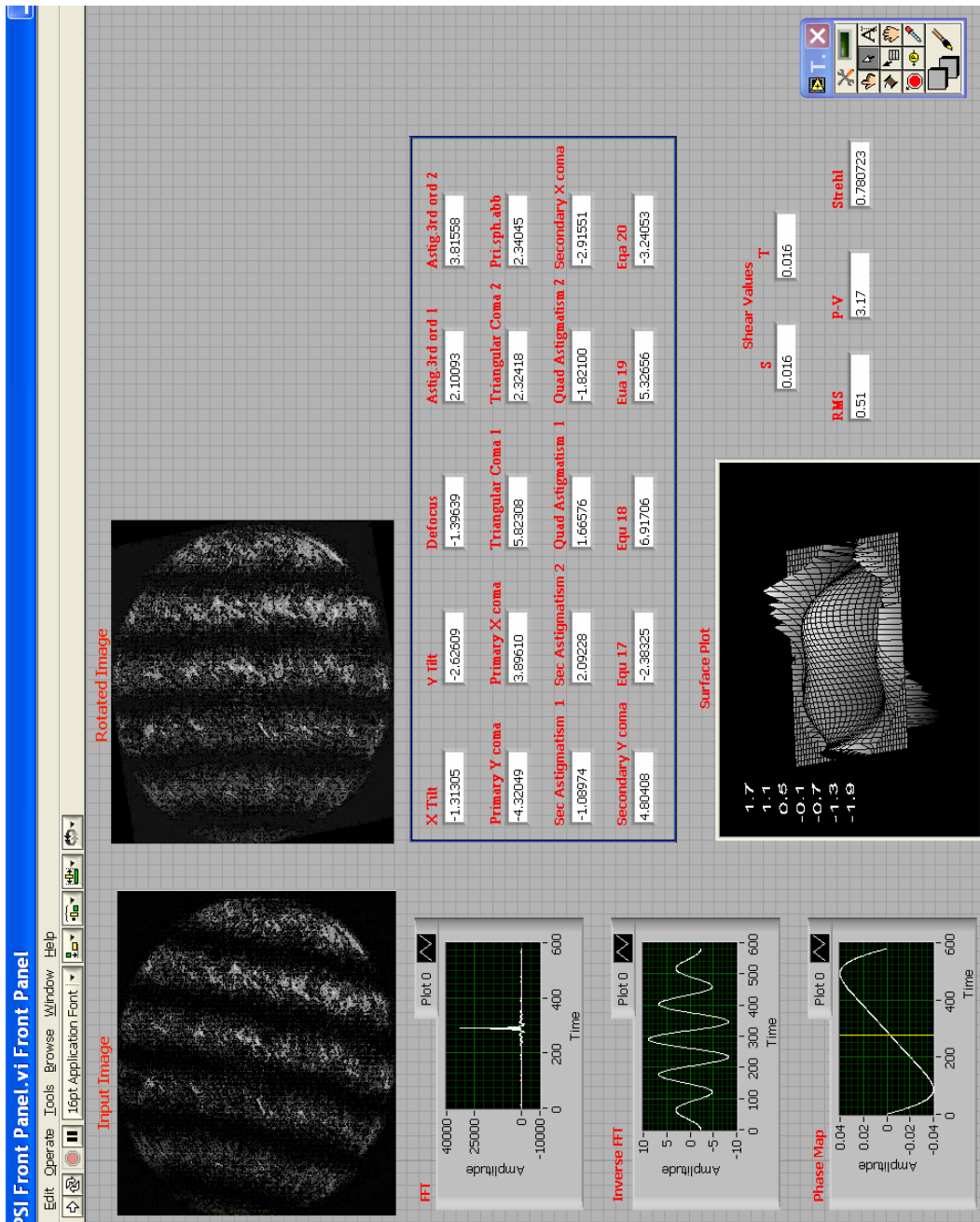


**Fig. 7.20 Front Panel of the Lab VIEW for the reduction of PSI record.**

$$\text{Sigma } rms = \sqrt{\sum_{i=3}^{21} a_i^2}$$

where  $a_i$  are the normalized Zernike coefficients.

The peak-to-valley – SH :  $2.65 \lambda$

The peak-to-valley – PSI :  $3.17 \lambda$

The rms – SH :  $0.35 \lambda$

The rms – PSI :  $0.51 \lambda$

The Peak to Valley of the wavefront error due to the phase plate as estimated from the Zygo interferometer gave  $2.9 \lambda$  and the rms error measured as  $0.42 \lambda$ . The Zernike coefficients could not be compared with the Zygo results as the numbering and normalization followed is different from the normalization used here.

### 7.3 Discussion

Several experiments were carried out and PSI interferograms and SH images were recorded in the laboratory in different optical setup. Later, in order to do the experiments in the same setup, the new optical design was worked out. The vibration and the thermal effects, affect the fringe quality considerably. The use of anti-vibration table and controlled thermal environment helped to overcome the above shortcomings. Analysis of all the interferograms and the SH images were carried out in Lab View and the exercise helped to overcome the bugs in the software. A typical record obtained in the laboratory has been given in the thesis presentation.

The wavefront error surface plotted in the Figures 7.7 and 7.19 are obtained using the Shack Hartmann method and Polarization shearing interferometer method respectively. The error surface matches quite well in both the methods but the value of the Zernike coefficients

differ for certain aberrations. The Shack Hartmann method employed only  $13 \times 13$  matrix elements where as the Polarization Shearing interferometer method employed a total of 1251 data points for the computation. The PSI method had a better sampling of the pupil compared to the SH method. Another reason, for the difference one can notice in the surface profile, is that the surface is slightly rotated with respect to one another. As mentioned before, the PSI record was rotated by an angle to suit the Fourier transform reduction technique. The order of magnitude of the surface error in both cases agrees as well. The rms and the Strehl ratio values also agree very well in both the SH and PSI methods.

The laboratory experiments and the results demonstrate that the Polarization shearing interferometer using Babinet compensator can be conveniently employed in adaptive optics system to estimate the wavefront errors introduced by the atmospheric turbulence.

# Chapter 8

## Conclusions

Estimation of the wavefront errors is very important aspect in adaptive optics. Besides the telescope system errors, most of the errors are introduced by the atmospheric turbulence. The atmospheric turbulence is aptly characterized by the Kolmogorov model. It is essential to accurately estimate these aberrations in the dynamic situations, in order to apply, real time corrections. A simulation study by Jeffrey et al. (2002) of the shearing interferometers and Shack Hartmann sensor prove that the Shearing interferometer performs better in the presence of low Fried parameter and for Rytov numbers greater than 0.2. A new method of wavefront sensing using a polarization shearing interferometer has been developed for this purpose. An attempt has been made to use the Babinet Compensator as a convenient and suitable optical device to create the shearing of wavefronts in two orthogonal directions simultaneously. Since the sensitivity of the BC for the measurement of phase is shown to be  $2\pi$  milli radian, it was planned to exploit its maximum potential. An in-depth, study has been made of the proposed polarization shearing interferometer. Fourier theoretical approach has been applied to the Polarization Shearing Interferometer to establish the

basis of the wavefront sensing. Theoretical simulations were carried out for visualization of various aberrations in the interferometric fringe pattern. The study reveals that under moderate turbulent conditions where  $D/r_0 = 0.025$ , the sensitivity of the PSI is not altered significantly. The errors due to other factors like noise and ripples are well removed in the reduction procedure. The proposed method uses a single interferogram, in order to reconstruct the complete wavefront. Two dimensional shears in orthogonal directions are produced in a single set up, by the proper choice of the Babinet Compensator and system parameters. Use of Fourier transforms techniques to estimate the wavefront errors have been demonstrated. In an adaptive optics situation, one requires a fast method of wavefront sensing and reconstruction. The proposed method using Babinet compensator based Polarization Shearing Interferometers can be suitably used with greater amount of flexibility. Being in the intensity mode, high spatial sampling is possible and speed and sensitivity is dictated by the detector dynamic range and the computation time, which is progressively improving. A study of Shack Hartmann wavefront sensing was also used to estimate the phase plate errors for comparison with the polarization shearing interferometer results. The results are presented in the seventh chapter. To conclude, wavefront sensing by Polarization Shearing interferometer using two crossed Babinet compensator is quite a promising option. Thus, in essence, is the main advantage of the system, designed and developed as is reported in the foregoing chapters.

There is also much work to be carried out in the future in order to fully exploit the maximum potential of the PSI. As part of the future work, more realistic model of Kolomogorov turbulence will be simulated in the laboratory and can be applied to evaluate the effect of Fried's parameter from PSI records. This is a very important requirement for the characterization of site seeing for its suitability for adaptive optics based astronomical telescopes.

This wavefront sensing method is planned to be used in adaptive optics systems of the future large telescopes.

## **Bibliography**

[1] Atad E; John W. Harris; Colin M. Humphries; Victoria C. Salter, "Lateral Shearing interferometry: evaluation and control of the performance of astronomical telescopes" SPIE 1236, "Advanced Technology Optical Telescopes IV", Lawrence D. Barr, Editors, 575-584 (1990)

[2] Babcock, H.W, "The possibility of compensating astronomical seeing," Publ. Astron. Soc. Pac. 65, 229 – 236 (1953).

[3] Ben C Platt and Roland Shack, "History and Principles of Shack-Hartmann Wavefront Sensing" Journ. of Refr. Surg. Vol. 17, S573 – S576 (2001).

[4] Bone D.J, Bachor H.A, and Sandeman R.J, "Fringe pattern analysis using a 2-D Fourier Transform," Appl.Opt. Vol.25, No.10, 1653 – 1660 (1986).

[5] Born E and Wolf, "Principles of Optics" Pergamon Press. (1970).

[6] Creath, K., "Phase-Measurement Interferometry Techniques" in Progress in Optics, Vol. XXVI, ed. E. Wolf, Ed., Elsevier Science Publishers, 349 – 393 (1988).

[7] Dai Guang-ming and V.N.Mahajan, "Zernike annular polynomials and atmospheric turbulence", J.Opt.Soc.Am. A Vol.24, No.1, 139 – 155, (2007)

- [8] Esposito.S, and A.Riccardi, "Pyramid wavefront sensor behavior in partial correction Adaptive Optic systems, *Astron.&Astrophy.* 369, L9-L12 (2001)
- [9] Francon, M and S.Mallick, "Polarization Interferometers" Wiley, NY, (1971).
- [10] Fried, D.L. "Statistics of a geometrical representation of wavefront distortion" *J.Opt.Soc.Am.*, Vol.55, No.11, 1427 – 1435 (1965).
- [11] Fried, D.L. "Optical resolution through a randomly inhomogeneous medium for very long and very short exposures", *J.Opt.Soc.Am.*, Vol.56, No.10, 1372 – 1379 (1966).
- [12] Greivenkamp, J.E., and Bruning, J.H., " Phase shifting interferometers" in *Optical Shop Testing*, Ed., Malacara, D., Wiley Series, 501 – 598 (1992).
- [13] Greenwood, D.P. "Bandwidth specification for adaptive optics systems", *J.Opt.Soc.Am.* Vol.66, No.3, 390 – 393 (1977)
- [14] Harbers G, P.J.Kunst and G.W.R Leibbrandt, "Analysis of lateral shearing interferograms by use of Zernike polynomials", *Appl.Opt.* 35, No.31, 6162 – 6172 (1996)
- [15] Hardy, J.W. and Alan J. MacGovern., "Shearing interferometry: a flexible technique for wavefront measurement" SPIE, Vol. 816, "Interferometric Metrology", 180 – 195 (1987).
- [16] Hardy J.W, "Adaptive Optics for Astronomical Telescopes" Oxford University Press, (1998).

[17] Hariharan P and Sen D “Accurate measurements of phase differences with the Babinet compensator” 1960 *J. Sci. Instrum.* Vol.37, 278 – 281 (1960).

[18] Hippler Stefan, Felix Hormuth, David J Butler, Wolfgang Brandner and Thomas Henning, “Atmosphere-like turbulence generation with surface-etched phase-screens” *Optics Exp.* Vol. 14, 22, 10139 – 10148 (2006).

[19] Humphries, C.M., Harris, J.W. and Atad, E., “Determination of the wavefront errors of an astronomical telescope using lateral shearing interferometry” *Mon. Not. R. Astron. Soc.*, 284, 655 – 668 (1997).

[20] Hyun-Ho Lee, Jang-Hoon You and Seung-Han Park, “Phase shifting lateral shearing interferometer with two pairs of wedge plates” *Optics Lett.* 28 (22), 2243 – 2245 (2003).

[21] Ichikawa, K, Lohmann, A.W. and Takeda, M., “Phase retrieval based on the irradiance Transport Equation and the Fourier Transform method: Experiments”, *Appl.Opt.* Vol. 27, No.16, 3433 – 3436 (1988)

[22] Jeffrey D Barchers, David L Fried, and Donald J Link, “Evaluation of the performance of a shearing interferometer in strong scintillation in the absence of additive measurement noise”, *Appl. Opt.* Vol. 41, No.18, 3674 – 3684 (2002)

[23] Jerrard H.G, “Formation of fringes in a Babinet Compensator” *J.Opt.Soc.Am.* Vol. 39, No.12, 1031 – 1035 (1949)

[24] Joseph M Geary, "Introduction to wavefront sensors" Tutorial texts in Optical Engineering, SPIE Press, Vol.TT 18 (1995).

[25] Kingslake R, "Lens Design Fundamentals", Acad. Press (1978).

[26] Kolmogorov, A.N., "The local structure of turbulence in incompressible viscous fluids for very large Reynolds' numbers", in "Turbulence, Classical papers on Statistical Theory" Ed.S.K.Friedlander and L.Topper, 151 – 155, Wiley-Interscience (1961).

[27] Labeyrie A, "Attainment of diffraction limited resolution on large telescopes by Fourier analyzing speckle patterns", Astron. Astrophys. 6, 85 (1970).

[28] Macy,W.W. Jr., "Two-Dimensional fringe pattern analysis," Appl.Opt. Vol. 22, No.23, 3898 – 3901 (1983).

[29] Mahajan V.N. "Strehl ratio for primary aberrations: some analytical results for circular and annular pupils" J.Opt.Soc.Am., Vol.72, No.9, 1258 – 1266 (1982)

[30] Mahajan V.N., "Strehl ratio for primary aberrations in terms of their aberration variance" J.Opt.Soc.Am., Vol. 73, No.6, 860 – 861 (1983)

[31] Malacara, D. Optical Shop Testing, 2<sup>nd</sup> Edn. John Wiley & Sons, (1992).

[32] Malacara-Hernandez D, Gonzalo Paez, D.Malacara-Doblado and J Garcia-Marquez, "Wavefront retrieval from lateral shearing interferograms with Fourier techniques" SPIE, 3744 " Interferometry '99: Techniques and Technologies" 290 – 295 (1999).

[33] Milonni Peter W “ Resource Letter: AOA – 1: Adaptive Optics for Astronomy”, Am.J.Phys, Vol. 67, No.6, 476 – 485 (1999).

[34] Noll, R.J., “ Zernike polynomials and atmospheric turbulence” J. Opt. Soc. Am., Vol. 66, No.3, 207 – 211 (1976).

[35] Nugent K.A, “Interferogram analysis using an accurate fully automatic algorithm”, Appl.Opt. Vol.24, No.18, 3101 – 3105 (1985).

[36] Okuda Seiichi, Takashi Nomura, Kazuhide Kamiya, Hiroshi Miyashiro, Kazuo Yoshikawa and Hatsuzo Tashiro, “High-precision analysis of a lateral shearing interferogram by use of the integration method and polynomials”, Appl.Opt. Vol. 39, No.28, 5179 – 5186 (2000)

[37] Pandya T.P and A.K.Saxena, “ An analysis of Babinet Compensator fringes using Jones Calculus”, Kodai. Obs. Bull.Ser. A Vol. 2, 107 – 114 ( 1978)

[38] Peiyong Liang, Jianping Ding, Zhou Jin, Cheng-Shan Guo and Hui-tian Wang, “Two dimensional wavefront reconstruction from lateral shearing interferograms”, Optics Exp. Vol.14, No.2, 625 – 634 (2006)

[39] Pinna E, A.Puglisi, S.Esposito, A Tozzi and Goncharov, “Simple implementation of phase screens for repeatable seeing generation” in SPIE, Vol. 5490, “Advancements in Adaptive Optics” 830 – 836 (2004).

[40] Primot.J, G.Rousset and J.C.Fontanella, “Deconvolution from wavefront sensing: a new technique for compensating turbulence-degraded images” J.Opt.Soc.Am., A., Vol.7, No.9, 1598 – 1608 (1990)

[41] Pugh, W.N, Lobb, D.R., Walker, D.D., Williams, T.L., “Pupil-imaging wavefront gradient sensor”, in “Adaptive optical systems and Applications” SPIE, Vol. 2534, 312 – 317 (1995).

[42] Ragazzoni, R. “Pupil plane wavefront sensing with an oscillating prism”, J. Mod. Opt., Vol. 43, 289 – 293, (1996).

[43] Rhoadarmer Troy A. and Roger P Angel, “A method to generate atmosphere like turbulence.” Appl.Opt. Vol. 40, No.18, 2946 – 2955 (2001).

[44] Riccardi,A., Bindi, N., Ragazzoni, R., Esposito, S. and Stefanini, P. “Laboratory characterization of a ‘Focault-like’ wavefront sensor for adaptive optics”, in “Adaptive optical system Technologies”, SPIE, Vol.3353, 941 – 951, (1998).

[45] Roggemann C Michael, Byron M Welsh and Robert Q Fugate, “Improving the resolution of ground-based telescopes” Rev. Mod. Phys. Vol 69, No.2, 437 – 506 (1997).

[46] Rongwei Xu, Zhu Luan, Hongzhan Liu and Liren Liu, “Measurement of the diffraction limit wavefront with double shearing interferometers”, J.Opt.A: Pure. Appl.Opt. Vol.8, 164 – 171 (2006)

[47] Roddier C and F. Roddier, “Interferogram analysis using Fourier Transform techniques,” Appl. Opt. Vol. 26, No.9, 1668 – 1673 (1987).

[48] Roddier F. “Curvature sensing and compensation: a new concept in adaptive optics”, Appl.Opt., Vol. 27, No.7, 1223 – 1225, (1988).

- [49] Roddier, F. "Imaging through the atmosphere" in "Adaptive Optics in Astronomy" Cambridge University Press. 9 – 22 ( 1999).
- [50] Rousset, G. "Wave-front sensors" in Adaptive Optics in Astronomy, 91 – 130, Cambridge University Press, (1999).
- [51] Sandler, D G., Cuellar, M Lefebvre. T Barrett, R. Arnold, P. Johnson, A. Rego, G. Smith, G.Taylor and B.Spivey., " Shearing interferometry for laser-guide star atmospheric correction at large  $D/r_0$ " J. Opt. Soc. Am. A., Vol.11, No.2, 858 – 873 (1994).
- [52] Saxena A.K, "Quantitative Test for concave aspheric surfaces using a Babinet Compensator," Appl. Opt. Vol. 18, No.16, 2897 – 2901, (1979).
- [53] Saxena A.K and Jayarajan A.P, "Testing concave aspheric surfaces: Use of two crossed Babinet Compensators", Appl. Opt. Vol. 20, No.5, 724 (1980).
- [54] Saxena A.K, and Lancelot J.P, "Theoretical fringe profiles with crossed Babinet compensators in testing concave aspheric surfaces," Appl. Opt. Vol. 21, No.22, 4030 – 4032 (1982).
- [55] Saxena A.K, and Lancelot J.P, "Wavefront sensing and evaluation using two crossed Babinet compensators," SPIE, 1121, "Interferometry '89" 41 – 43 (1990).
- [56] Seward A.J, "Image plane filters and adaptive optical systems", Ph.D., thesis, New Mexico State University, (2005).
- [57] Swapan K Saha, "Diffraction-limited Imaging with Large and Moderate Telescopes" World Scientific Pub. Co. (2007)

[58] Takeda M, Ina H and Kobayashi S, “Fourier Transform method of fringe-pattern analysis for computer based tomography and interferometry.” J.Opt.Soc. Am, Vol. 72, 156 – 160 (1982).

[59] Tubbs Robert, “Seeing timescales for large aperture optical/infrared interferometers from simulations”, SPIE, 5491, “New Frontiers in Stellar interferometry”, 1240 – 1248 (2004).

[60] Tubbs Robert, “Effect of wavefront corrugations on fringe motion in an astronomical interferometer with spatial filters”, Appl.Opt. Vol.44, No.29, 6253 – 6257 (2005).

[61] Tyson R.K, “Principles of Adaptive Optics” Acad.Press. (1991)

[62] Welsh M Byron, Brent L.Ellerbroek, Michael C.Roggemann, and Timothy L Pennington, “Fundamental performance comparison of a Hartmann and a Shearing interferometer wavefront sensor”, Appl. Opt. Vol.34, No.21 4186 – 4195, (1995).

[63] Wyant, J.C “ Use of an ac heterodyne lateral shear interferometer with real-time wavefront correction systems” Appl.Opt. Vol. 14, No.11, 2622 – 2626 (1975).